Combinatorial Studies of Fe-Zn and Fe-Si-Zn Alloy Negative Electrodes for Li-ion Batteries

by

Lauren MacEachern

Submitted in partial fulfilment of the requirements
for the degree of Master of Science

at

Dalhousie University
Halifax, Nova Scotia
August 2014

Table of Contents

List of Tables

List of Figures

Abstract

In this work Fe-Zn and Fe-Si-Zn alloy systems were studied for use as negative electrodes in Li-ion batteries. The aim was to understand the electrochemistry of these alloy systems and observe if the addition of Fe and Zn to Si thin-film electrodes leads to improvements in performance by reducing volume expansion and suppressing formation of $Li_{15}Si_4$. Thin-film libraries were fabricated using combinatorial sputtering. X-Ray diffraction, Mössbauer effect spectroscopy, and electron microprobe were used to characterize structure of the thin-films. Electrochemical cycling measurements were used to determine if alloys based on these systems are practical for use in Li-ion batteries.

Electrochemical performance of Fe-Zn electrodes was strongly dependent on composition. The cycle life and coulombic efficiency improved as Fe concentration in electrodes increased to x = 0.12. A simple macroscopic atom model predicted that compositions with up to 50 atomic percent Fe would be active toward Li. However, the capacity decreased as the iron content increased and the Fe_xZn_{1-x} alloys became completely inactive when the Fe content was above 12 atom %. Ex-situ X-ray diffraction and Mössbauer measurements were used to explain the structural changes that occur during cycling.

A large amorphous region exists in Si-rich compositions of the Fe-Si-Zn system. The electrochemistry of numerous compositions of Fe-Si-Zn materials was determined near room temperature. Voltage curves and capacity of the films was strongly dependent on composition. ICE and hysteresis improved with increasing Si concentration in the electrodes. Both Zn and Fe additions to Si were found to suppress the formation of $Li_{15}Si_4$ during cycling.

List of Abbreviations and Symbols Used

A   area percentage

Å   angstrom

A^+ positive ion of element A

at %   atomic percent

c speed of light

CE   coulombic efficiency

CS   center shift

d lattice spacing

d.u.   density unit

DFT   Density Functional Theory

dQ/dV   differential capacity

e magnitude of charge of an electron

E energy

eV   electron volt

g nuclear g-factor

H   magnetic field of hyperfine field distribution site

HFD   hyperfine field distribution

I   current

I spin quantum number

ICE   initial coulombic efficiency

IRC   irreversible capacity

K crystallite shape factor

k_B	Boltzmann constant
Li-ion	lithium ion
M	mass
n_{WS}	electron density of the Wigner-Seitz cell for a given element
Q	charge transferred
Q	nuclear quadrupole moment
QS	quadrupole splitting
QSD	quadrupole splitting distribution
r.f.	radio frequency
SEI	solid electrolyte interphase
t	size of crystallite
T	temperature
V	potential
V, v	velocity
V_A	molar volume of element A
w	full width at half maximum
W	watt
WDS	Wavelength Dispersive Spectroscopy
XRD	X-Ray diffraction
x_s	surface area concentration
δ	isomer shift (center shift)
$|\Psi(0)|^2$	s-electron density at nuclei
°	degrees

μ   chemical potential

ΔH   enthalpy of formation

Ө   angle

λ   wavelength

φ   work function

ω   angular frequency

Acknowledgements

Chapter 1 Introduction

Lithium ion batteries have received increasing attention in recent years due to rapid growth in the portable electronics and electric vehicle markets. There is a demand for smaller batteries that last longer between charges for use in devices such as cellular phones and tablets. There is also demand for batteries that will perform well over thousands of cycles and last upwards of ten years for use in the growing electric vehicle market. With the emerging use of electric vehicles which use thousands of Li-ion batteries in just one vehicle, it is crucial to keep the cost of materials used in Li-ion batteries minimal.

Li-ion battery technology has been optimized over the past 23 years with the majority of cells using graphite and $LiCoO_2$ active materials in the negative and positive electrodes, respectively. In order to meet increasing energy demands, the development of new electrode materials for Li-ion batteries should be pursued. These new materials should ideally be abundant, easily manufactured, cost effective, sustainable, and safe to work with.

1.1 Lithium Ion Batteries

A Li-ion battery is a device which converts chemical energy into useable electrical energy. A Li-ion battery consists of many components, including, but not limited to the positive electrode (cathode), the negative electrode (anode), electrolyte, porous separators, current collectors, cell can, header, vent and tabs. Li must be able to insert into the electrodes via efficient and reversible redox reactions. The electrolyte consists of a Li salt (such as $LiPF_6$ or $LiClO_4$) in a solvent typically comprising combinations of cyclic and/or linear carbonates (such as ethylene carbonate, diethylene carbonate, ethyl

methyl carbonate). Porous separators are sandwiched between the positive and negative

electrode and allow for passage of Li^+ ions between electrodes while being electrically

insulating to prevent short circuiting of the cell. Electrodes are in electrical contact with

current collectors which can be electrically connected to an external circuit. A schematic

of a Li-ion cell is shown in Figure 1.1.
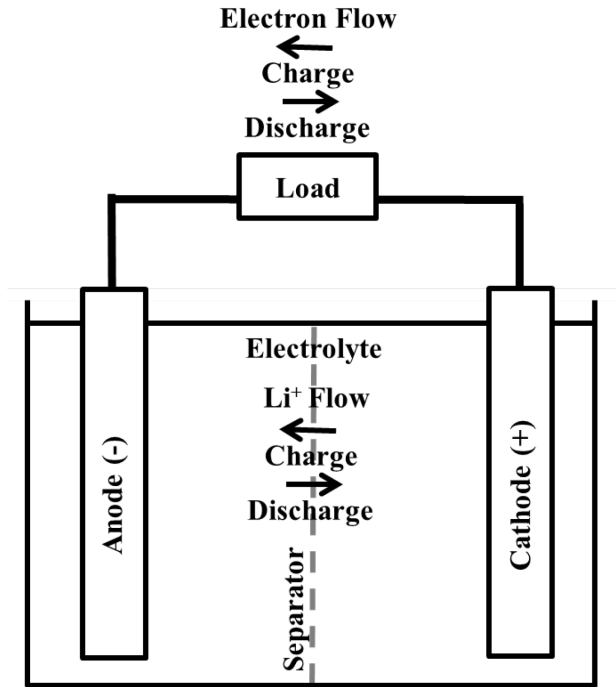
Figure 1.1 Schematic of a Li-ion cell

During the discharge of a Li-ion cell the negative electrode acts as the anode and is

oxidized while the positive electrode acts as the cathode and is reduced. Electrons travel

through an external circuit from the anode to cathode while positive (Li^+) ions pass from

the positive to negative electrode via the electrolyte to complete the circuit. The

discharge process is driven by a difference in chemical potential between the positive and

negative electrodes. The resulting cell voltage, V, can be expressed as:

$$V = - \frac{\mu_{cathode} - \mu_{anode}}{e},$$
(1.1)

where $\mu_{cathode}$ and μ_{anode} are the chemical potentials of Li ions in the cathode and anode, respectively, in units of electron volts and e is the magnitude of charge of an electron.

During the charge of a Li-ion cell the negative electrode acts the cathode and is reduced while the positive electrode acts as the anode and is oxidized. An external electric potential difference is applied across the cell, causing electrons to travel in the opposite direction (from negative to positive electrode) while Li^+ ions migrate to the positive electrode to complete the circuit. One discharge/charge process is referred to as a cycle.

1.2 Negative Electrodes for Li-ion Batteries

Current commercial Li-ion cells commonly use graphite as the negative electrode. Graphite negative electrodes are low in cost, abundant, and easily handled, making them appealing for use in Li-ion batteries. Graphite electrodes exhibit excellent cycling performance and long cycle life. Graphite has theoretical gravimetric and volumetric capacities of 372 mAh/g and 833 Ah/L, respectively. Graphite can electrochemically be intercalated with Li according to the following reversible reaction:

$$Li^+ + C_6 + e^- \leftrightarrow LiC_6. \tag{1.2}$$

A small volume change (~10%) occurs during the insertion of Li into graphite because Li^+ ions occupy space between the graphite layers, causing them to expand.[1,2] Graphitic negative electrodes for Li-ion batteries have been studied extensively and have been optimized for use in commercial cells.[3–5] Although graphite electrodes have been optimized for use in commercial cells, they exhibit low volumetric capacity compared to many other elements that can reversibly react with Li^+.

3

Many other materials can reversibly react via an alloying reaction with lithium at low potential vs. Li/Li^+, making them possible negative electrode materials. The alloying reaction is:

$$xLi^+ + M + xe^- \leftrightarrow Li_xM. \tag{1.3}$$

Table 1.1 lists some elements that alloy with Li and their theoretical volumetric capacities. From the table it is clear that much higher volumetric capacities than that of graphite can be attained when Li alloys with metals. It is also important to note that the volume expansions associated with alloying reactions are an order of magnitude greater than the volume expansion associated with the intercalation of Li into graphite. Unlike graphite where Li slides in and out of layers with minimal volume expansion, Li requires a volume of ~9 mL/mol in metallic alloys.[6] As a result, volumetric capacities must be calculated using the fully lithiated molar volume because the volume expansion associated with lithium alloying reactions is quite large. Figure 1.2 shows the gravimetric and volumetric capacities of some lithium alloys. The blue and orange lines are the gravimetric and volumetric capacity of graphitic carbon, respectively. It is clear from Figure 1.2 and Table 1.1 that many elements exhibit significantly higher capacity towards Li^+ than graphite. To find a viable replacement for graphite, new materials must be abundant, inexpensive, and easy to manufacture, which rules out some materials such as Ge, Ag, and Sb.

Table 1.1 Elements that react reversibly with Li and their associated fully lithiated phase. Capacities are calculated using the fully lithiated volume and volume expansion is calculated assuming Li requires 9 mL/mol Li.

Element	Fully Lithiated Phase	Capacity (Ah/L)	Volume Expansion (%)
C	LiC_6 [7]	833	10
Bi	Li_3Bi [8]	1662	126
Zn	$LiZn$ [9]	1475	98
Sb	Li_3Sb [10]	1771	147
Ag	Li_9Ag_4 [11]	1975	197
Al	$LiAl$ [12]	1411	90
Sn	$Li_{22}Sn_5$ [13]	2111	244
Ge	$Li_{22}Ge_5$ [14]	2214	290
Si	$Li_{15}Si_4$ [15]	2194	280
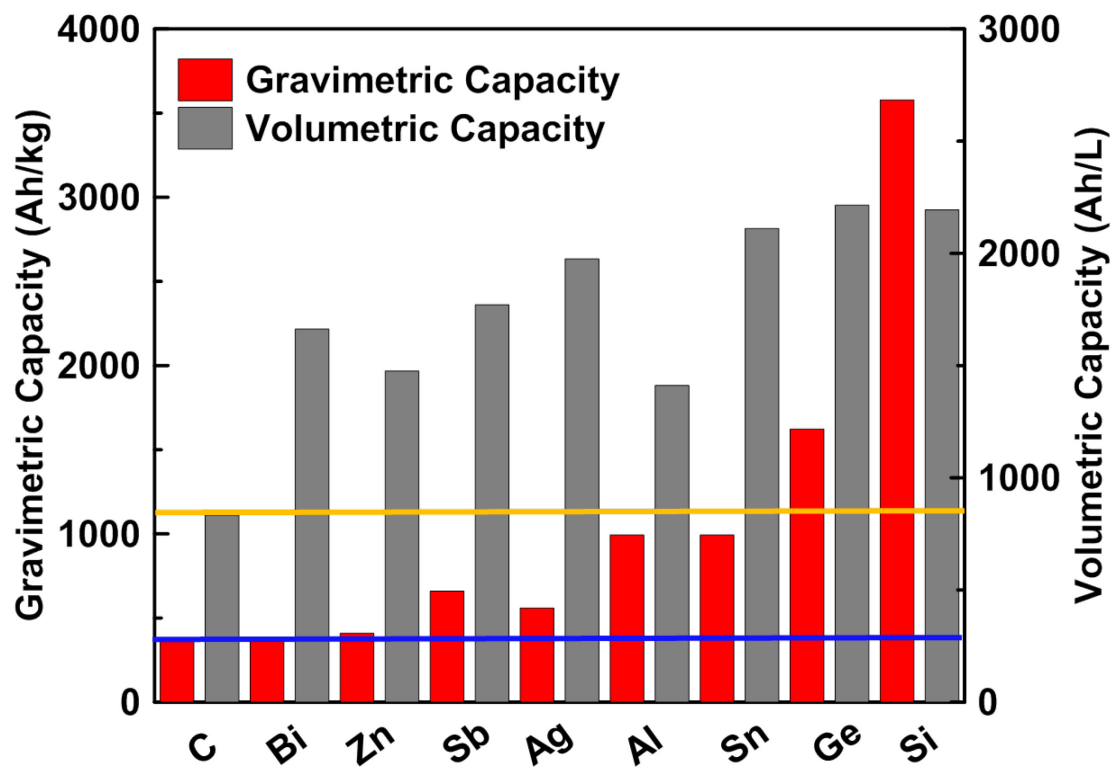
Figure 1.2 Gravimetric and volumetric capacities of selected elements toward lithium. The volumetric capacities are from Table 1.1. The blue and orange lines represent the gravimetric and volumetric capacities of graphitic carbon toward lithium, respectively.

The potential vs Li/Li$^+$ at which these high capacity elements react with Li is also important in determining if materials will be useful in Li-ion cells. The energy per unit volume of a lithium ion cell is dependent not only on capacity, but also on the potential at which the capacity is accessible.[6] Cell potential is the difference between the potential at the negative and positive electrodes. High energy density cells require a low average potential for the negative electrode. Figure 1.3 shows average potential vs volumetric capacity for the elements in Table 1.1.
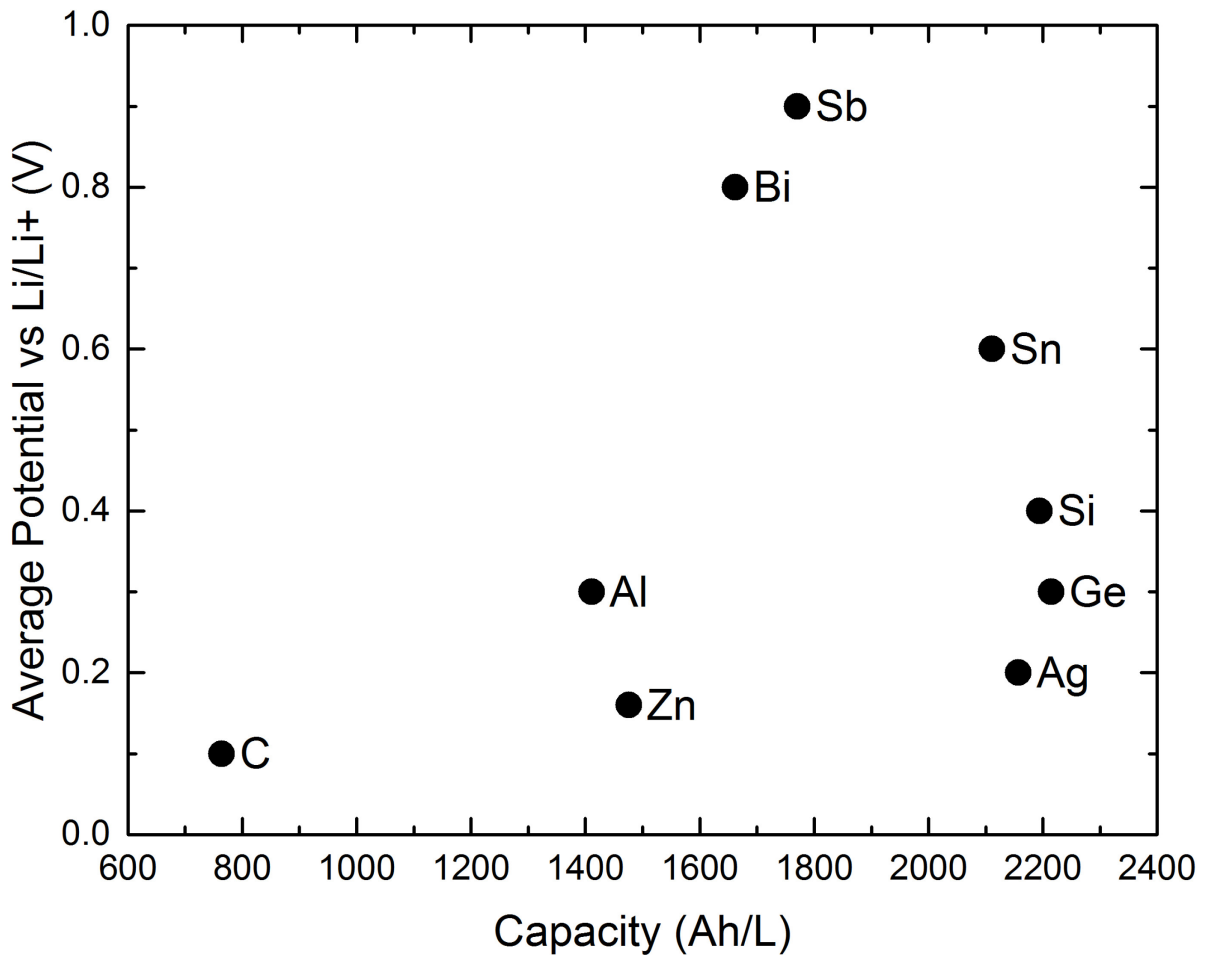
Figure 1.3 Average potential vs. Li/Li+ of elements listed in Table 1.1 plotted against volumetric capacities at fully lithiated volume.[6,8,9,11,14,16]

Alloy negative electrodes have been used in commercial Li-ion batteries by Sony Corp. In 2005 Sony released the Nexelion[TM] Li-ion battery containing a Sn-based anode.[17] Sony's Nexelion[TM] battery was the first commercially available Li-ion battery to use alloy technology as a replacement for graphite. New companies are starting to produce Si anodes, and claim extended cycle life and high energy density in Li-ion cells.[18,19]

Of the materials shown in Table 1.1 and Figure 1.2 Si offers the best combination of abundance, high volumetric capacity, low toxicity, and low potential vs Li/Li^+.[20] Pure Si and Si-based negative electrodes are discussed in more detail throughout this chapter.

1.3 Pure Si Negative Electrodes

One mole of Si can alloy with 3.75 moles of Li at room temperature, resulting in a capacity of 3578 Ah/kg or 2190 Ah/L.[15] As mentioned, each mole of Li displaces approximately 9 mL of volume in an alloy.[6] The molar volume of Si is 12 mL/mol, giving a volume of expansion of 280% when one Si alloys with 3.75 Li. Such large volume expansions cause cracking of the electrode and loss of contact with the current collector on cycling, leading to fast capacity fade and poor performance.[21–24]

Pure Si can be manufactured to be crystalline or amorphous. Crystalline Si can be prepared inexpensively in bulk quantities. Amorphous Si can be prepared by thin-film methods such as sputter deposition which are good for lab scale experiments, but are not cost effective when scaled to batch quantities. Amorphous Si can also be prepared in bulk by delithiation of $Li_{12}Si_7$.[25] The electrochemistry of pure Si has been studied in detail.[15,22,25–28] The lithiation of Si at room temperature has also been studied using first principles models.[29–31]

The reaction of crystalline Si with Li at room temperature has been studied using X-ray powder diffraction (XRD).[15,25] During the first lithiation, crystalline Si is converted to an amorphous $Li_{3.5}Si$ phase. When the potential vs Li/Li^+ drops below 60 mV a crystalline $Li_{15}Si_4$ phase is formed. During delithiation, crystalline $Li_{15}Si_4$ coexists with an amorphous Li_xSi phase. When the $Li_{15}Si_4$ phase disappears only the amorphous phase is present until the electrode is delithiated. During subsequent cycles, crystalline $Li_{15}Si_4$ is formed below 60 mV, but can be avoided if the lower cutoff potential stays above approximately 70 mV.[15,25]

It is thought that rapid capacity fade in crystalline Si electrodes is due to inhomogeneous volume expansions and internal stresses caused by the formation of two-phase regions during cycling.[25] If two-phase regions can be avoided by limiting the lower cutoff voltage during cycling, improvements in capacity retention should be observed. Obrovac et al. found that crystalline Si can cycle for over 100 cycles if the electrode is subject to conditioning cycles and the lower cutoff voltage remains above 170 mV.[27] These cycling conditions work well because only the amorphous Si is cycled after the conditioning cycles and $Li_{15}Si_4$ formation is suppressed.[27] It is important to keep in mind that if Si is to be incorporated into commercial cells it is likely that it will be in the form of an alloy/graphite composite as the addition of a small fraction of Si to a graphite anode can increase the capacity substantially. Since graphite has a low lithiation potential, it may not be practical to cycle to these high lower cutoff voltages and additional methods of $Li_{15}Si_4$ suppression should be explored.

Amorphous Si undergoes a uniform volume expansion during lithiation, therefore two phase regions are not formed and cycling performance can improve. Thin-film

8

amorphous Si has been shown to cycle well and have good capacity retention over many cycles. [32–34] Formation of crystalline $Li_{15}Si_4$ can still occur below 30 mV however; in Si thin films $Li_{15}Si_4$ formation is dependent on film thickness and is only observed when films thickness is above a critical thickness of approximately 2.5 μm. [26] Unfortunately, thin-film amorphous Si prepared by sputter deposition is not economical for use in commercial Li-ion batteries.

1.4 Si Containing Alloy Negative Electrodes

As stated above, high volume expansion at full lithiation (~280%) of Si electrodes leads to poor cycleability when cycled to full capacity. Cycling of Si can also be improved by adding elements that suppress formation of $Li_{15}Si_4$, such as Zn, Ag, and Sn, or by reducing volume expansion by adding an inactive phase, such as Fe. [35–38] Numerous Si-containing alloy negative electrode materials have been studied, including, but not limited to; Si-Sn,[37] Si-C,[39] Si-Fe,[38,40] Si-TiN-C,[39] Si-Zn-C,[41] Si-Al-Sn,[42] Si-Al-Mn,[43] and Si-Sn-C.[44]

Improvement in cell performance can be obtained by incorporating elements that do not alloy with Li into alloy electrodes. Adding an inactive phase to the electrode dilutes the volume expansion, improves cycle life, and increases energy density at a given volume expansion due to lower average voltage compared to pure Si cycled to limited capacity.[6] Fleischauer et al. showed that increasing Mn concentration in Si-Al-Mn thin-film electrodes improved capacity retention, but total specific capacity decreased with increasing Mn.[43] Dong et al. found that $Si_{0.75}Fe_{0.25}$ electrodes exhibited reduced initial capacity, which agrees with the results found by Fleischauer et al., and better cycleability and higher coulombic efficiency (CE) compared to pure Si electrodes.[40]

9

Elements that are active with Li, but with lower specific capacity (and lower volume expansion) than Si have also been shown to improve cycling performance of alloy negative electrodes. Some elements suppress $Li_{15}Si_4$ formation, and thus avoid two-phase regions and high internal stresses during cycling. Zn, Ag, and Sn have all been found to improve cycling for this reason.[45] Zn alloys with Li in a 1:1 ratio and has a theoretical capacity of 410 mAh/g. Hatchard et al. found that Si-Zn thin film electrodes with approximate composition of $Si_{0.4}Zn_{0.6}$ had reversible capacities over 1000 mAh/g and had enhanced cycling performance compared to pure Si.[20] In-situ XRD experiments were used to show that Si-Zn electrodes become amorphous during cycling. Electrodes with greater than 20% content suppressed the formation of $Li_{15}Si_4$ during cycling. Yoon et al. reported good cycling performance for mechanically milled Si-Zn-C composite electrodes.[41] They found that 91% of the initial discharge capacity could be retained for 40 cycles.

One goal of this work is to study the structure and electrochemistry of the Fe-Si-Zn ternary alloy system. According to the phase diagram this system is predicted to comprise three phases: an inactive $FeSi_2$ phase, an active pure Si phase and an active pure Zn phase.[46] However; sputtering is a non-equilibrium process and can lead to formation of metastable phases. Previous electrochemical measurements done on the Fe-Si binary system suggest Fe-Si thin films comprise inactive FeSi and active Si for less than 50 atom % Fe.[38] In this work, Fe-Si-Zn thin-films are predicted to comprise inactive FeSi, active pure Si, and active pure Zn. Fleischauer et al. studied the electrochemistry of Si_xFe_{1-x} thin films and found that capacity decreased nearly linearly from pure Si to 60 atom % Si and dropped to zero at 50 atom % Si.[38] They found that capacity can be

predicted nicely when Si_xFe_{1-x} is assumed to comprise $(2x - 1)$ Si and $(2 - 2x)$ inactive SiFe for $0.5 < x < 1$. In studying this system it is hoped that the advantages of the Si-Fe system (lower volume expansion) and the Si-Zn system (suppression of $Li_{15}Si_4$ formation) could be combined to result in high performance anode materials. The binary systems of Si-Fe and Si-Zn have been previously tested as negative electrode materials for Li-ion batteries. [35,38,47] The electrochemistry and structural characterization of Fe-Zn, a subset in the Fe-Si-Zn ternary system whose electrochemistry has not been previously reported, will also be studied here and leads in to the work done on the Fe-Si-Zn ternary system.

1.5 Organization of Thesis

Chapter 2 outlines the experimental techniques used in this work, including material preparation and characterization. Materials in this thesis were prepared by combinatorial sputtering and horizontal roller milling and were characterized using XRD, Mössbauer effect spectroscopy, electron microprobe, and electrochemical methods.

Chapter 3 discusses the sputtered Fe_xZn_{1-x} binary system in detail. The activity of Fe_xZn_{1-x} alloys towards lithium were predicted using a macroscopic atom model. Electrochemical measurements were performed on a range of compositions and ex-situ Mössbauer and x-ray diffraction measurements were performed on a $Fe_{0.1}Zn_{0.9}$ electrode. The Fe-Zn binary system was studied as preliminary work for studying the Fe-Si-Zn ternary system.

Chapter 4 focuses on the Fe-Si- Zn ternary system. Structural characterization and electrochemistry of a range of compositions is discussed. Finally, Chapter 5

summarizes the negative electrode materials examined in this thesis and future work in the area is suggested.

Chapter 2 Experimental Techniques

2.1 Combinatorial Sputtering

Sputter deposition is a technique that involves bombarding a source material (target) with energetic ions, ejecting atoms from the target and depositing them on a substrate. The target is kept at a high negative potential (hundreds of volts) by attaching it to a power supply while the chamber and substrate are kept at ground potential. As a result, the target becomes the cathode and the chamber and substrate become the anode of the sputtering system. When the potential difference between the anode and cathode is large enough, the sputtering gas (typically Ar) becomes ionized and is referred to as a plasma. Ions in the plasma (Ar^+) accelerate toward the cathode and collide with the target, ejecting atoms from the target material. The ejected target atoms are then deposited on the substrate. The plasma is sustained during deposition by secondary electrons being ejected from the target and ionizing more Ar atoms. A simple schematic of the sputtering process is shown in Figure 2.1.
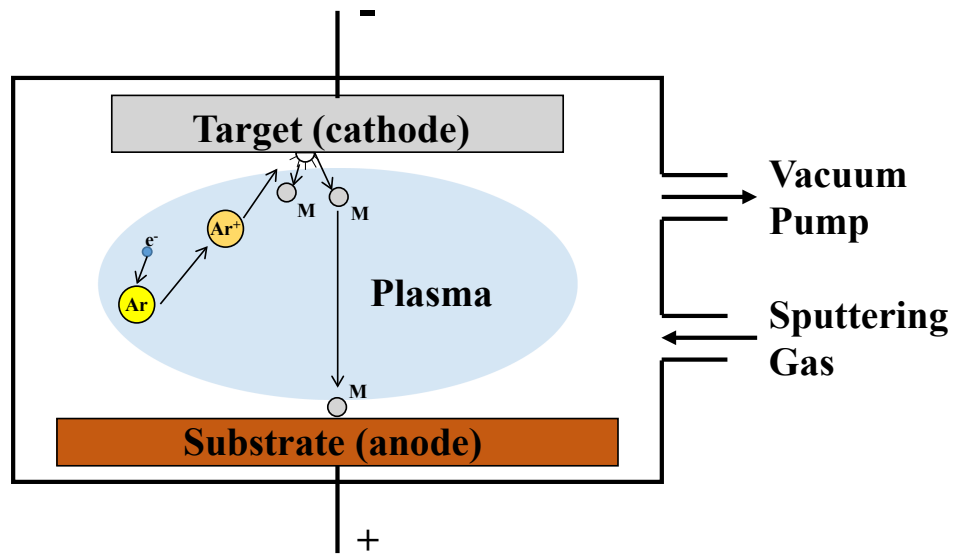
Figure 2.1 Simple schematic of the sputtering process.

Secondary electrons can only ionize Ar atoms over the short path from the cathode to anode. Magnets can be placed behind sputtering targets to augment the plasma near the target and lengthen the travel time of secondary electrons, increasing the number of Ar^+ ions they can create. The magnets behind the target create magnetic fields that cause secondary electrons to travel in a spiral path towards the target. This increases their traveled distance and the likelihood that an electron will collide with an Ar atom. The modification of incorporating magnets into the sputtering apparatus is referred to as magnetron sputtering.

Thin film libraries were produced using a Corona Vacuum Coater model V3-T magnetron sputtering system. Base pressures of $< 4 \times 10^{-7}$ Torr are obtained by evacuating the vacuum chamber using a Varian 500 L/s turbo pump backed by a roughing pump. A Polycold PFC-400 cryopump is used to remove water vapour from the chamber. Ar gas is used to maintain the pressure at approximately 1 mTorr during sputter deposition. The sputtering system has five magnetrons separated by 60° which use a pair of rare-earth Nd-Fe-B concentric magnets. The magnetrons are water cooled to dissipate any heat generated during the sputtering process. Each magnetron can be controlled individually, so the system has the ability to accommodate five unique sputtering targets. Further details of the combinatorial sputtering system have been described by Dahn *et al.*.[48]

The sputtering system has the ability to produce continuously varying binary and ternary libraries by placing different masks over the targets. Constant masks are placed in front of targets when a uniform mass deposition along the sputtering track is desired. A modified constant mask may be required if a constant mask does not produce a uniform deposition along the track. Linear-in or linear-out masks are placed in front of

targets when mass deposition along the track is required to increase radially inward or radially outward, respectively. The substrate table rotates continuously at 15 rpm to ensure sufficient atomic level mixing during deposition.

In this work a binary library refers to a library comprising two elements varying continuously in the radial direction along the sputtering annulus. A binary library is fabricated using constant masks over the sputtering target of element "A" and linear-in or linear-out masks over the target of element "B". A minimum of two unique sputtering targets are required to produce a binary library. A pseudobinary library refers to a library comprising three elements with two elements deposited in a fixed molar ratio along the sputtering radius and the third varying continuously. A pseudobinary library is fabricated using constant masks over targets of two elements "A" and "B", and a linear-in or linear-out masks over the target of element "C". A minimum of three unique sputtering targets are required to produce a pseudobinary library. A schematic of the sputtering table and substrates used in producing binary and pseudobinary libraries is shown in Figure 2.2. A ternary library refers to a library comprising three elements, with two of the elements varying continuously in orthogonal directions. A constant mask is placed in front of the target of element "A" and linear-in or linear-out masks are placed in front of elements "B" and "C". A schematic of the substrate table used for producing ternary libraries is given in Figure 2.3. An orthogonally varying library is obtained by rotating the substrates that are mounted on subtables on the rotating substrate table. The techniques used to obtain ternary libraries have been presented in more detail by Fleischauer *et al.*.[49]

Details of the sputtered libraries will be given in their respective Chapters. Three types of 5.08 cm diameter targets were used in this work: Si targets (99.99% purity,

Williams Advanced Materials), Fe targets (produced by stacking two 50 mm diameter disks cut from 0.7 mm thick sheets of grade 1008 low carbon steel), and Zn targets (99.99% purity, Kurt J. Lesker Company). A chrome plasma scrubber electrode was mounted on one of the magnetrons for ternary sputtering runs.
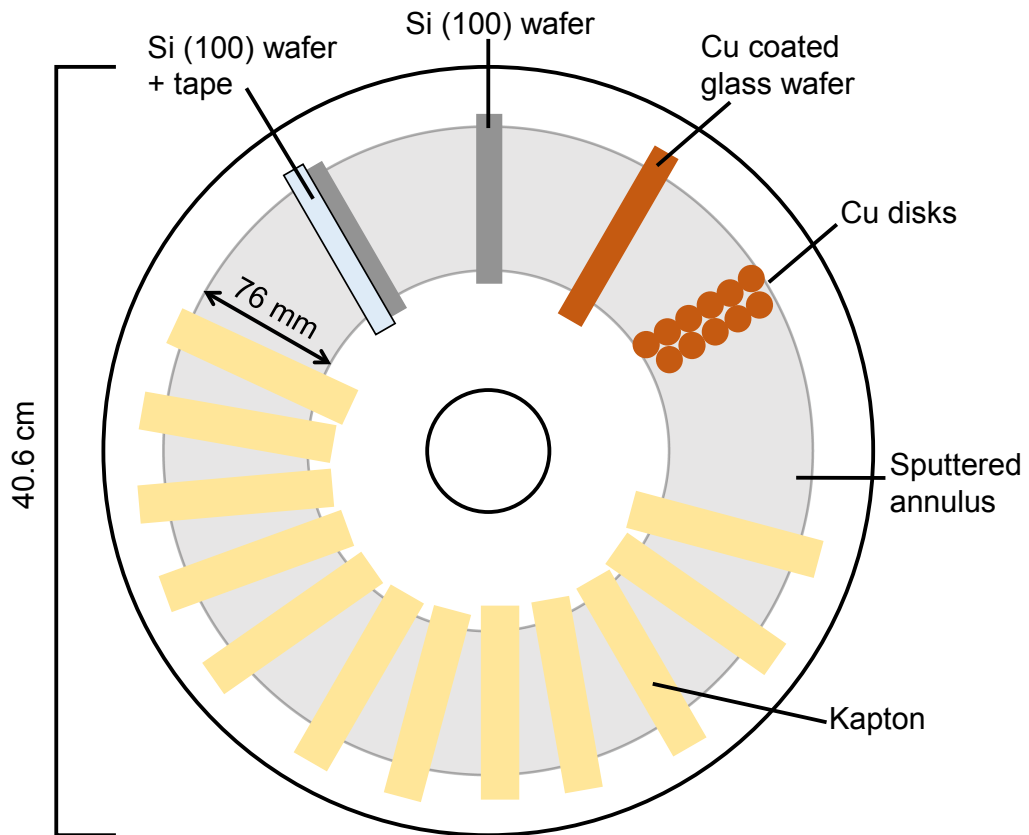
Figure 2.2 Binary sputtering table with substrates used in this work.
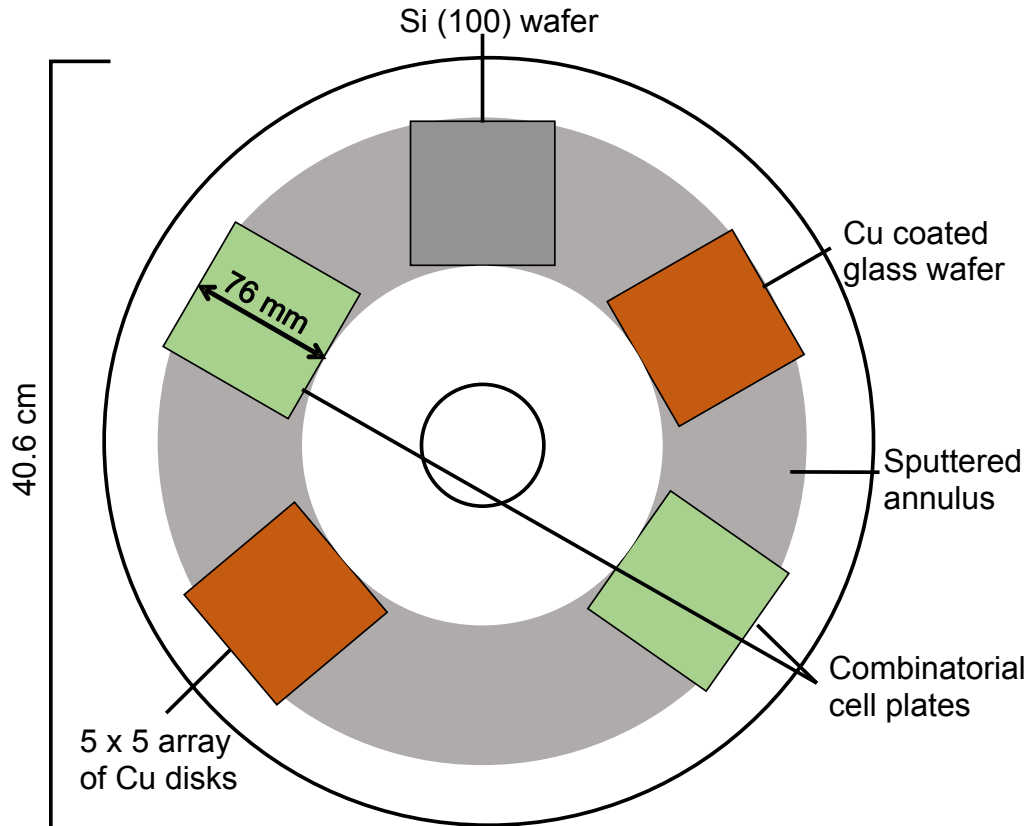
Figure 2.3 Schematic of the substrate table used in producing ternary libraries. The five substrates are mounted on sub-tables which move during rotation of the main substrate table.

2.2 X-Ray Diffraction

X-ray diffraction (XRD) is a commonly used technique for determining the structure of materials. XRD patterns can provide information about phase composition, grain size, and crystal structure of materials. Consider in-phase X-ray beams incident on parallel planes of atoms separated by a distance, d. When the incident X-rays hit the sample they will be scattered by the electrons. The beams can interfere constructively or destructively. To have constructive interference, Bragg's law must be satisfied:

$$n\lambda = 2d \sin \theta, \tag{2.2}$$

17

where n is an integer, λ is the wavelength of the incident X-rays, chosen to be similar to atomic spacing distance, d is spacing between planes of atoms, and θ is the incident angle of the X-ray beams.

Figure 2.4 outlines the basic principles behind X-ray diffraction measurements. For an X-ray source with a known wavelength, θ can be determined experimentally and the plane spacing of the atoms in the crystal structure is easily determined. An X-ray diffraction pattern is a plot of intensity of scattered X-ray beams (peak intensity) versus the scattering angle, 2θ, the angle between incident and diffracted X-ray beams.

The size of crystallites, t, in the material can be estimated using the Scherrer equation:

$$w = \frac{K\lambda}{t \cos\theta},$$ (2.3)
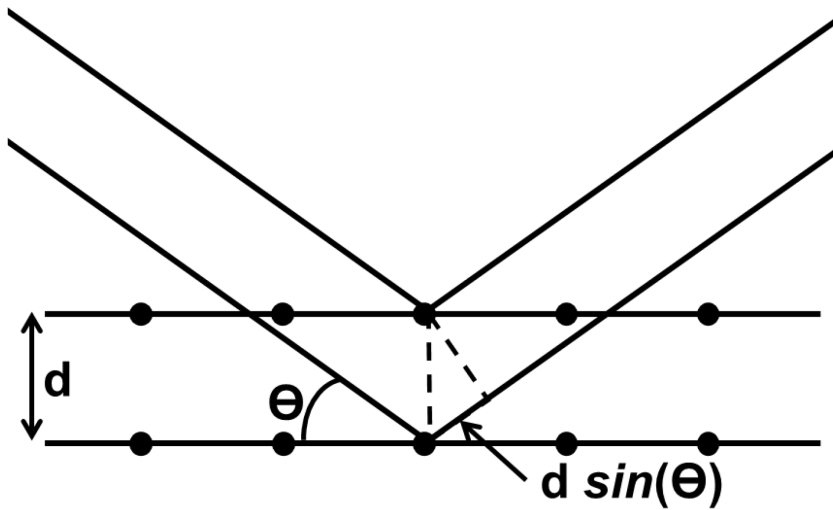
Figure 2.4 Illustration of Bragg's Law of diffraction.

where K is a dimensionless crystallite shape factor usually taken to be 0.9 for unknown samples, w is the full width at half maximum of the peak in degrees, λ is the X-ray wavelength, and θ is the incident angle. Broad peaks are observed for materials that have very small crystalline regions. Broad peaks are characteristic of materials lacking long range crystallographic order such as nanocrystalline or amorphous materials.

XRD patterns were collected using two different diffractometers. A Bruker D-8 Discover X-ray diffractometer equipped with a Cu target and CuK_α monochromator was used for thin-film libraries deposited on Si (100) wafers. The Bruker D-8 is equipped with translational stage that can be programmed to collect data at multiple points subsequently. This allows diffraction patters to be collected as a function of position and composition. The Bruker D-8 is also equipped with a VÅNTEC-2000 area detector. The area detector has a 14×14 cm^2 active sensor area with 2048×2048 pixels. The X-ray beam was incident on the sample at an angle of 6°, which does not satisfy the Bragg condition for Si; and as a result, the Si wafer has zero background. A Rigaku Ultima IV diffractometer with a CuK_α (1.54 Å) radiation source with a diffracted beam monochromotor and scintillation detector was used for powder samples. Powder samples were recovered under Ar and placed in an air sensitive sample holder for measurements.

2.3 Mössbauer Effect Spectroscopy

Many of the materials studied in this thesis are amorphous or nanostructured and X-ray diffraction experiments cannot provide insight into the structure of these materials. Since all of the materials studied here are Fe containing alloys, Mössbauer effect spectroscopy can be used to probe the structure and learn more about these materials at very high (atomic) resolution. The Mössbauer effect is defined as emission or absorption

of a γ-ray photon without loss of energy due to recoil of the nucleus or thermal broadening. Detailed information on Mössbauer effect spectroscopy is available elsewhere.[50,51] Some basic concepts will be illustrated here.

2.3.1 Recoil Free Fraction

If the energy of an atom in an excited state is

$$E = E_e - E_g,$$

(2.4)

where E_e and E_g are the excited and ground state energies of the atom, respectively, then the total energy of the atom with mass M moving at some velocity V_x will be

$$E_{tot} = E + \frac{1}{2} M V_x^2.$$

(2.5)

If a γ-ray photon is emitted from the nucleus the total energy is now

$$E_{tot} = E_\gamma + \frac{1}{2} M (V_x + v)^2,$$

(2.6)

where E_γ is the energy of the emitted photon and v is the change in velocity of the nucleus. If total energy is conserved we have

$$E - E_\gamma = \frac{1}{2} M V_x v + \frac{1}{2} M v^2 = E_D + E_R,$$

(2.7)

where E_D and E_R are Doppler effect energy and recoil kinetic energy of the nucleus. The mean kinetic energy per atom in a gas with random thermal motion is

$$E_K = \frac{1}{2} M \bar{V}_x^2 \cong \frac{1}{2} k_B T,$$

(2.8)

where k_B is the Boltzmann constant and T is the absolute temperature. From Equations *2.7* and *2.8* the Doppler effect energy is

$$E_D = 2\sqrt{\bar{E}_K E_R}.$$

(2.9)

The energy distributions for emission and absorption of a γ-ray photon will be Gaussian with a small energy overlap region. This is called the recoil free fraction and is illustrated in Figure 2.5.

The recoil energy of a single free nuclei is on the order of $10^{-4} - 10^{-1}$ eV and bond energies are on the order of $1 - 10$ eV. Since the bond energies of atoms are much larger than the recoil energy of a free nuclei, the emitting atom cannot recoil freely, but instead the whole crystal recoils. This means the effective mass, M, is much larger and the recoil energy,

$$E_R = {E_\gamma^2}/{2Mc^2},$$ (2.10)

approaches zero. The Doppler effect energy also approaches zero according to Equation *2.9*. When recoil energy is transferred to the crystal (i.e. does not lead to a change in the crystal vibrational energy), the emission and absorption peaks will shift to zero and narrow and the overlap between them grows. The probability of this happening is called the recoil free fraction, f, and is given as

$$f = 1 - {E_R}/{\hbar\omega},$$ (2.11)
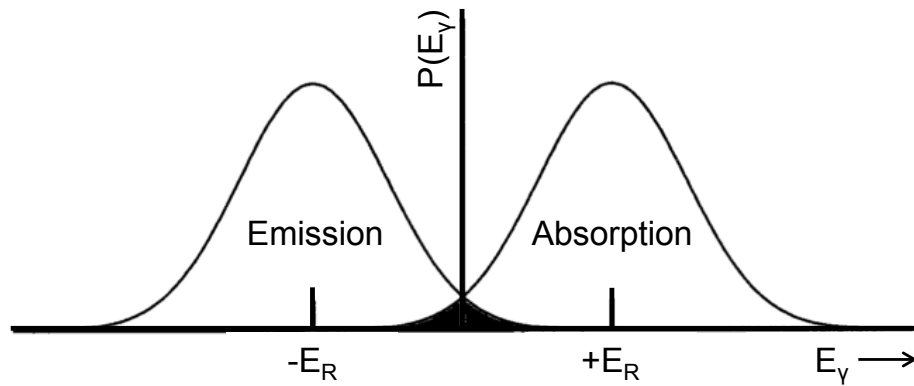
Figure 2.5 Schematic of energy distributions for emission and absorption. The shaded area is the resonance overlap region. Figure adapted from Reference 51.[51]

where ω is the photon angular frequency.

For Mössbauer spectroscopy to be a practical technique, the availability of excited state nuclei to produce photons is necessary. ^{57}Fe is often used for Mössbauer experiments because it has a natural abundance of ~2% in bulk Fe and γ-ray photons can be produced using a ^{57}Co radioactive source, which has a half-life of 270 days. The electron capture decay of ^{57}Co to ^{57}Fe is shown in Figure 2.6 along with respective half-lives and energies. The $3/2 \rightarrow 1/2$ transition is relevant for the Mössbauer effect.

The energy of incident γ-rays must be modified to probe energy levels of the Mössbauer nuclei. This is achieved by Doppler shifting the energies of γ-rays by moving the source. The range of energies probed is given by

$$r = E_\gamma \, {v_s}/{c},$$ (2.12)
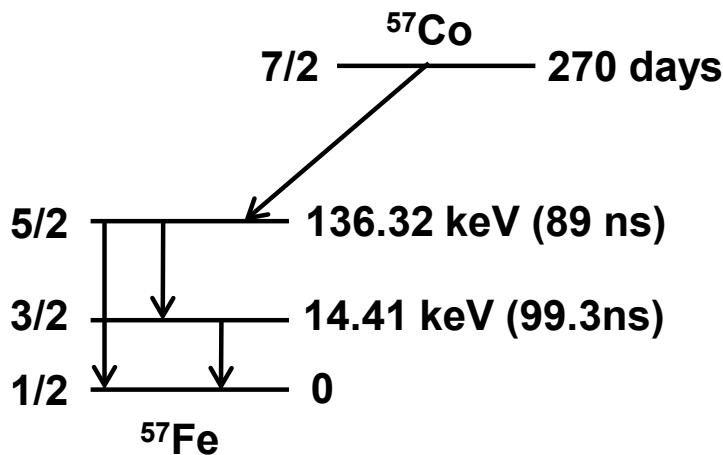
Figure 2.6 Electron capture decay of ^{57}Co.

where v_s and c are the source velocity and speed of light, respectively. Velocities between -3 mm/s to + 3 mm/s and -8 mm/s to + 8 mm/s were used to scan the range of absorber energies in this work. Calibrations are done with α-Fe which has well-known features.

2.3.2 Hyperfine Interactions

There are three types of hyperfine interactions that can be used to probe the local Fe environments in the material. These are the isomer shift, quadrupole splitting, and Zeeman effect. These interactions will differ depending on the environment of the Fe nuclei in a material and can be characterized by computer fitting of the Mössbauer spectrum.

The isomer shift (δ) is a measure of differences in s-electron densities of the source and absorber. If the source and absorber are in identical chemical environments, the center shift will be identically zero. A difference in chemical environments of the source and absorber results in the resonant peak of the spectra being displaced from zero. The isomer shift is measured relative to a standard, α-Fe in this work, and is given as

$$\delta = const \times \{|\psi_s(0)_A|^2 - |\psi_s(0)_S|^2\}, \tag{2.13}$$

where *const* is a nuclear term which is constant for a given transition and $|\psi_s(0)_A|^2$ and

$|\psi_s(0)_S|^2$ are the s-electron densities at the probe nuclei in the absorber and source,

respectively.[51] For ^{57}Fe Mössbauer spectroscopy a positive isomer shift indicates a

decrease in s-electron density in the absorber compared to the source. The isomer shift is

defined for 0 K. The center shift that is discussed in following chapters is the isomer

shift plus a relativistic temperature dependent contribution.

Quadrupole splitting arises from a non-spherical charge distribution in a nucleus

with total spin, *J*, greater than ½.[51] Nuclei with *J* greater than ½ have a quadrupole

moment which can interact with the electric field gradient that results from a non-

spherical charge distribution according to

$$E_Q = \frac{e^2 qQ}{4J(2J-J)}[3m_J^2 - J(J+1)], \tag{2.14}$$

where m_J is the *z* component of the total spin, *Q* is the nuclear quadrupole moment for the

resonant isotope, and *eq* is the maximum value of the electric field gradient.[51] The

magnitude of the quadrupole interaction is the product of *eQ* and *eq*. Presence of a

quadrupole splitting results in the Mössbauer spectra for the 3/2 → 1/2 transition having

two lines of equal intensity (if the sample is crystallography isotropic). The center of the

quadrupole split doublet is the isomer shift.

The presence of a magnetic field also alters a Mössbauer spectrum and this is

known as the nuclear Zeeman effect. For a magnetic field with a flux density *H*, the

spectrum will be split into energy levels according to

$$E_m = -g\mu_N H m_J, \tag{2.15}$$

where g is the nuclear g factor, μ_N is the nuclear magneton, and m_J is the magnetic

quantum number representing the z component of J.[51] Allowed nuclear transitions for

^{57}Fe corresponding to quadrupole splitting and Zeeman splitting are shown in Figure 2.7.

Room temperature ^{57}Fe Mössbauer effect measurements were performed using a

See Co. constant acceleration spectrometer equipped with a Rh^{57}Co source. For thin film

Mössbauer experiments, films were deposited on 10.2 cm × 2.54 cm strips of Kapton and

placed on top of each other in stacks of 12, in order to obtain a reasonable Fe loading for

Mössbauer measurements. A rectangular slot exposed the desired film area to the

(a)

$J = 3/2$

$|m_J| = 3/2$

$|m_J| = 1/2$

$J = 1/2$

$|m_J| = 1/2$

(b)

$J = 3/2$

$m_J = -3/2$

$m_J = -1/2$

$m_J = +1/2$

$m_J = +3/2$

$J = 1/2$

$m_J = +1/2$

$m_J = -1/2$
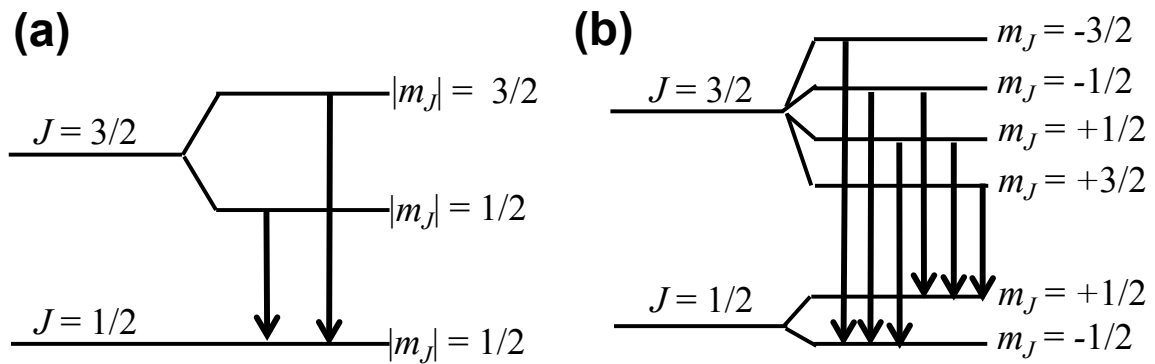
Figure 2.7 Allowed nuclear transitions in ^{57}Fe for (a) quadrupole splitting and (b) Zeeman splitting.

detector. Spectra were taken in 4.5 mm or 9 mm steps. For powder Mössbauer

measurements, powders were transferred to a sample holder which was heat sealed in

aluminized Mylar under Ar.

To obtain sufficient electrode material for ex-situ Mössbauer measurements, a

large area electrode was made by first coating a 12:8 w/w mixture of Super P carbon

clack (Erachem, Europe) and PVDF (HSV 900, KYNAR) from an NMP (anhydrous,

99.5%, Sigma Aldrich) slurry onto a Cu foil with a 0.002" doctor blade and drying in air

at 120°C for 45 minutes. This formed a conductive release layer on the Cu foil onto which a thin film of constant $Fe_{0.08}Zn_{0.92}$ composition was sputtered using constant composition masks for both the Fe and Zn targets. The film was then cut into 6 cm × 6 cm electrodes and placed over the 8 × 8 lead pattern of the combinatorial cell described by Al-Maghrabi *et al.*[52] with a Li counter/reference electrode. Such cells were cycled to various states of charge and electrode material was recovered from combinatorial cells by scraping electrode material off of the Cu substrate in an argon filled glovebox. Typically 60 - 70 mg of electrode material could be recovered from each cell. The recovered powder was transferred to a sample holder which was heat sealed in aluminized mylar under Ar.

The velocity scales for all spectra were calibrated relative to room temperature α-Fe. All Mössbauer spectra were analyzed with the Recoil software package (©1998 Ken Lagarec and Denis G. Rancourt).

2.4 Electron Microprobe

Atomic compositions of the libraries presented in this work were determined using a JEOL-8200 Superprobe electron microprobe with wavelength dispersive spectroscopy (WDS). The spectrometer is equipped with a translational stage, allowing data to be collected for multiple points on one substrate. A 5 keV electron beam bombards the sample and interacts with the atoms in the film. Inner shell electrons are ejected from the atoms and outer shell electrons fill the vacant shell, resulting in characteristic X-rays being emitted. Energies of emitted X-rays are well-defined for different elements and are used to determine the composition of the sample. Intensities of X-rays from the sample are compared to X-rays produced from standards of known

26

composition. Relative ratios of the elements are obtained by measuring the intensities of the emitted x-rays and performing computational corrections related to atomic number (Z), absorption (A), and fluorescence (F). This correction is referred to as the *ZAF* correction.

Fe-Zn binary thin-film libraries were deposited on Si (100) wafers for electron microprobe measurements. Fe-Si-Zn libraries were deposited on Cu coated glass plates for electron microprobe measurements in order to distinguish the deposited Si from the substrate and obtain reliable data. Data were collected at 20 points along the radius of the sputtered annulus for binary and pseudobinary libraries. Data were collected on an 8 × 8 grid of points on a 7.62 cm × 7.62 cm square for ternary libraries.

2.5 Electrochemical Characterization

Electrochemical performance of materials is dependent on structure and composition. Slight changes in material properties can lead to significant changes in electrochemical performance. The materials fabricated in this thesis are tested as positive electrode materials in Li half-cells, but would be used as negative electrode materials in full cells. The chemical potential of Li in the negative electrode material is higher than that of Li in the positive electrode material. During discharge of a cell Li ions are transferred from the electrode with high chemical potential of Li (negative electrode) to the electrode with low chemical potential of Li (positive electrode). During discharge of a half cell, Li ions are transferred from Li metal (higher chemical potential of Li) to the test material (lower chemical potential of Li), making the test materials positive electrodes in half cells. However, during discharge of a full cell Li ions will be

transferred from the test material to a positive electrode material such as as $LiCoO_2$ or

$Li(Ni_xMn_yCo_{1-x-y})O_2$, making the test materials negative electrodes in commercial cells.

The capacity is charge stored per unit mass (specific capacity) or unit volume

(volumetric capacity) and is given by:

$$capacity_{m,v} = \frac{Q}{m,v} \qquad (2.16)$$

where Q is charge in mAh, and *m* or *v* is the active mass or volume of the fully lithiated

electrode, respectively. The "active" material in the electrode refers to the material that

reacts reversibly with Li. For sputtered film electrodes, the entire deposited mass is the

active mass. Electrodes prepared from powder samples comprise alloy powder, binder,

and conductive diluent. The active mass for powder sample electrodes is the of the alloy

powder only.

Important electrochemical characteristics of the test materials are potential vs

Li/Li^+, capacity, irreversible capacity (IRC), coulombic efficiency, and cycle life. The

potential vs Li/Li^+ at which the electrode lithiates and delithiates should be low for a

good negative electrode material. The difference between the average charge and

discharge voltage is referred to as polarization. Polarization should be minimized as it

corresponds to energy lost during cycling.

Capacity provides information on how many Li ions react with the electrode

material. Capacity data can help predict what active and inactive phases are present in

the electrode material. Irreversible capacity (IRC) is the difference between the first

discharge and charge capacities and is often given as a percentage of the first discharge

capacity. This loss of capacity is generally due to Li being consumed during surface

electrolyte interphase (SEI) formation. Coulombic efficiency (CE) is the ratio of the

amount of lithium inserted in the electrode to the amount of lithium removed and is calculated by dividing the charge capacity by discharge capacity for one cycle. If CE is 100%, a cell should cycle forever. Cycle life is the number of cycles the material can undergo until the capacity drops below a certain threshold, usually 80% of first cycle capacity.

In this work, amorphous materials are desirable because they do not form two-phase regions during cycling. The formation of two-phase regions during cycling causes inhomogeneous volume expansions and high internal stresses in the electrode resulting in rapid capacity fade. Two-phase regions formed during cycling can easily be seen as peaks in plots of differential capacity (dQ/dV) versus potential. Differential capacity can be easily obtained using the relation:

$$\left(\frac{dQ}{dV}\right) = \left(\frac{dQ}{dt}\right)\left(\frac{dt}{dV}\right),$$ (2.17)

where (dQ/dt) is the current, I. Sharp peaks in a differential capacity plot are analogous to plateaus in the voltage curve and are characteristic of two-phase regions. Amorphous Si with no $Li_{15}Si_4$ formation during cycling shows two broad humps in differential capacity during delithiation. If $Li_{15}Si_4$ is formed during cycling a sharp peak at 0.4 V during delithiation is observed.[26] Figure 2.8 shows delithiation portions of two amorphous Si cells. The red curve is characteristic of amorphous Si with $Li_{15}Si_4$ formation supressed during cycling and the black curve indicates $Li_{15}Si_4$ formation is not suppressed during cycling with a sharp peak at 0.4 V. The red curve is from the first cycle of an electrode comprising approximately 80 atom % Si with 5 atom% Zn and 10 atom % Fe. Zn has been previously shown to suppress $Li_{15}Si_4$ formation in Si thin-film electrodes.[35] The addition of Fe to Si causes a depression in the discharge voltage, which

may also aid in the suppression of $Li_{15}Si_4$ formation and will be discussed in Chapter 4.

The black curve is from cycle 6 of the same electrode. Repeated insertion and removal of

Li into the electrode may cause the Zn that was dispersed throughout the electrode to

aggregate, giving rise to larger Si regions that can more easily form $Li_{15}Si_4$. Similar

mechanisms for $Li_{15}Si_4$ formation have been proposed for SiAg electrodes and will be

discussed in Chapter 4.[36]

2.5.1 Coin-Type Cells

Coin cells were used for electrochemical testing of sputtered libraries and

mechanically milled powders. In the case of sputtered libraries, the material was

deposited on 1.25 cm^2 diameter Cu disks and used as electrodes. Electrode mass was

determined by weighing the Cu using a Sartorious SE-2 microbalance (0.1 μg precision)

before and after sputter deposition.)
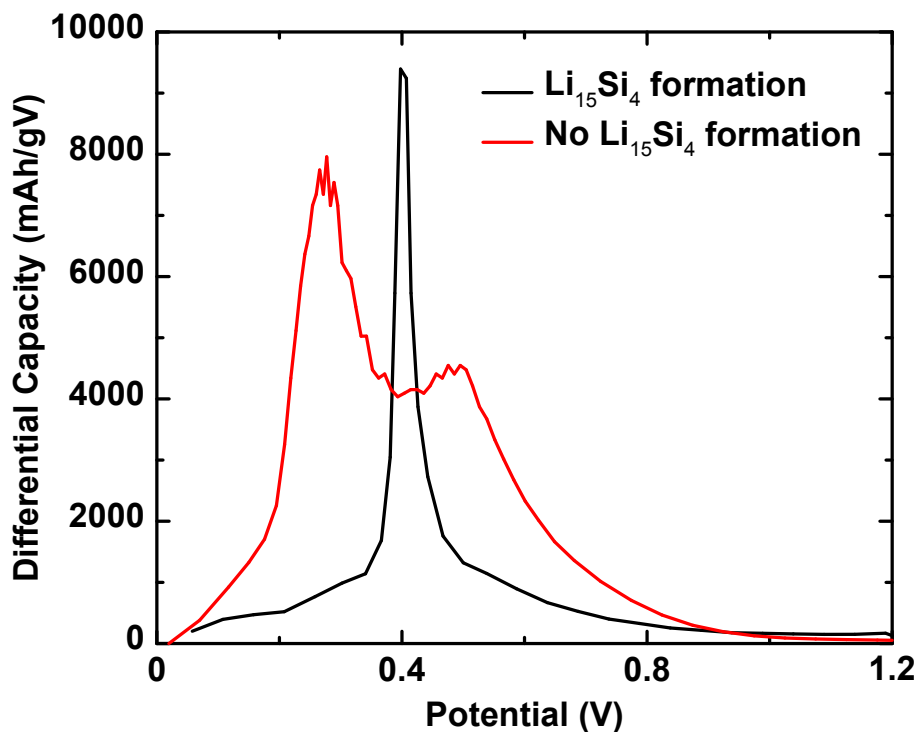
Figure 2.8 Charge portion of two amorphous Si voltage curves. The red curve shows no evidence of $Li_{15}Si_4$ formation. The black curve shows evidence of $Li_{15}Si_4$ formation.

Electrodes deposited on Cu disks were incorporated into 2325 coin cells with Li metal counter electrodes and 1 M $LiPF_6$ in ethylene carbonate (EC) / diethyl carbonate (DEC) in a 1/2 v/v ratio or 1 M $LiPF_6$ in ethylene carbonate (EC) / ethyl methyl carbonate (EMC) / fluoroethylene carbonate (FEC) 2/7/1 v/v/v or 1 M $LiPF_6$ in EC/DEC/FEC 3:6:1 v/v/v electrolyte (all from BASF, < 50 ppm H_2O), depending on the library. For Fe-Zn libraries electrodes were separated with two layers of Celgard 2301 separator and one layer of polypropylene blown microfiber separator (3M Co.). For ternary Fe-Si-Zn libraries electrodes were separated with two layers of Celgard 2301 separator. All cell assembly was performed in an Ar-filled glove box.

Cells were cycled at 30°C with a Maccor Series 4000 Automated Test System. For Fe-Zn binary libraries cells were cycled from 0.005 V to 1 V at a C/40 rate and trickled until a C/80 rate was reached at the lower voltage limit during discharge (lithiation), where C was calculated assuming Zn alloys with Li in a 1:1 ratio and all Zn present in the electrode is active. For Fe-Si-Zn libraries, cells were cycled from 0.005 V to 1.2 V at a C/10 rate and trickled until a C/20 rate was reached at the lower voltage limit during discharge (lithiation). The C rate for Fe-Si-Zn cells was calculated assuming that three phases are present in the sputtered film: FeSi, Si, and Zn and that the FeSi phase is inactive, the remaining Si alloys with 3.75 Li per Si, and all the Zn present is active and alloys with 1 Li per Zn.

Chapter 3 Fe-Zn System

3.1 Introduction and Background

As stated previously, alloy negative electrode materials are of interest for use in Li-ion rechargeable batteries due to their high volumetric and gravimetric capacities and low average voltages.[53] Zn and Al alloy with Li in a similar manner. Each reacts electrochemically with one equivalent of Li, corresponding to volumetric capacities of 1478 Ah/L and 1411 Ah/L, respectively. The cycle life of crystalline Zn and Al is poor because of 2-phase regions encountered during their lithiation.[54] Despite their similarities, Al-based alloys have been studied extensively as negative electrodes, while Zn containing alloy materials have not been well explored.

Previous studies on Zn negative electrodes for Li-ion batteries have reported poor cycle life for pure Zn electrodes.[55–57] Hwa *et al*. performed ex-situ x-ray diffraction studies on Zn electrodes and reported that lithiation and delithiation of a Zn electrode at room temperature follow different mechanisms:[55]

$$\text{lithiation: } Zn \xrightarrow{Li} \alpha\text{-}LiZn_4 \xrightarrow{Li} \alpha\text{-}Li_2Zn_3 \xrightarrow{Li} LiZn, \tag{3.1}$$

$$\text{delithiation: } LiZn \xrightarrow{-Li} \alpha\text{-}Li_2Zn_3 \xrightarrow{-Li} LiZn_2 \xrightarrow{-Li} \alpha\text{-}Li_2Zn_5 \xrightarrow{-Li} \alpha\text{-}LiZn_4 \xrightarrow{-Li} Zn. \tag{3.2}$$
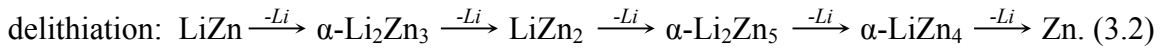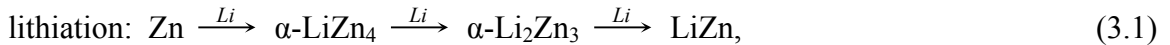
While the delithiation of Zn follows the Li-Zn binary phase diagram shown in Figure 3.1, $LiZn_2$ and $\alpha\text{-}Li_2Zn_5$ are not formed during lithiation.
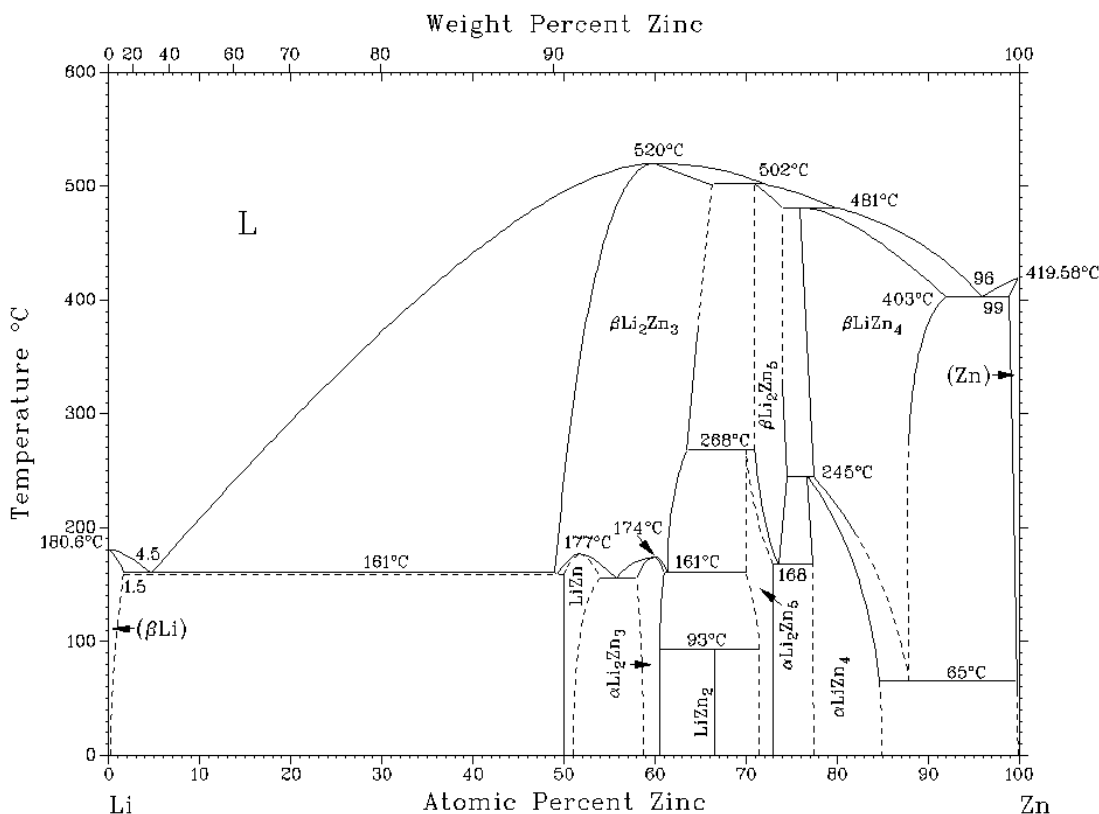
Figure 3.1 Li-Zn binary phase diagram.[58]

Active elements are commonly alloyed with other elements to improve cycling

performance by making the active phase amorphous or nanostructured and by reducing

volume expansion.[53] Incorporating Zn into composite electrode materials (Zn-C, Zn-

Al$_2$O$_3$-C, Zn-Fe) has been shown to improve performance compared to pure Zn negative

electrodes.[55–57] Purcell *et al*. recently showed that the addition of carbon to a Zn

electrode improved cycle life and CE.[57] They also found that electrolyte decomposition

at the electrode surface increases with Zn content in a Zn-C composite electrode,

resulting in "slippage" of the voltage curves. Purcell *et al*. suggested that electrolyte

decomposition may also occur in other Zn-based composite electrodes, such as the Zn-

Al$_2$O$_3$-C system presented by Hwa *et al*.[55] Fujieda *et al*. studied the electrochemistry of

Fe-doped Zn electrodes prepared by electrodeposition on Ni wire and heat treatment in N_2.[56] They found that adding 2 wt.% Fe to Zn electrodes improved cycling efficiency and suggested that the formation of a supersaturated Fe-Zn in the Zn rich region does not inhibit the reaction between Li and Zn.

In an attempt to improve the cycle life of Al, Fleischauer *et al*. studied sputtered Al-M (M = a transition metal) thin films.[59] These studies showed that amorphous Al-based alloys can be formed when the M content is increased; however the capacity in these amorphous alloys is near zero when M content is above 15 atom %.[59,60] Fleischauer *et al*. presented a phenomenological model based on the macroscopic atom model of de Boer *et al*. to describe observed capacity as a function of transition metal content. They predicted that Al-M alloys should be active to lithium for M content below 33-65 atom %, but found that only 12 atom % Fe was required to render Al-Fe electrodes inactive, coinciding with the formation of an amorphous Al-Fe phase.[59] They suggested that increasing Fe content creates $Al_{12}Fe_2$ clusters in the film, which become inactive when they aggregate as the Fe content is increased. The sharp drop in capacity with increased Fe above the fcc solubility limit was attributed to each additional Fe atom inactivating 12 Al atoms.

In order to evaluate whether Fe-Zn alloys could be useful as negative electrodes, it would be valuable to predict the activity of Fe_xZn_{1-x} alloys towards lithium by means of density function theory (DFT) calculations. Online DFT routines made available by the Materials Project, [61,62] can be used to predict that the ζ ($FeZn_{13}$) phase will be active toward lithium. Predicting the activity of more Fe-rich phases is more complicated.
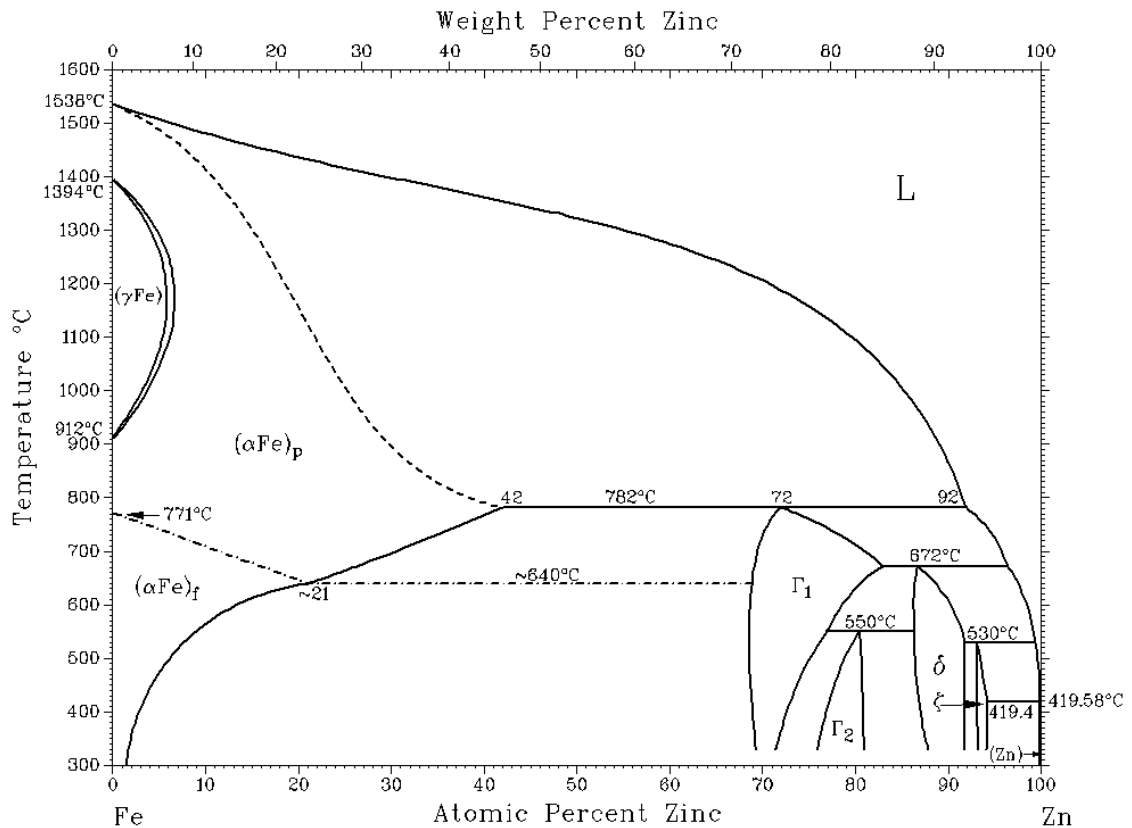
Figure 3.2 Fe-Zn binary phase diagram.[55]

The Fe-Zn binary phase diagram is shown in Figure 3.2. Fe-rich phases include δ ($FeZn_{10}$), Γ_1 (Fe_5Zn_{21}), and Γ (Fe_3Zn_{10}), which comprise 555, 408, and 52 atoms per unit cell, respectively.[63] In more recent studies, two distinct Zn-rich phases (δ_{1k} and δ_{1p}) have been found to exist in the δ region.[64–66] Okamoto *et al.* performed a structure refinement on the δ_{1p} ($Fe_{13}Zn_{126}$) phase and found it had a hexagonal unit cell comprising 566 atoms.[65] The δ_{1k} phase is slightly more Fe rich and is thought to have a superlattice structure based on the δ_{1p} structure, but the crystal structure has not been refined.[66] Large (>400 atoms) unit cells make DFT calculations prohibitive. The Γ (Fe_3Zn_{10}) phase is a potential starting point for DFT calculations with 52 atoms per unit cell; however, the positions of all atoms within the unit cell are not known and so DFT calculations cannot

35

be easily performed.[67–69] As an alternative, a macroscopic atom model is used here to predict activity of Fe_xZn_{1-x} alloys toward lithium, as described previously by Fleischauer *et al.* for the Al-Fe system.

In the present work sputtered Fe_xZn_{1-x} alloys were studied as potential negative electrodes in lithium cells. The microstructure and electrochemical behavior of these alloys are described using results from ex-situ Mössbauer and XRD studies.

3.2 Film Characterization

The three libraries had composition ranges of x = 0 - 0.35, 0 - 0.45, and 0.02 - 0.55. The libraries had constant Zn content and an Fe content that varied along the radius of the sputtered annulus. Film thickness measured for all three runs was found to be 1 - 3.9 μm, depending on the library and composition. Electron microprobe analysis determined that the three sputtered libraries spanned a composition range of $0 < x < 0.55$ in Fe_xZn_{1-x}. Multiple libraries were sputtered to check for reproducibility and accommodate substrates used in characterization. Film compositions were calculated using the library closure technique outlined by Liao *et al.*,[70] which is illustrated in Figure 3.3. The variation of Zn and Fe moles per unit area along the library are defined by constant and linear in sputtering masks, respectively. This means moles of Zn will be constant along the sputtering track and moles of Fe will vary in a linear manner along the sputtering track. Figure 3.3(a) shows sputtered moles per unit area that best fit mass and composition data by a least squares method. Figure 3.3(b) shows film composition along the library. The calculated compositions (solid lines) in Figure 3.3(b) are obtained by converting sputtered moles of Fe and Zn to respective mole ratios. The calculated

Table 3.1 Summary of sputtered Fe_xZn_{1-x} libraries presented in this work.

Run ID	Power Supplied to Targets		Film Composition	Mass Loading (mg/cm^2)	Measured Thickness (μm)	Experiments
	Fe (W)	Zn (W)	Fe (at%)			
Spt055	78 (×2)	34	0.00 < x < 0.35	0.79 - 1.16	1.00 - 1.51	Electrochemistry
Spt065	90	35	0.00 < x < 0.44	0.91 - 1.31	1.28 - 1.62	Electrochemistry
Spt068	90 (×2)	72	0.02 < x < 0.24	1.93 - 3.22	2.36 - 3.94	Electrochemistry, Mössbauer
Spt126	35	70	x = 0.08	2.05 - 2.09	2.80*	*Ex-situ* XRD and *ex-situ* Mössbauer

* calculated thickness

compositions (solid line) from Figure 3.3(a) agree with compositions measured by electron microprobe (open and closed diamonds). Figure 3.3(c) shows that measured film mass per unit area (closed circles) also agrees with calculated mass (solid line) based on moles per unit area given in Figure 3.3(a). Library closure for the other two sputtering runs showed similar results.

Figure 3.4 shows XRD patterns measured at different radial distances on a Fe_xZn_{1-x} sputtered library for $0 < x < 0.35$. Figure 3.5 shows an expanded view of XRD patterns for $x = 0.04$ and $x = 0.07$. At low Fe concentration crystalline Zn peaks are present at 36.3°, 38.9°, and 43.2°. As Fe content increases, the sharp crystalline peaks are broadened and lose intensity and two new peaks appear in the XRD patterns at 41.1° and 59.9°. These peaks occur when film composition falls into the ζ ($FeZn_{13}$) region on the phase diagram,[71] however, the peaks are not characteristic of ζ $FeZn_{13}$ and, furthermore, do not correspond to any known Fe-Zn phase. Therefore it is attributed to a new Fe-Zn phase with an unknown structure. As Fe content is increased above 10 atom %, XRD measurements show the film is amorphous. To our knowledge, this is the first report of combinatorially sputtered amorphous Fe-Zn composite films.
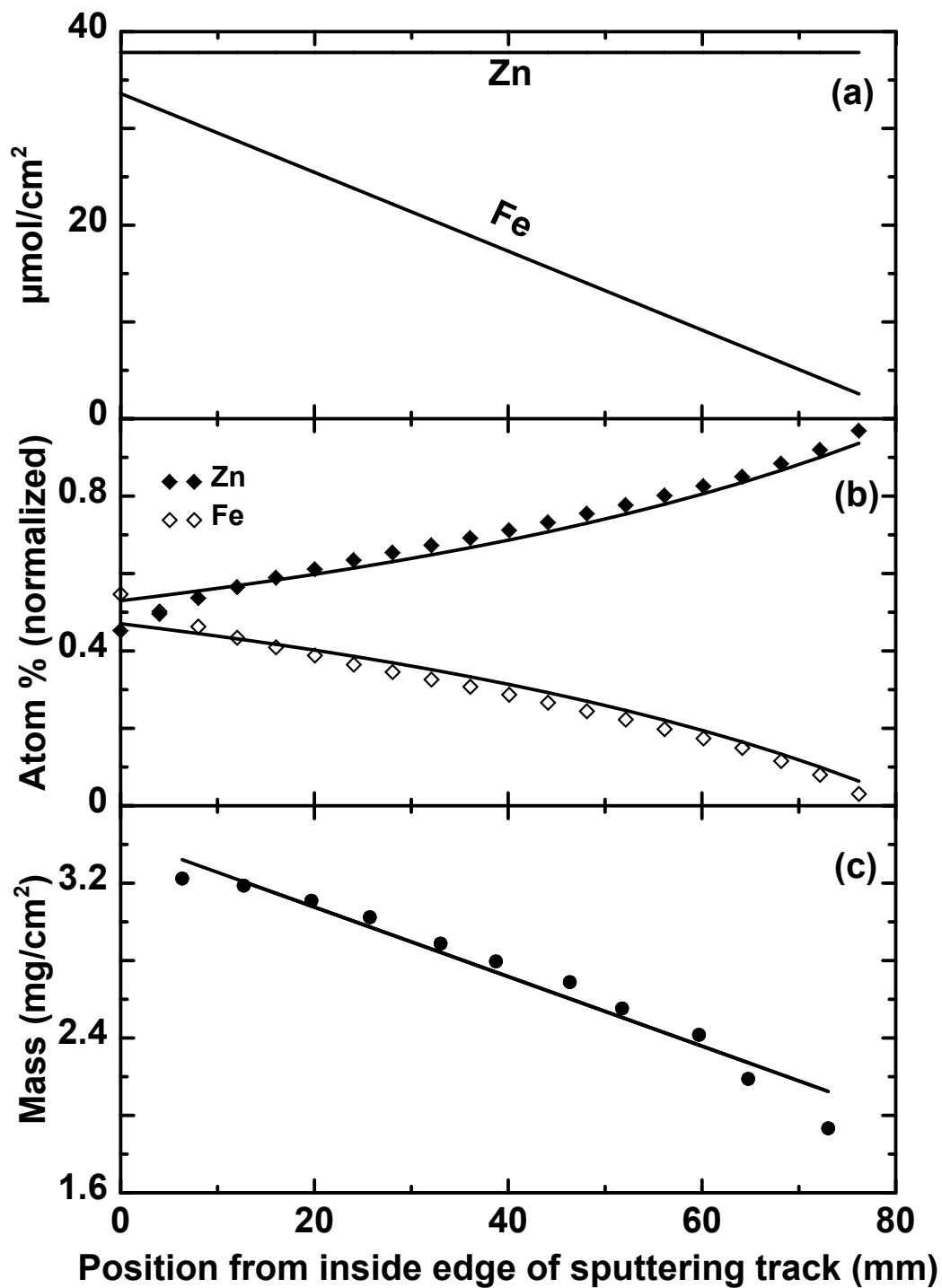
Figure 3.3 Library closure for Fe$_x$Zn$_{1-x}$ sputtering run with 0.03 < x < 0.55. (a) Calculated Zn and Fe moles per unit area defined by constant and linear out masks, respectively. (b) Calculated composition (solid line) from (a) agrees with measured microprobe data (open and closed diamonds). (c) Measured mass per unit area of sputtered film on Cu weigh disks (closed circles) and calculated mass (solid line) from (a).
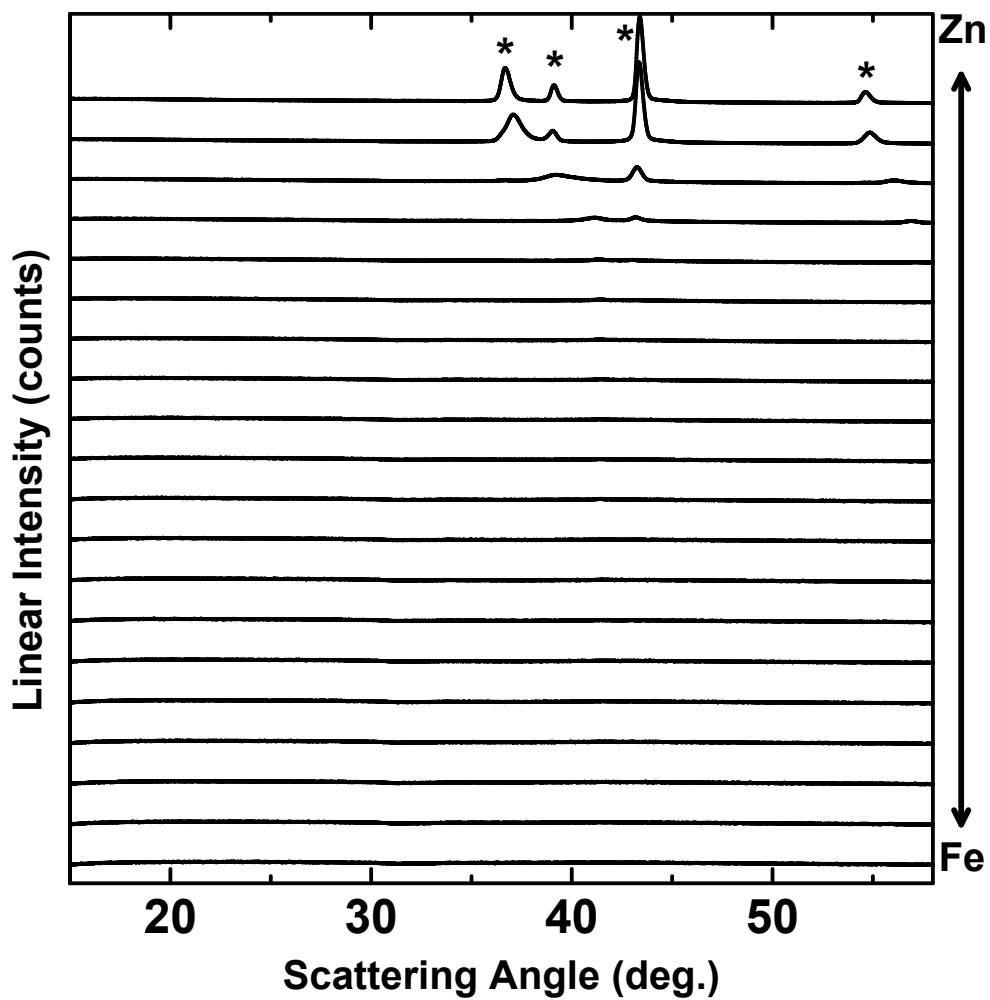
Figure 3.4 XRD patterns for Fe_xZn_{1-x} for $0 < x < 0.35$. The known Zn peak positions are indicated with a star (*).
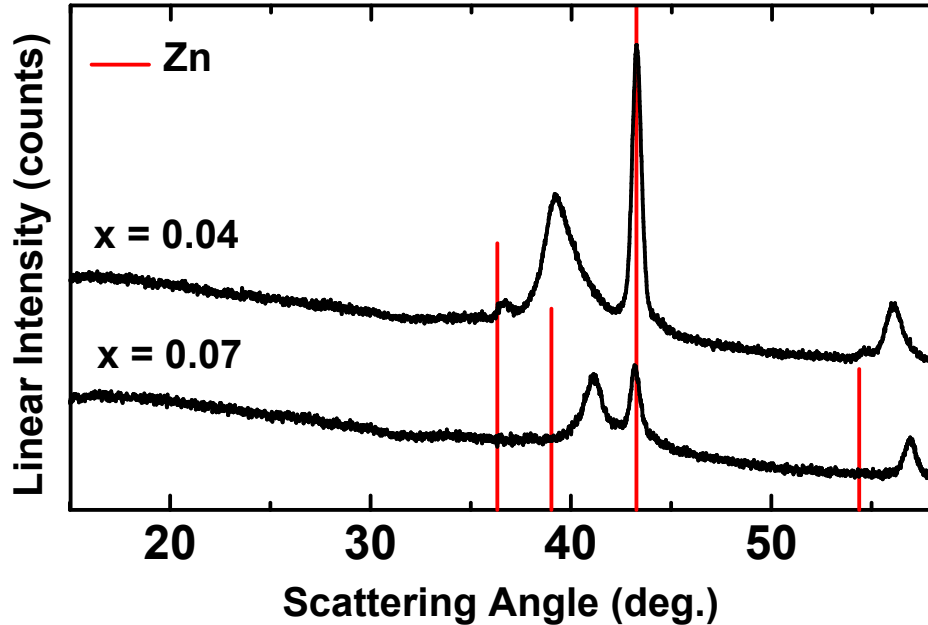
Figure 3.5 XRD patterns for Fe_xZn_{1-x} for x = 0.04 and x = 0.07. The known Zn peak positions and intensities are indicated with red lines.

3.3 Electrochemical Cycling

The lithiation of Fe-Zn alloys is expected to proceed via a displacement reaction

$$(1 - x)\text{Li} + \text{Fe}_x\text{Zn}_{1-x} \rightarrow (1 - x)\text{LiZn} + x\text{Fe}. \qquad (3.3)$$
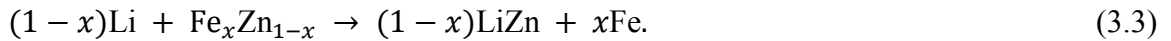
It is assumed that the free energy of formation is approximately equal to the heat of formation so the macroscopic atom model of de Boer *et al*. can be used.[72] The heats of formation of Fe_xZn_{1-x} and (1-x) moles of LiZn calculated with the macroscopic atom model are shown in Figure 3.6. A value of ΔH = -15.1 kJ/mol, calculated using equilibrium potentials obtained by Wang *et al*.,[9] was used for the heat of formation of LiZn because the macroscopic atom model is better suited for alloys containing at least one transition metal. According to this model the displacement reaction (3.3) is favorable for Fe-Zn alloys with up to 50 atom % Fe. Based on these thermodynamic calculations, Fe_xZn_{1-x} negative electrodes should be active towards lithiation when Fe content is below

50 atom %. Since the Γ phase in the Fe-Zn system is the richest Fe containing phase and can accommodate up to 31% Fe; the above calculation predicts that all equilibrium Fe-Zn phases should be active with respect to lithium, according to equation 3.3.
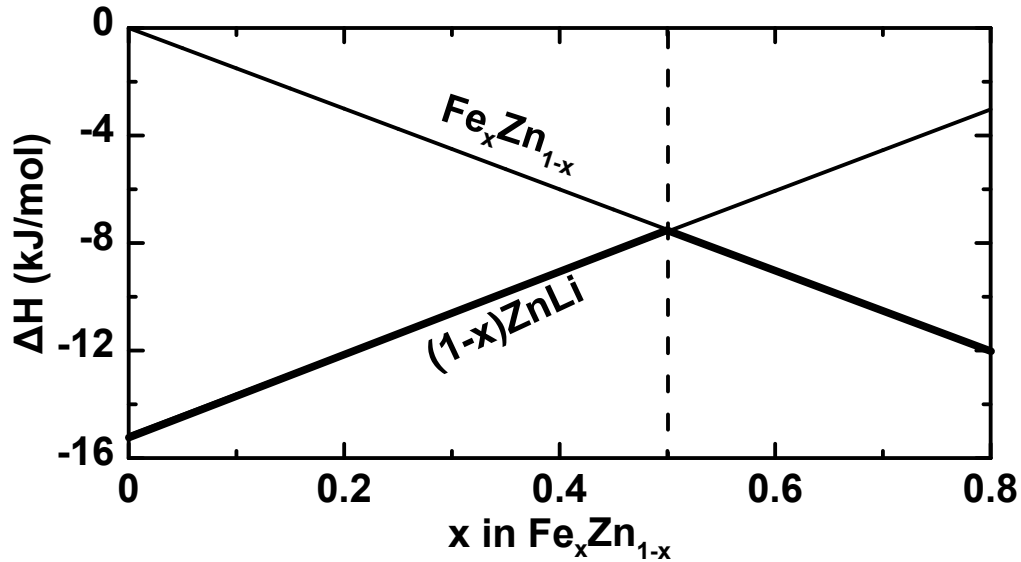
Figure 3.6 Heat of formation calculations of (1-x) moles of ZnLi as a function of Fe content. The region where formation of ZnLi is favorable and where Fe_xZn_{1-x} will not lithiate is separated by a dashed line.

Voltage curves for Fe_xZn_{1-x} films with x = 0.02, 0.05, 0.08 and 0.12 are shown in Figure 3.7. As will be shown below, in contrast to the above calculations, at Fe contents higher than x = 0.12 Fe_xZn_{1-x} is inactive. The voltage curve of the $Fe_{0.02}Zn_{0.98}$ film has several distinct plateaus, which correspond to the sequential lithiation of phases observed in the Li-Zn phase diagram. As the Fe content increases the plateaus in the voltage curves increase in slope and become less defined, which is consistent with the electrode being amorphous with increased Fe content. Figure 3.8 shows a differential capacity plot for selected cycles of $Fe_{0.12}Zn_{0.88}$. A differential capacity plot of pure Zn is characterized by five discharge peaks and eight charge peaks.[73] For $Fe_{0.12}Zn_{0.88}$ only about 3 poorly defined peaks are observed during charge and discharge. In addition,

42

during cycling differential capacity peaks become broader indicating the electrode becomes more amorphous.

There is severe slippage of all of the voltage curves in Figure 3.7. Voltage curve slippage is indicative of side reactions with electrolyte.[74] Coulombic efficiencies averaged over cycles 5-12 for cells with x < 0.12 are shown in Figure 3.9 and are all poor (< 0.92). With increasing Fe content (and reduced Zn content) the coulombic efficiencies increase in an approximately linear manner. This is consistent with the severe slippage and poor coulombic efficiency previously observed for Zn-rich C-Zn films,[57] and is further suggestive of Zn-alloys generally having poor coulombic efficiencies due to reactivity with electrolyte.
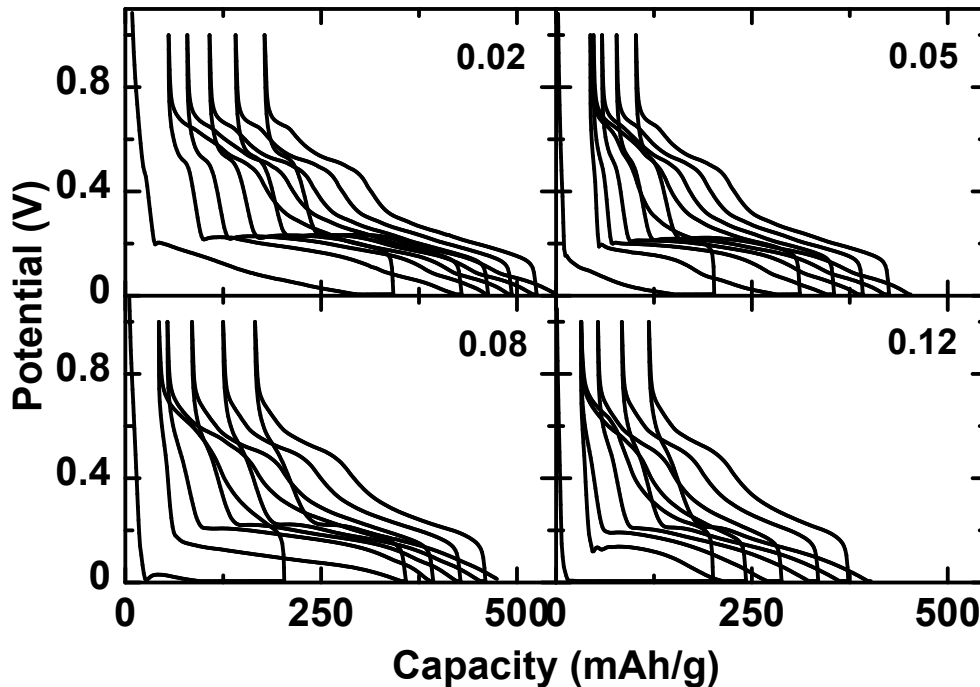
Figure 3.7 Voltage curves for selected low Fe content alloys. Fe content (x) is indicated in top right corner of plots.
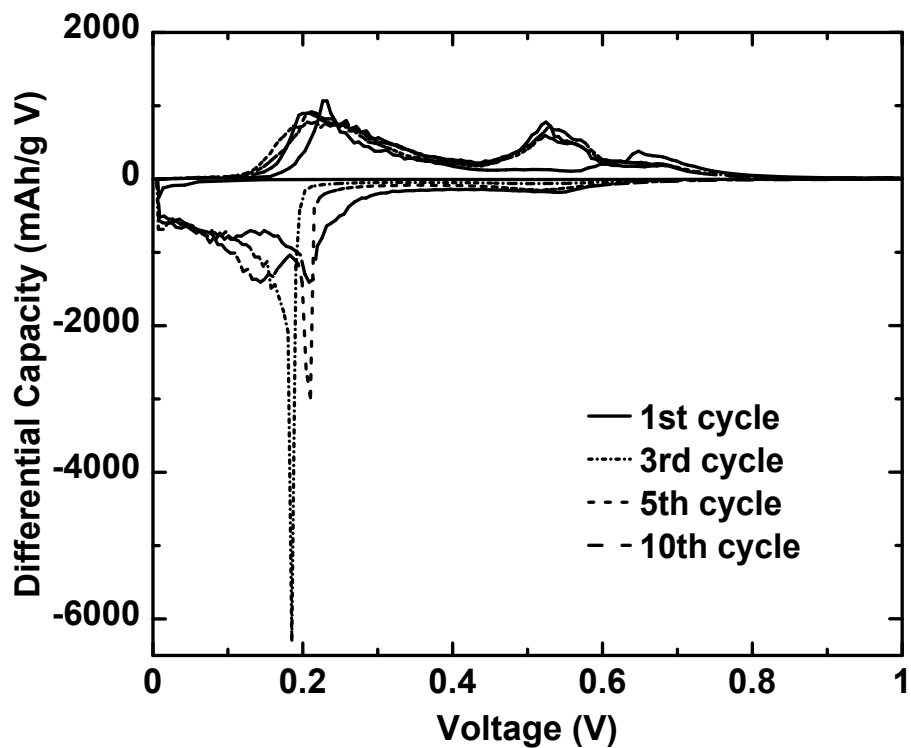
Figure 3.8 Differential capacity curves of various cycles for Fe_xZn_{1-x} with x = 0.12.
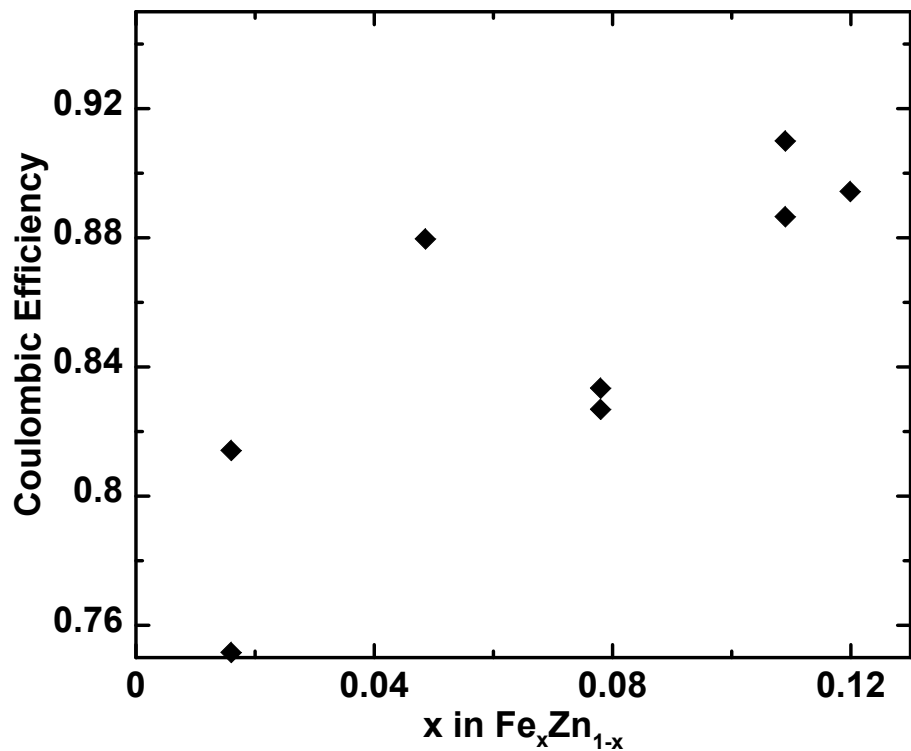
Figure 3.9 Average coulombic efficiency of cycles 5 through 12 for low Fe content electrodes
.

Figure 3.10 shows the cycling performance of the alloys shown in Figure 3.7. The

capacity initially increases over the first 4-7 cycles. Cracks and channels can form during

cycling due to large volume expansion giving rise to a higher surface area. The high

surface area improves Li diffusion, leading to increasing capacity over the initial cycles.

Similar findings were reported for the Al-Fe system.[59] After reaching a maximum

capacity at about cycle 5, all active cells had rapid capacity fade over subsequent cycles.

It has been found that this often occurs for thin film alloys. Composite coatings made

with these compositions are required to evaluate their cycling performance.
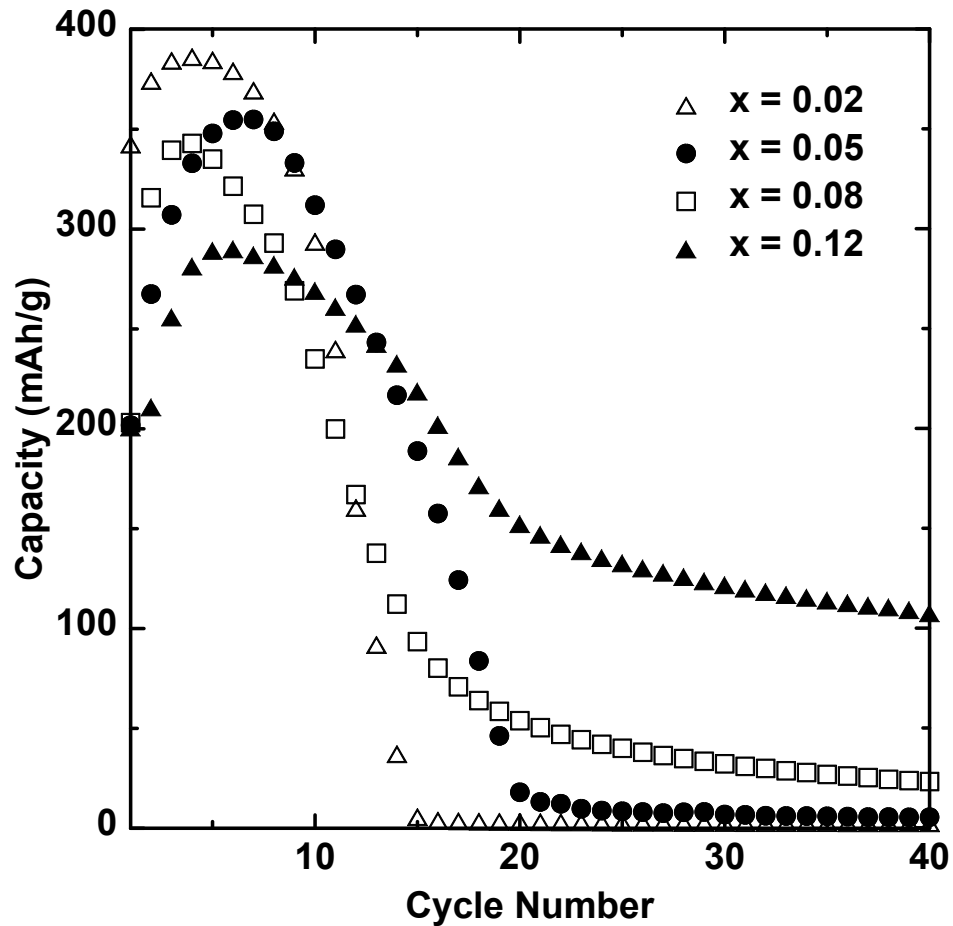
Figure 3.10 Discharge capacity versus cycle number for selected low Fe content alloys.

Figure 3.11 shows the fifth cycle specific capacity as a function of composition for Fe_xZn_{1-x} $(0 < x < 0.45)$. A capacity of 400 mAh/g was obtained for $x = 0.01$ which is just below the theoretical value of 405 mAh/g for this composition. As the Fe content is increased, the capacity drops linearly. A solid line in Figure 3.11 shows the predicted capacity according to equation 3.3, based on the thermodynamic calculations presented above. The presence of Fe decreases the capacity much more than expected. The decreased capacity fits well if it is assumed that for each Fe atom added, two Zn atoms become inactive (shown as a dashed line in Figure 3.11). Above $x = 0.12$ the Fe_xZn_{1-x} films are inactive. These results will be discussed in the context of Mössbauer and XRD measurements below.
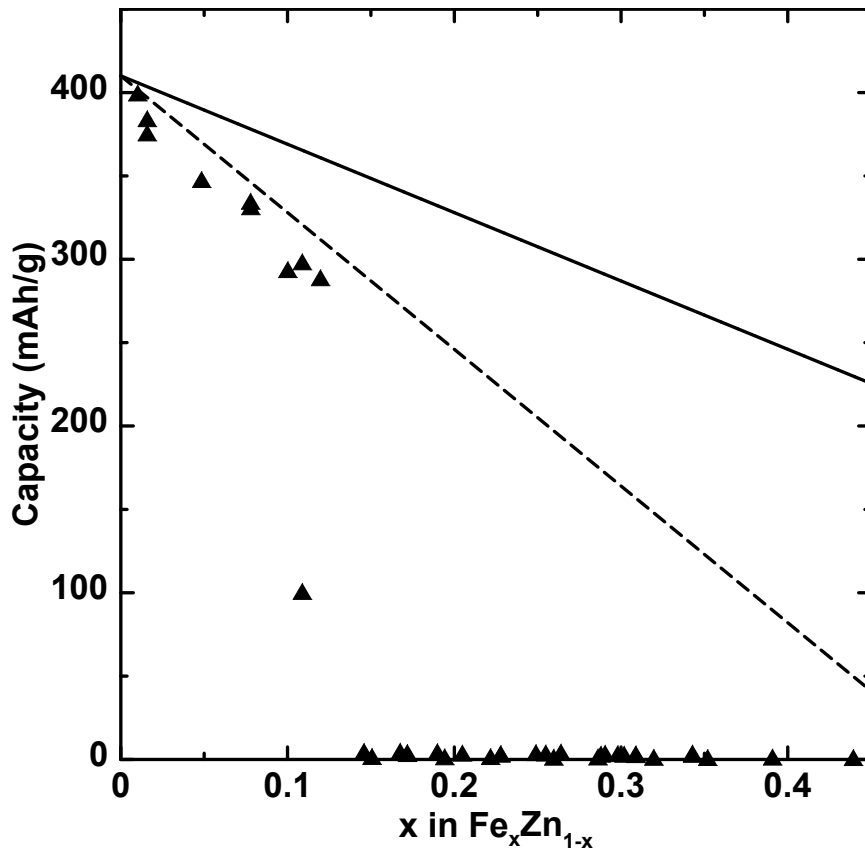
Figure 3.11 Fifth cycle discharge capacities for Fe_xZn_{1-x} for $0 < x < 0.55$. Theoretical capacity assuming all Zn is active is shown with a solid line. Theoretical capacity assuming each additional Fe atom inactivates two Zn atoms is shown with a dashed line.

3.4 Mössbauer Studies

Mössbauer experiments were performed on Fe_xZn_{1-x} thin films with $0.08 < x < 0.55$ using a ± 10 mm/s velocity range. Spectra were fit using a Voigt based function. Mössbauer spectra and fits for $x = 0.31, 0.43, 0.46$, and 0.55 are shown in Figure 3.12. Compositions are averaged over the sample region defined by the slit. The composition range for individual spectra is within ± 2 atom % Fe of the average. Parameters obtained from the fits in Figure 3.12 are given in Table 3.2. Spectra with 50 - 55 atom % Fe were fit to only magnetic hyperfine field distributions. Spectra with 40 - 46 atom % Fe were fit to combined hyperfine field and quadrupole doublet distributions and spectra with 35 atom% Fe and below were fit to quadrupole distributions only. Two magnetic sites were used to fit the spectra with magnetic components. The field distributions for the magnetic sites were between 19 T - 23 T for the high field sites and 4 T - 12 T for the low field sites. The mean center shift decreased with increasing Fe content for both the quadrupole and magnetic sites and quadrupole splitting increased with Fe content.

Table 3.2 Summary of hyperfine parameters obtained from analysis of spectra in Figure 3.12. The hyperfine field distribution (HFD) and quadrupole splitting distribution (QSD) sites correspond to magnetic and paramagnetic sites, respectively. CS and QS are the mean center shifts and quadrupole splittings, respectively. $<H>_{ave}$ is the average magnetic field of the HFD site. A (%) is the fraction of total area under the HFD or QSD site. Uncertainties in the CS,$<H>$, A, and QS values are ±0.005 mm/s, ±0.5 T, ±0.005 mm/s, and $\pm5\%$, respectively.

	HFD Site			**QSD Site**		
x	CS (mm/s)	$<H>_{ave}$ (T)	A (%)	CS (mm/s)	QS (mm/s)	A (%)
0.31	--	--	--	0.304	0.389	100
0.43	0.235	12.6	92	0.264	0.497	8
0.46	0.211	15.0	90	0.292	0.560	10
0.55	0.228	20.7	100	--	--	--
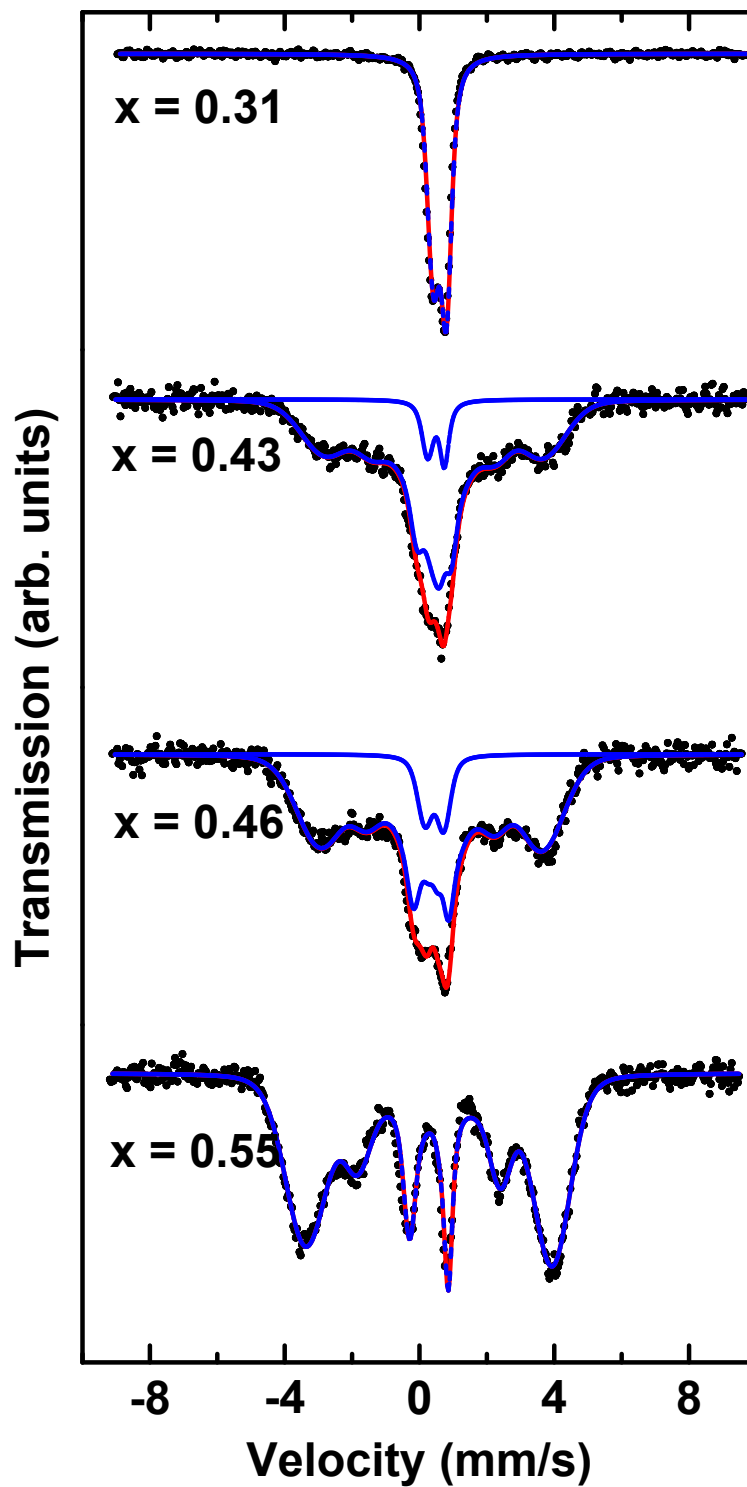
Figure 3.12 Room temperature ^{57}Fe Mössbauer effect spectra of Fe$_x$Zn$_{1-x}$ (x indicated in panels) at a ±10 mm/s velocity range.   The overall fits (solid red lines) and individual components (dashed blue lines) are superimposed on the experimental data (black dots).

Additional Mössbauer spectra were obtained for x = 0.08, 0.16, 0.21, and 0.26

with a ± 3 mm/s velocity range, allowing for a higher resolution of any small features in

the non-magnetic spectra. On this velocity scale it was necessary to use three quadrupole

sites to obtain reasonable fits with the data, indicating there are three distinct Fe sites in

the films. The fits were performed using Lorentzian doublets and are shown in Figure

3.13. The center shifts of each site decreased with increasing x and the quadrupole

splitting increased with x. Parameters obtained from the fits are given in Table 3.3.

The results show similar trends to those described by Hauet, Laggoun and Teillet

for radio frequency (r.f.) sputtered Fe-Zn films which were not amorphous.[75]   The use of

three quadrupole doublets to fit the Mössbauer spectra for the four Fe-Zn phases in the

Zn rich portion of the phase diagram has been previously reported in the literature for

non-sputtered samples.[68,75,76] The three doublet components are characteristic of three Fe

environments with site 1 corresponding to Fe with the greatest number of Fe neighbors

and site 3 corresponding to Fe atoms in the most dilute environment with the most Zn

neighbors.

Table 3.3 Summary of hyperfine parameters obtained from analysis of spectra in Figure 3.13. CS and QS are the center shifts and quadrupole splitting, respectively, of the three sites. A (%) is the fraction of total area under the peak of the doublet. Uncertainties in the CS, QS, and A values are ±0.005 mm/s, ±0.005 mm/s, and ±5%, respectively.

|	Site 1			Site 2			Site 3		
x	CS (mm/s)	QS (mm/s)	A (%)	CS (mm/s)	QS (mm/s)	A (%)	CS (mm/s)	QS (mm/s)	A (%)
0.08	0.25	0.12	17	0.431	0.000	39	0.604	0.04	44
0.16	0.156	0.09	21	0.352	0.07	33	0.563	0.091	45
0.21	0.126	0.225	14	0.274	0.125	36	0.545	0.101	50
0.26	0.091	0.190	21	0.209	0.187	30	0.529	0.109	48
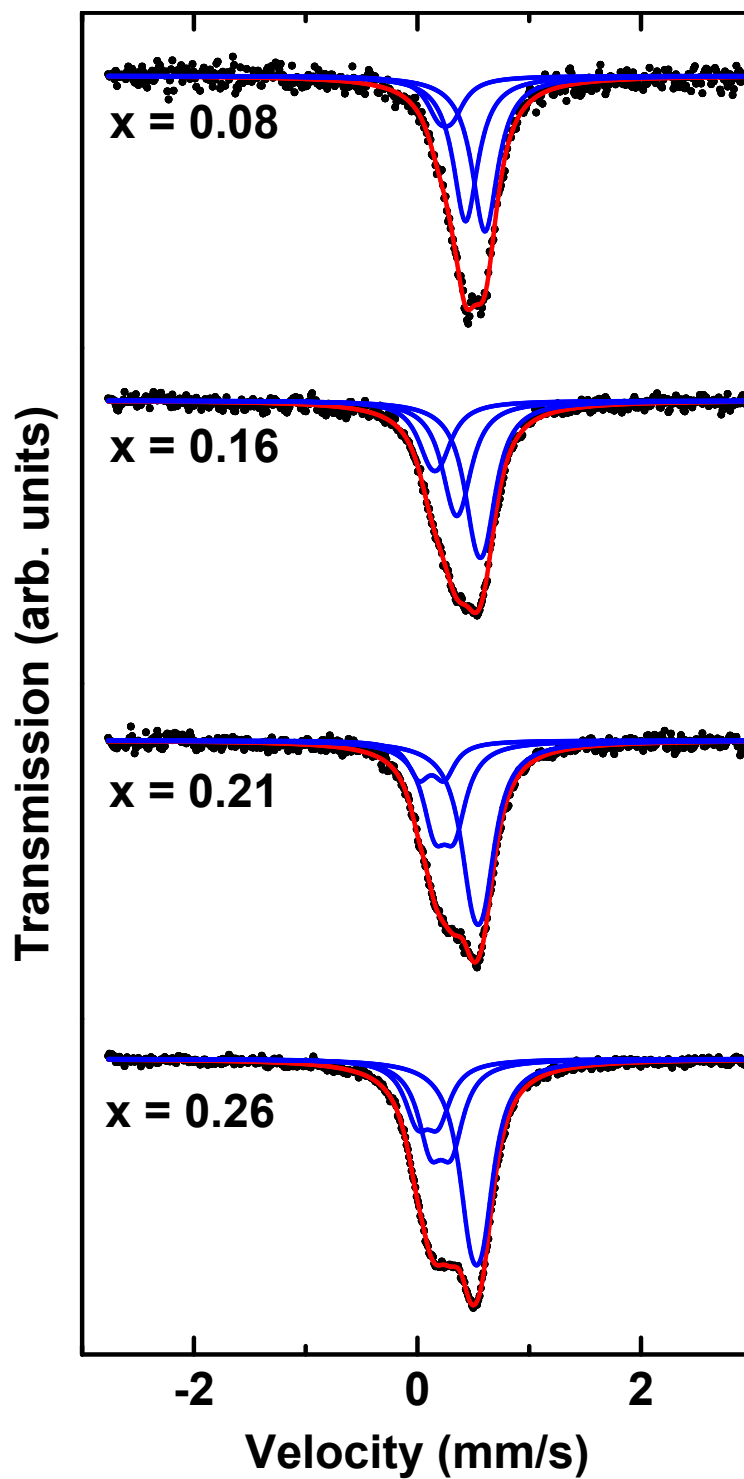
Figure 3.13 Room temperature ^{57}Fe Mössbauer effect spectra of Fe_xZn_{1-x} (x indicated in panels) at a ±3 mm/s velocity range.   The overall fits (solid red lines) and individual components (dashed blue lines) are superimposed on the experimental data (black dots).

For the $Fe_{0.08}Zn_{0.92}$ composition, center shifts of the three sites are similar to center shifts of various Fe-Zn phases reported in the literature. Site 1 has a center shift of 0.25 mm/s which is similar to reported average center shifts for the Γ (Fe_3Zn_{10}) and Γ_1 (Fe_5Zn_{21}) phases.[68,76] Site 2 has a center shift of 0.431 mm/s which is similar to reported average center shift values for the δ ($FeZn_{10}$) phase.[68,76] The center shift of site 3 (0.604 mm/s) does not correspond to center shifts of any known Fe-Zn phases, but has been used in fits of Mössbauer spectra r.f. sputtered Fe-Zn alloys by other groups.[75] If the data shown in Figure 3.14 are extrapolated, a center shift of 0.604 mm/s corresponds to 1.75 atom % Fe in Zn. As Fe concentration in the films is increased above x = 0.08 the center shifts of each site decrease as expected due to the addition of Fe neighbors. It is important to note, that although these Fe environments are similar to those found in bulk Fe-Zn phases, the Fe in these environments may be present in isolated clusters. Furthermore, as the Fe content is increased, such clusters may share Zn-atoms.

The simple semi-empirical model of Miedema and van der Woude can be used to interpret center shifts in metallic alloys.[77] The model proposed considers three contributions to the center shift in Fe-X alloys: (1) electronic charge transfer between atoms proportional to the difference in work functions of the elements, (2) s $\rightarrow$ d electron transfer which tends to make electron densities between neighboring Wigner-Seitz cells continuous, and (3) a volume adjustment when the atomic volumes of the two elements differ. The center shift can be modeled as

$$\delta(x_s) = (1 - x_s)\delta_{max} + \Delta_{IS}^{vol},$$ (3.4)

where the surface concentration, x_s, is given by

$$x_s = \frac{x\, V_{Fe}^{\frac{2}{3}}}{x\, V_{Fe}^{\frac{2}{3}} + (1-x) V_{Zn}^{\frac{2}{3}}}, \tag{3.5}$$

where V_{Fe} and V_{Zn} are the molar volumes of Fe and Zn, respectively, and x is the atomic percent Fe in the alloy. The maximum center shift, δ_{max}, is the center shift of an Fe atom completely surrounded by Zn neighbors in the alloy. In the Miedema and van der Woude model this is

$$\delta_{max} = P'(\varphi_{Fe} - \varphi_{Zn}) + Q'(n_{WS}^{Fe} - n_{WS}^{Zn}), \tag{3.6}$$

where φ is the work function and n_{ws} is the electron density of the Wigner-Seitz cell for a given element. P' and Q' are determined as best-fit parameters to experimental data.

Values of P' and Q' as given by van der Kraan and Buschow were converted to the form used by Hoving *et al.* in equation 3.6 to give 0.75 mm/s·V and 0.297 mm/s·d.u., respectively.[78,79] Work functions and Wigner-Seitz densities used in this work and are given in Table 3.4.[77,80]

Calculations from equations 3.4 through 3.6 and the experimental center shifts for the Fe$_x$Zn$_{1-x}$ compositions in this work are superimposed in Figure 3.14. The experimental center shifts are similar in magnitude to those predicted by the model presented by Miedema and van der Woude, but show a stronger dependence on Fe concentration. The center shift for dilute Fe in Zn is reported to be 0.500 mm/s by Ingalls *et al.* which agrees well with the 0.494 mm/s calculated in the Miedema and van der Woude model.[50]

Table 3.4 Parameters used in calculations from reference 77, 80. One d.u. = 4.7×10^{22} electrons/cm^3.

	φ (V)	n$_{ws}$ (d.u.)	V (cm^3)
Fe	4.93	5.55	7.106
Zn	4.33	2.30	9.157
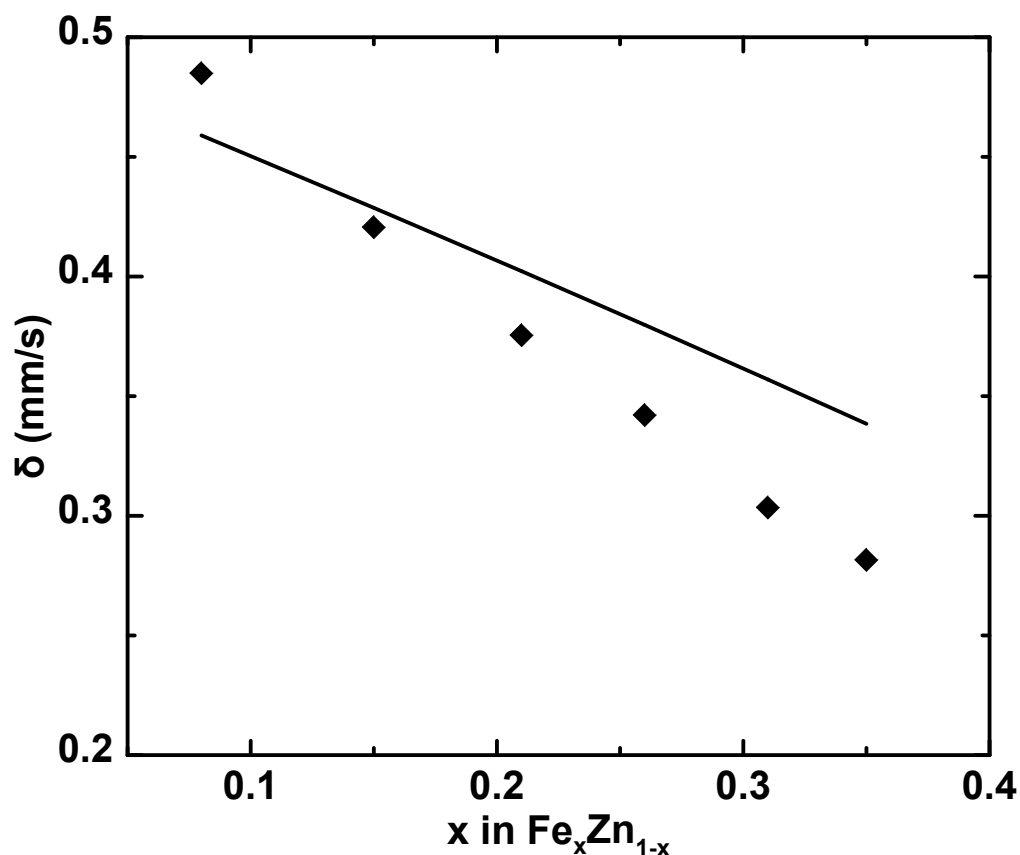
Figure 3.14 Center shifts for Fe_xZn_{1-x} Mössbauer spectra fit to quadrupole distributions only (♦) and predicted center shifts from the Miedema and van der Woude model (line). Ex-situ Mössbauer experiments were performed on cycled $Fe_{0.08}Zn_{0.92}$ electrodes.

The points on the voltage curve and respective Mössbauer spectra and fits are shown in

Figure 3.15. All spectra were measured at a 3 mm/s velocity scale and fit to four

Lorentzian singlet sites with distinct center shifts. The fitting parameters of sites 1 - 3 in

the cycled electrodes correspond closely to sites 1 - 3, respectively, that were used to fit

the as-prepared $Fe_{0.08}Zn_{0.92}$ film. A fourth site with near zero center shift was required to

provide reasonable fits for the cycled electrode spectra. This site has a near zero center

shift which is characteristic of an Fe precipitate. Slightly negative center shift values and

lack of quadrupole splitting have been observed for γ-Fe.[81,82] Superparamagnetic α-Fe has

a center shift of 0 mm/s and can look similar to γ-Fe. However, Mao, Dunlap, and Dahn

reported that superparamagnetic α-Fe precipitates were not found to be pure and had more positive center shifts and measureable quadrupole splittings.[83] Therefore, site 4 may be representative of γ- or α-Fe; however, the negative center shifts and consistent lack of quadrupole splitting in the spectra is suggestive of γ-Fe. Parameters used for the fits are given in Table 3.5.

The relative areas of Sites 2 and 4 increase significantly at the end of discharge (Figure 3.15 E). Simultaneously, there is a decrease in the relative area of Site 3. This suggests that as the electrode is lithiated and LiZn is formed, Fe is displaced from the Site 3 environment into the Site 2 ($FeZn_{10}$) and Site 4 (isolated Fe) environments. Site 3, comprising the most Zn rich phase, appears to be the only Fe-Zn phase present in the electrode that is active towards Li. In addition, the displacement reaction does not appear to be totally reversible as isolated Fe is present in the electrode after the first charge. Displaced Fe may be forming isolated clusters in the electrode on cycling, resulting in areas of inactivity. During cycling, the formation of the inactive $FeZn_{10}$ phase due to displaced Fe may not be totally reversible.

Table 3.5 Summary of hyperfine parameters obtained from analysis of spectra in Figure 3.15. CS and A(%) are the center shifts and the fraction of total area under the peak of the singlet, respectively. Uncertainties in the CS and A values are ±0.005 mm/s and ±5%, respectively.

	Site 1		Site 2		Site 3		Site 4	
	CS (mm/s)	A (%)	CS (mm/s)	A (%)	CS (mm/s)	A (%)	CS (mm/s)	A (%)
A	0.231	26	0.374	21	0.649	39	-0.02	13
B	0.226	18	0.373	31	0.644	45	-0.02	6
C	0.272	23	0.377	24	0.629	45	-0.02	9
D	0.249	18	0.381	25	0.635	45	0	12
E	0.19	16	0.431	47	0.635	10	0.02	27
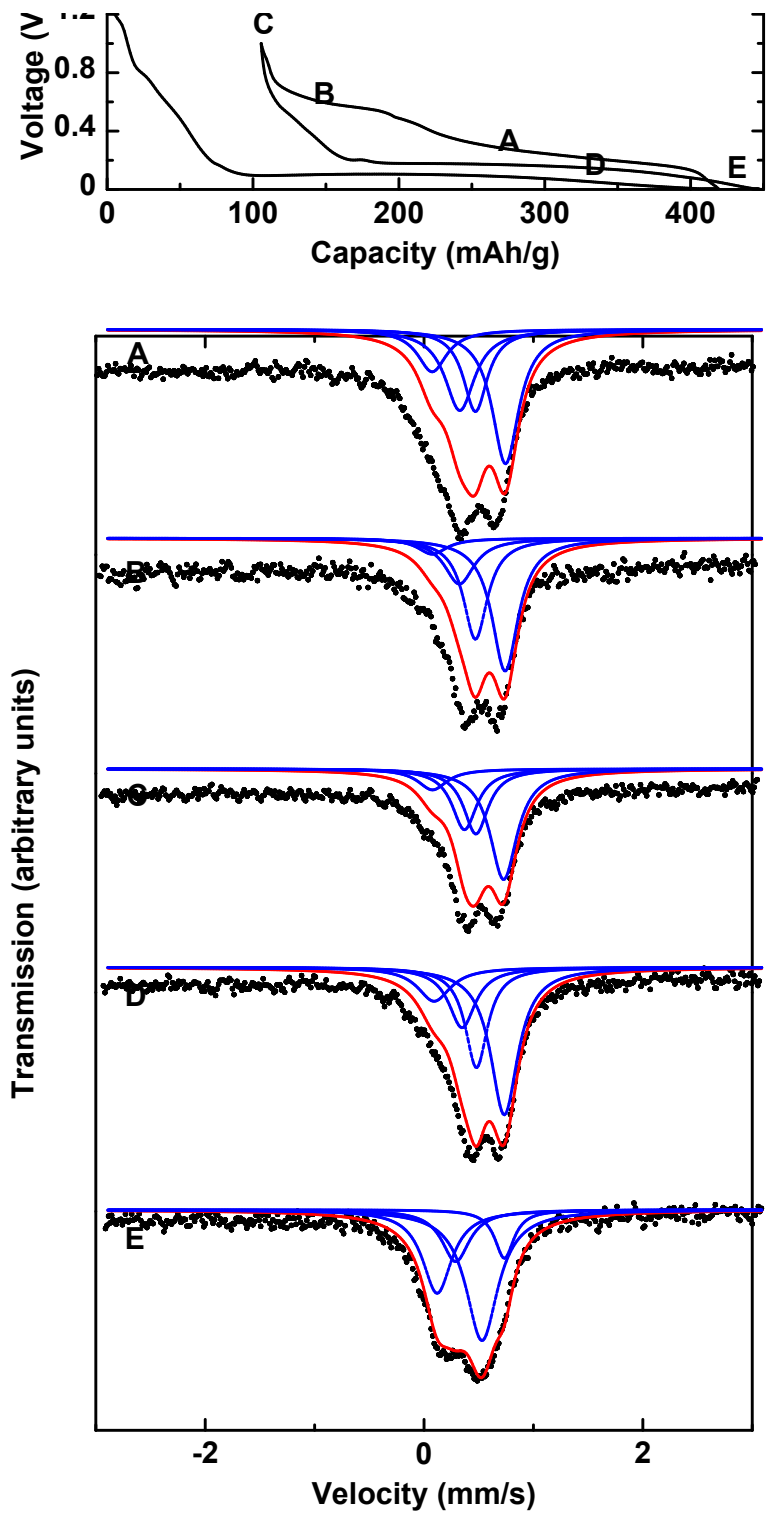
Figure 3.15 Voltage curve of $Fe_{0.08}Zn_{0.92}$ (top) and ex-situ Mössbauer spectra of cycled $Fe_{0.08}Zn_{0.92}$ electrode (bottom). Points of charge labeled A (0.275 V), B (0.60 V), C (1.0 V), D (0.15 V) and E (.005 V) correspond to spectra labeled A through E. The overall fits (solid red lines) and individual components (dashed blue lines) are imposed on the experimental data.

This may be a mechanism that could induce fade during cycling. Mössbauer measurements during subsequent cycles are required to confirm this.

Ex-situ XRD measurements were made of the same electrodes used for the above Mössbauer measurements. The XRD patterns collected at points C and E in Figure 3.15 are shown in Figure 3.16. When the electrode was fully delithiated (point C), the XRD pattern shows peaks from Γ-phase Fe-Zn. After subsequent full lithiation of the film (point E), the highest intensity peak from LiZn appears at 25.05°. The other higher angle peaks present in the XRD pattern of sample E fall between the peak positions for LiZn and Γ-phase Fe-Zn. A sample displacement could result in Li-Zn peaks being shifted to different angles; however, simple calculations show that peak shift due to sample displacement does not agree with the observed shift in peak positions. The relative intensities of the peaks also do not agree with the intensities for a LiZn XRD pattern. Thus, it is likely that the three higher angle peaks in the XRD pattern at full lithiation are from Γ-phase Fe-Zn. The offset in angle between the two XRD patterns is consistent with sample displacement, which can easily occur, depending on the sample size placed on the zero background wafer of the XRD holder. This is fully consistent with the above Mössbauer results, which show that there is Γ-phase Fe-Zn present and that it is not active toward lithiation. No other Fe-Zn phases were detected, but these may be present as amorphous phases (or in isolated clusters, as mentioned above) and be undetectable by XRD.

Using the results from Mössbauer and XRD measurements, the electrochemistry of the Fe-Zn films may be explained. Such films are composed of crystalline Zn, and Fe-
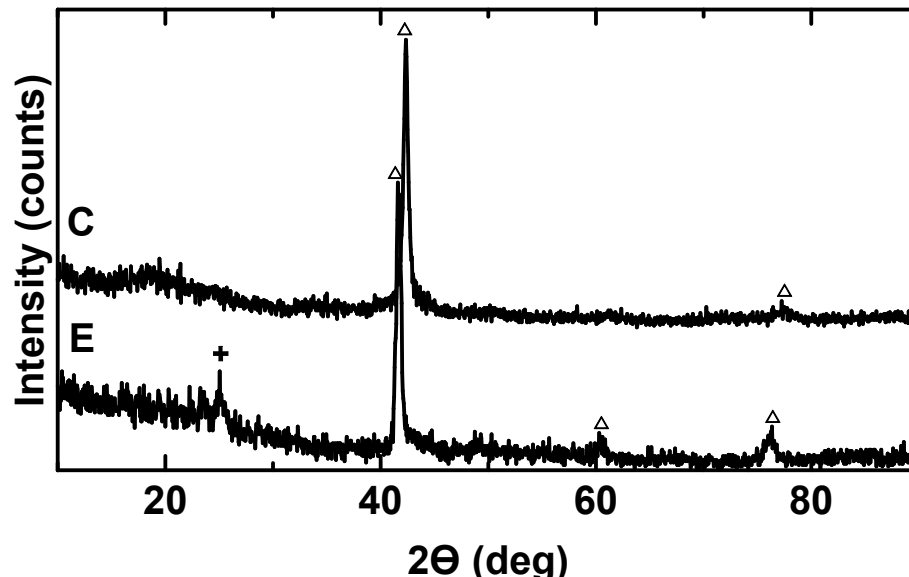
Figure 3.16 Ex-situ XRD patterns for points C and E of Figure 3.15. Γ-phase Fe-Zn peaks are indicated with a triangle (Δ). ZnLi peaks are indicated with a cross (+).

Zn alloys in environments that are similar to those in Γ (Fe_3Zn_{10}) and δ ($FeZn_{10}$) phases. All these phases are predicted to be active towards lithium from thermodynamic onsiderations, however the δ-phase is not active, presumably because of kinetic reasons. During lithiation of Fe_xZn_{1-x} films with x < 0.2, Fe is displaced from an unknown Zn rich Fe-Zn phase, forming LiZn, γ-Fe and the irreversible formation of inactive δ ($FeZn_{10}$). During delithiation the Zn rich phase is reformed.

As the Fe-content of the films is increased, 2 Zn are rendered inactive for every Fe added. At compositions with x > 0.2 the films no longer have Zn peaks in their XRD patterns, but are fully amorphous and inactive. It is likely that the Fe-Zn clusters have all joined together at such compositions, rendering all Zn atoms inactive, due to kinetic reasons. This is the same mechanism proposed for the inactivity of Al-Fe alloys with high Fe content.[56]

3.5 Conclusions for the Fe-Zn System

Thin film libraries of Fe-Zn were fabricated and characterized using combinatorial high throughput techniques. The capacity and electrochemical cycling ability of the electrodes was strongly dependent on composition. Compositions with less than 50 atom % Fe were predicted to be active by the macroscopic atom model of de Boer *et al.*.[72] Experimentally, only compositions with less than 12 atom % Fe were found to be active. These results are similar to those seen with Al-M systems where poor kinetics were believed to be responsible for inactivity of alloy compositions with less transition metal content.[59]

When Fe content is increased above 12 atom % samples are completely inactive. XRD patterns suggest that as an amorphous phase is introduced essentially all of the Zn atoms are being rendered inactive by surrounding Fe atoms. Mössbauer effect measurements suggest that Fe atoms are not spread uniformly throughout the material, but occur in three sites with different local Fe concentrations. Ex-situ Mössbauer measurements on cycled electrodes suggest that there are Fe-Zn phases present in the electrode which are inactive towards lithiation at room temperature. The ex-situ Mössbauer measurements also suggest that during the lithiation of Fe-Zn, Fe is displaced from the alloy, resulting in the formation of LiZn and inactive δ-phase Fe-Zn and isolated Fe.

Chapter 4 Fe-Si-Zn Ternary System

4.1 Introduction and Background

In this chapter alloys in the Fe-Si-Zn ternary system will be investigated as negative electrodes for Li-ion batteries. The ternary Fe-Si-Zn phase diagram is shown in Figure 4.1. The section labeled **A** in the figure is predicted to comprise three phases according to the phase diagram: an inactive $FeSi_2$ phase, an active pure Si phase and an active pure Zn phase. Fleischauer *et al.* performed electrochemical measurements on Fe_xSi_{1-x} thin films and found the films comprised an active Si phase and inactive FeSi phase.[38] Therefore, in this work the sputtered Fe-Si-Zn libraries are assumed to comprise an inactive FeSi phase, an active pure Si phase and an active pure Zn phase.

In studying this system it is hoped that the advantages of the Si-Fe system (lower volume expansion) and the Si-Zn system (suppression of $Li_{15}Si_4$ formation) can be combined to result in high performance anode materials.
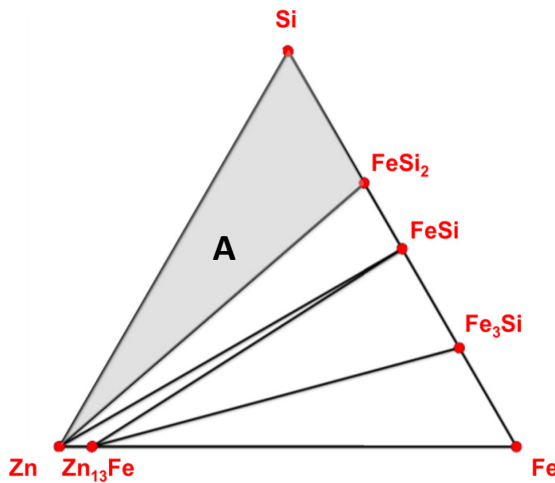
Figure 4.1 The Fe-Si-Zn ternary system as predicted by the Materials Project at 0 K.[61,62] The region labeled A comprises pure Si, pure Zn, and $FeSi_2$.

4.2 Film Characterization

Table 4.1 gives a summary of powers supplied to targets during sputtering and composition ranges obtained for each run. All libraries were sputtered for 4 hours. Figure 4.2 shows the range of Fe-Si-Zn compositions fabricated in a single sputtering run (Spt107). The labeled points correspond to plots in Figure 4.3 which show the XRD patterns for library Spt107. Figure 4.4 shows XRD patterns for the bottom row of Figure 4.3. The Zn concentration is approximately constant along this row (~29 at%) and the Fe concentration increases from 4 at% to 21 at%, while the Si concentration decreases from 67 to 50 at%.
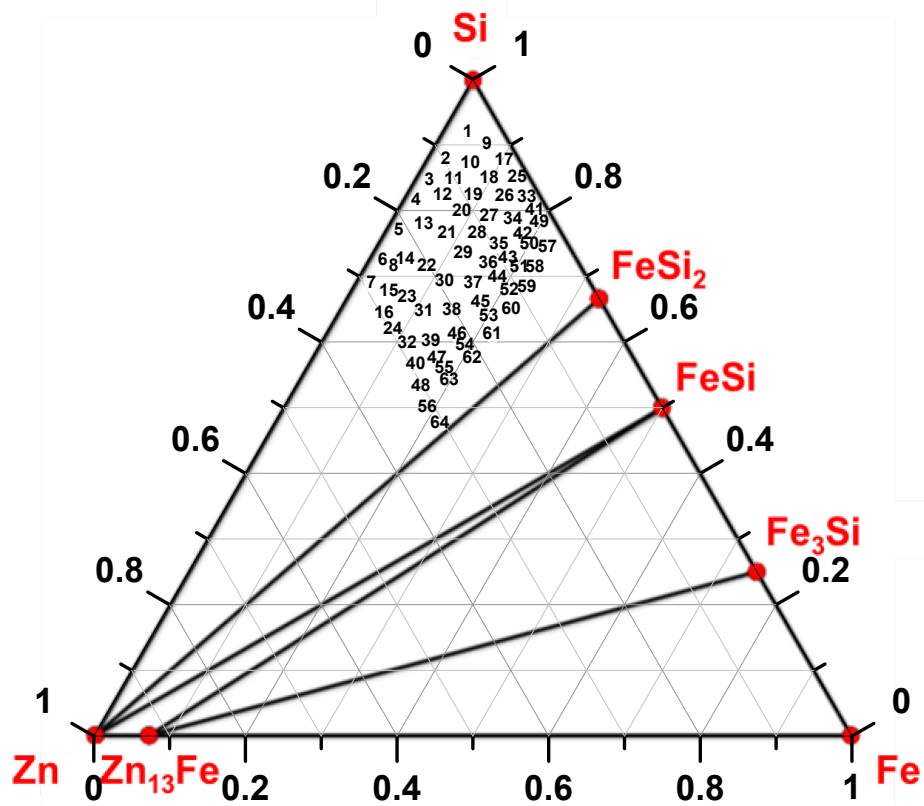
Figure 4.2 The Fe-Si-Zn ternary system as predicted by the Materials Project at 0 K.[61,62] The composition range of one sputtered library (Spt107) is superimposed on the diagram. Numbers correspond to XRD patterns shown in Figure 4.3

Table 4.1 Summary of sputtered libraries presented in this work.

	Power Supplied to Targets			Film Composition				
Run ID	Si (W)	Fe (W)	Zn (W)	Fe (at%)	Zn (at%)	Mass Loading (mg/cm^2)	Calculated Thickness (μm)	Electrochemistry Y/N
Spt074	130 (×2)	110	25	0.04 < x < 0.46	0.03 < y < 0.56	0.68 - 1.56	1.99 - 5.71	N
Spt094	130 (×2)	85	17	0.08 < x < 0.56	0.02 < y < 0.38	0.38 - 0.87	1.02 - 2.39	N
Spt101	130 (×2)	33	13	0.02 < x < 0.24	0.02 < y < 0.34	0.31 - 0.58	0.95 - 1.80	Y
Spt107	125 (×2)	32	13	0.02 < x < 0.23	0.02 < y < 0.31	0.25 - 0.46	0.80 - 1.50	Y
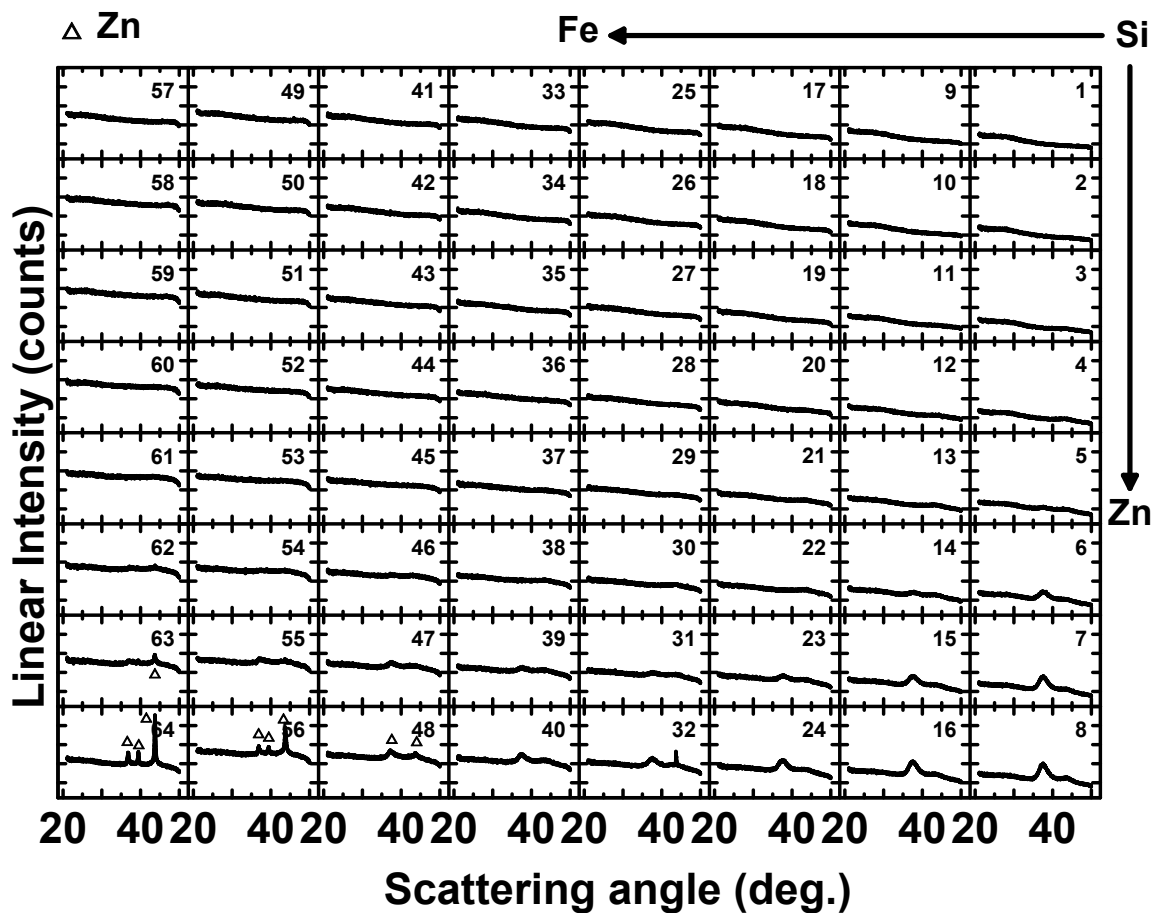
Figure 4.3 XRD patterns of library Spt107. Positions of Zn peaks are indicated with triangles (Δ). Numbers in top right corner of each plot correspond to compositions shown in Figure 4.2.
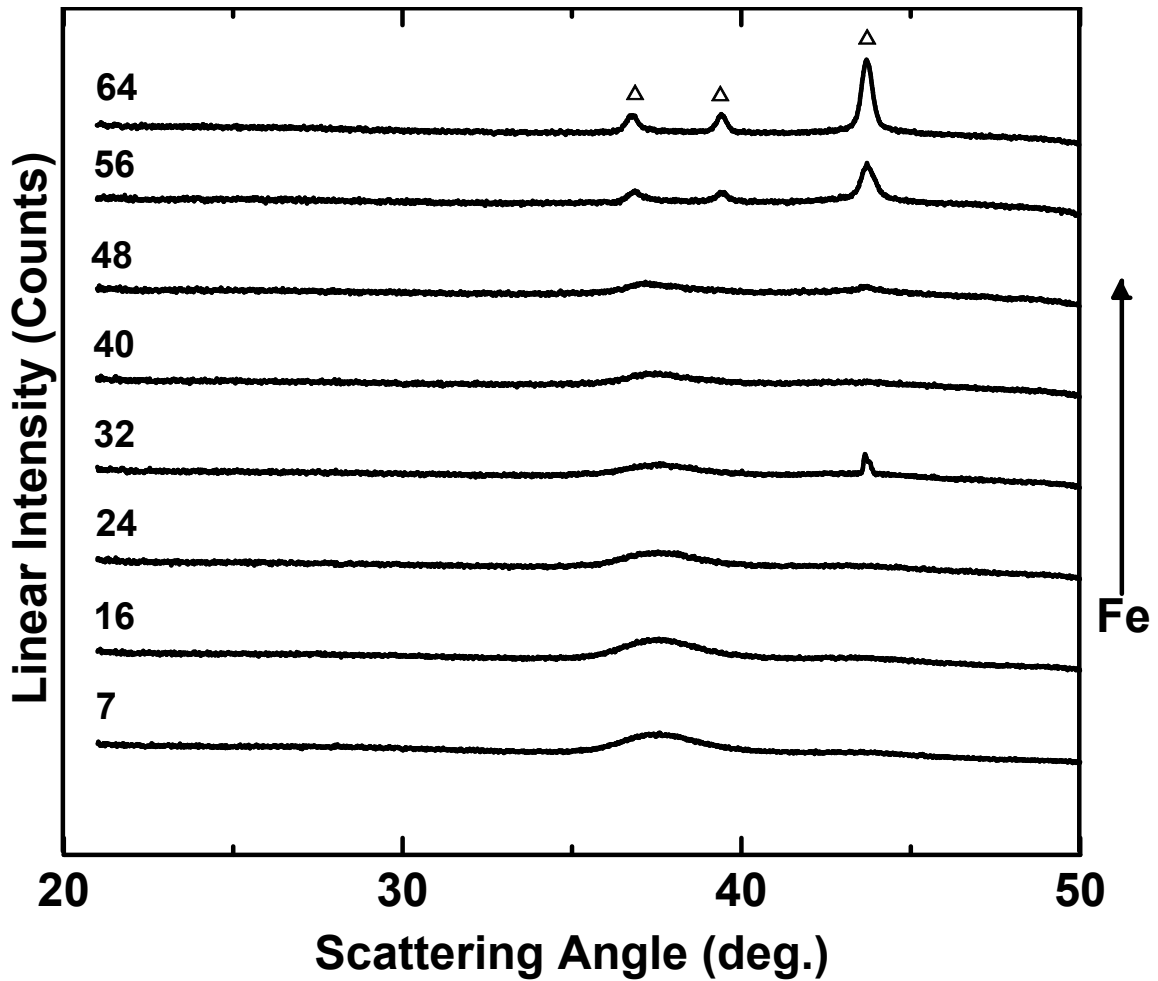
Figure 4.4 XRD patterns of compositions with constant Zn and varying Fe concentration from Figure 4.3 (approximately corresponding to compositions in the range of $Fe_y Si_{1-y-0.29} Zn_{0.29}$; $0 < y < 0.2$). Zn peaks are indicated with triangles (Δ). The arrow points in the direction of increasing Fe concentration.

It is clear from Figure 4.3 and Figure 4.4 that the Zn microstructure in the film is dependent not only on Zn concentration, but also on the Fe and Si concentration. It has been shown that Si-Zn thin films can be sputtered amorphously for compositions with less than 45 at% Zn,[35] which agrees well with the results found in this work for the lowest Fe concentrations. Si-Fe thin films can be sputtered amorphously for compositions with less than 72 at% Fe.[47] The range of compositions fabricated in this work did not extend above 50 at% Fe and all compositions along the Si-Fe portion of the phase diagram were

63

found to be amorphous, agreeing with previously reported results.[47] Along lines of

constant Zn composition, crystalline Zn formation becomes more favorable when both Fe

and Si are present. Crystalline Zn peaks begin to appear in the XRD patterns when the

Zn concentration is above 25 at% in compositions with a 4:1 Si:Fe ratio. Figure 4.5

shows a summary of the structures determined by XRD for all Fe-Si-Zn libraries

presented in this work. The entire shaded region in the figure indicates the total range of

compositions investigated while the darker shaded region corresponds to the range of Fe-

Si-Zn compositions that were sputtered amorphously.
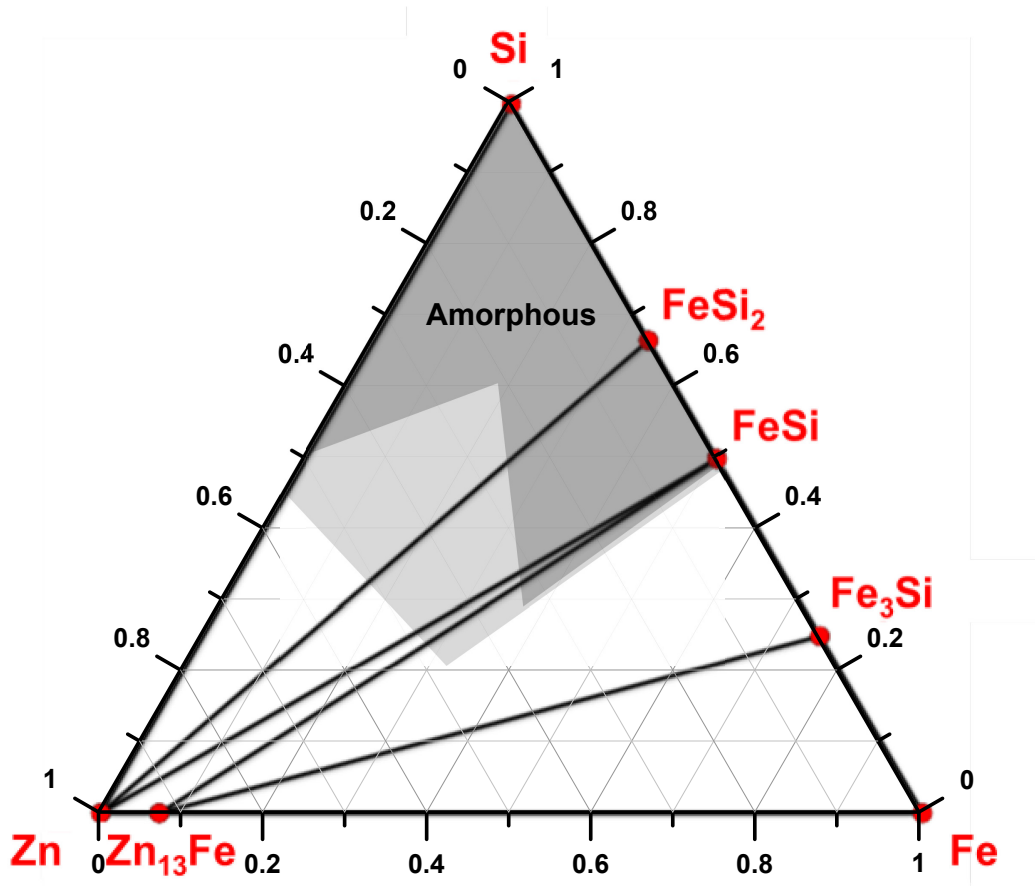
Figure 4.5 Range of compositions sputtered in this work superimposed on the Fe-Si-Zn ternary
system as predicted by the Materials Project at 0 K.[61,62] The entire shaded region represents
compositions fabricated in all four libraries. The dark shaded region represents those
compositions which can be sputtered amorphously.

4.3 Electrochemical Characterization

Figure 4.6 shows compositions on the Fe-Si-Zn Gibbs' Triangle for which electrochemical studies are presented. Electrodes were tested in half cells versus Li and cycled between 5 mV and 1.2 V, as mentioned in Section 2.5. The electrochemical results presented are for coin cells with electrodes from library Spt101. Electrochemical measurements were also conducted using coin cells with electrodes from library Spt107 and the results were consistent with those obtained from library Spt101. Figure 4.7 correlates the electrodes used in coin cells prepared from library Spt101 with the XRD patterns obtained from library Spt101.
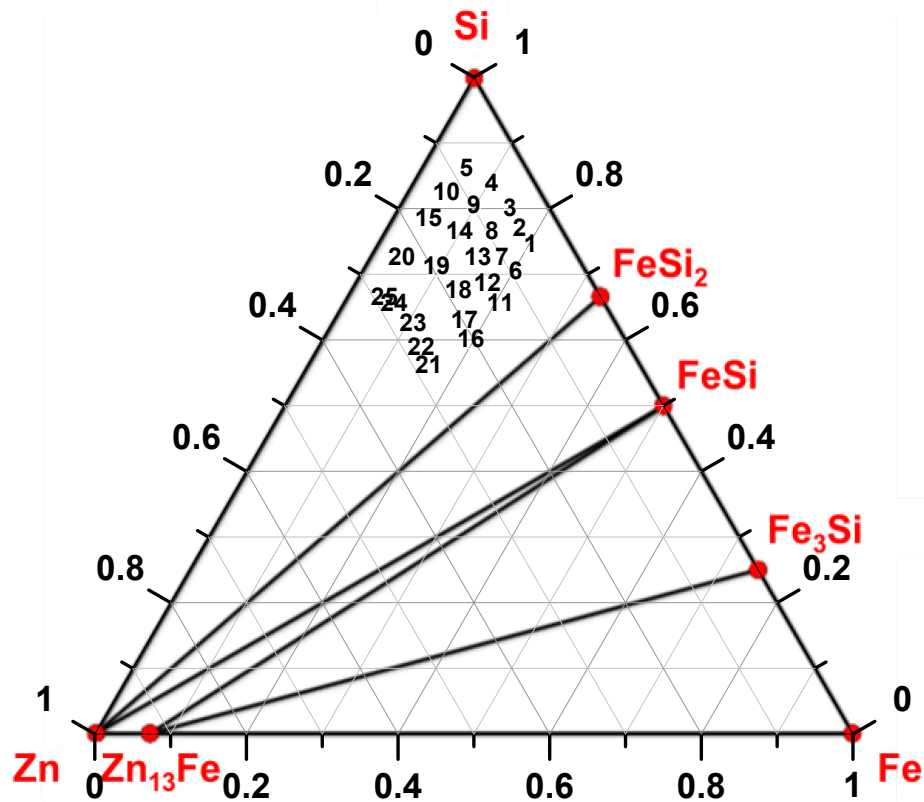
Figure 4.6 Compositions of coin cells prepared from library Spt101 superimposed on the Fe-Si-Zn ternary system as predicted by the Materials Project at 0 K.[61,62] Numbers correspond to plots in Figure 4.7, Figure 4.8, Figure 4.9, and Figure 4.14.
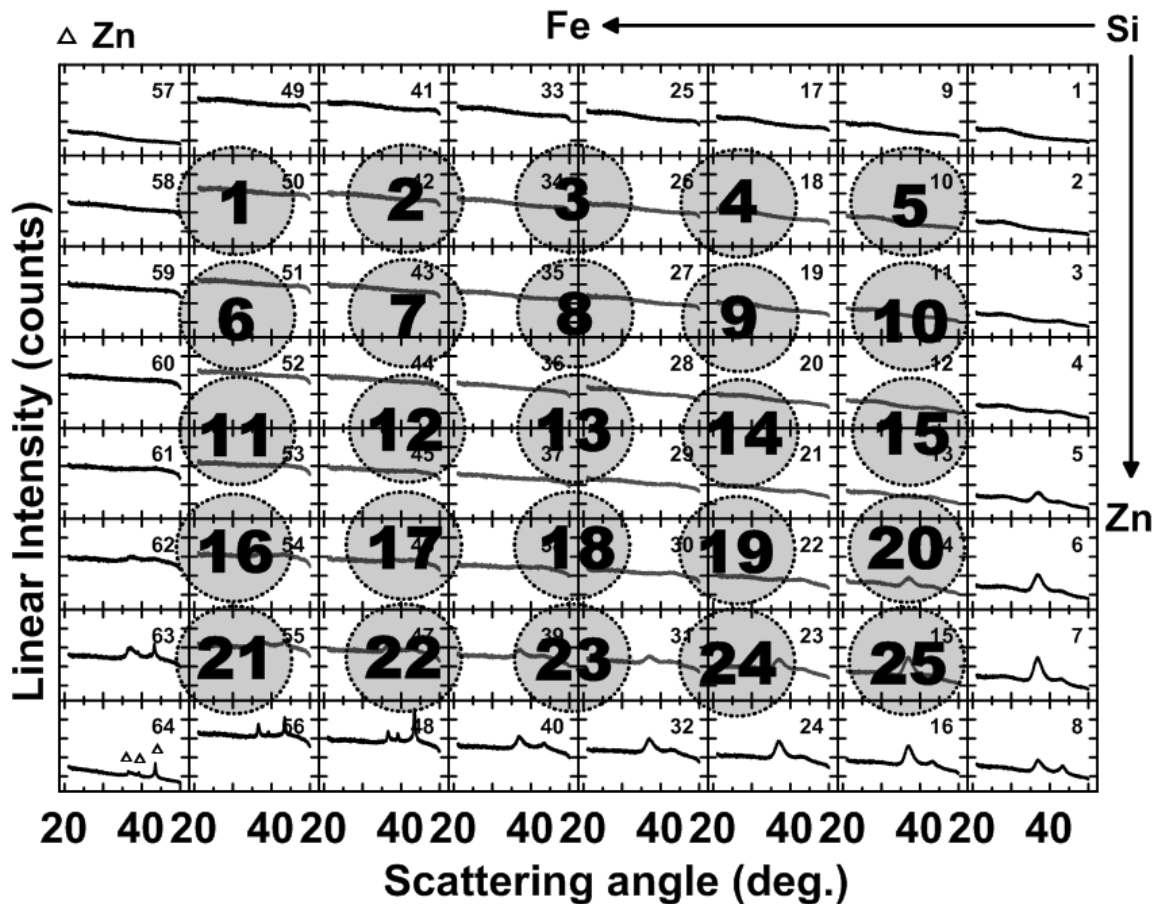
Figure 4.7 Position of coin cells from library Spt101 overlaid onto XRD patterns obtained from library Spt101. Zn peaks are indicated with triangles (Δ).
Voltage curves for the first 1.5 cycles for Spt101 are shown in Figure 4.8.

Voltage curves for all compositions show long sloping plateaus, characteristic of amorphous materials. Two distinct plateaus can be seen for voltage curves in the Si rich region (see plot 5 in Figure 4.8), characteristic of amorphous Si.[26] As Zn and Fe concentrations in the electrode increase, these plateaus become less defined. This can be seen more clearly in the differential capacity plots for cells from library Spt101, shown in Figure 4.9. All plots show broad peaks during charge for the first two cycles, indicating that the films remain amorphous during the first two cycles. The peaks become less defined as Fe and Zn concentrations in the film increase. All electrodes remain amorphous during cycling except those shown in panels 4 and 5 (electrodes with the

highest Si concentration), which show a sharp peak during charge for cycles 6-7 which is consistent with the formation of $Li_{15}Si_4$.[15] Crystallization of thin-film electrodes to form $Li_{15}Si_4$ during later cycles has been observed in Si-Ag thin-film electrodes.[36] It was suggested that the Ag which was initially dispersed throughout the electrode could be aggregating to form larger particles during cycling, leaving larger areas of Si that can more easily crystallize to form $Li_{15}Si_4$. A similar mechanism may be occurring in the Fe-Si-Zn electrodes in panels 4 and 5 of Figure 4.9, where Fe and Zn aggregate during cycling, leading to larger regions of Si and formation of $Li_{15}Si_4$.

Hatchard *et al.* concluded than a sufficient amount of Zn in Si-Zn thin film electrodes suppressed the formation of the $Li_{15}Si_4$ phase.[35] In the present work, both Fe and Zn appear to suppress $Li_{15}Si_4$ formation. The Zn and Fe concentrations required to suppress $Li_{15}Si_4$ formation are 13 at% and 15 at%, respectively. Only electrodes containing the lowest Zn and Fe concentrations showed evidence of $Li_{15}Si_4$ formation during cycling.

During the lithiation of Si-Zn thin films a ternary $Li_{2+x}SiZn$ phase is formed. During delithiation, Zn does not phase separate and the films become amorphous or nanocrystalline. This mechanism was thought to suppress Si phase aggregation during cycling and, as a result, it also suppress $Li_{15}Si_4$ formation.[35] It is possible that the FeSi inactive phase may also suppress Si aggregation in Si-Fe alloys, resulting in the suppression of $Li_{15}Si_4$ formation. However, additional mechanisms may be operating that suppress $Li_{15}Si_4$ formation in these films, as will be discussed below.
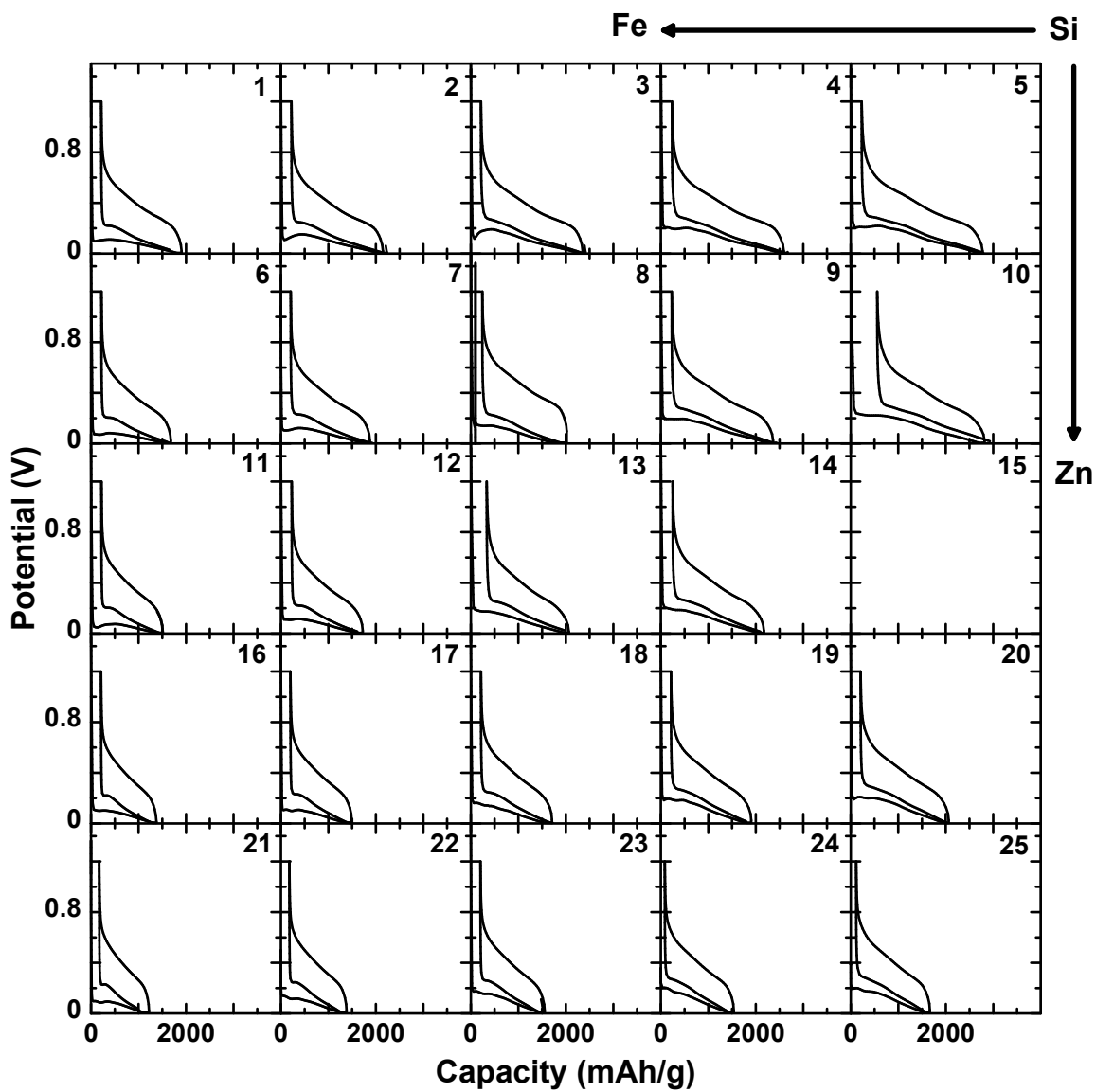
Figure 4.8 Voltage versus capacity cures for cells from library Spt101. Numbers in the top right corner correspond to numbers shown on the coin cells in Figure 4.6.
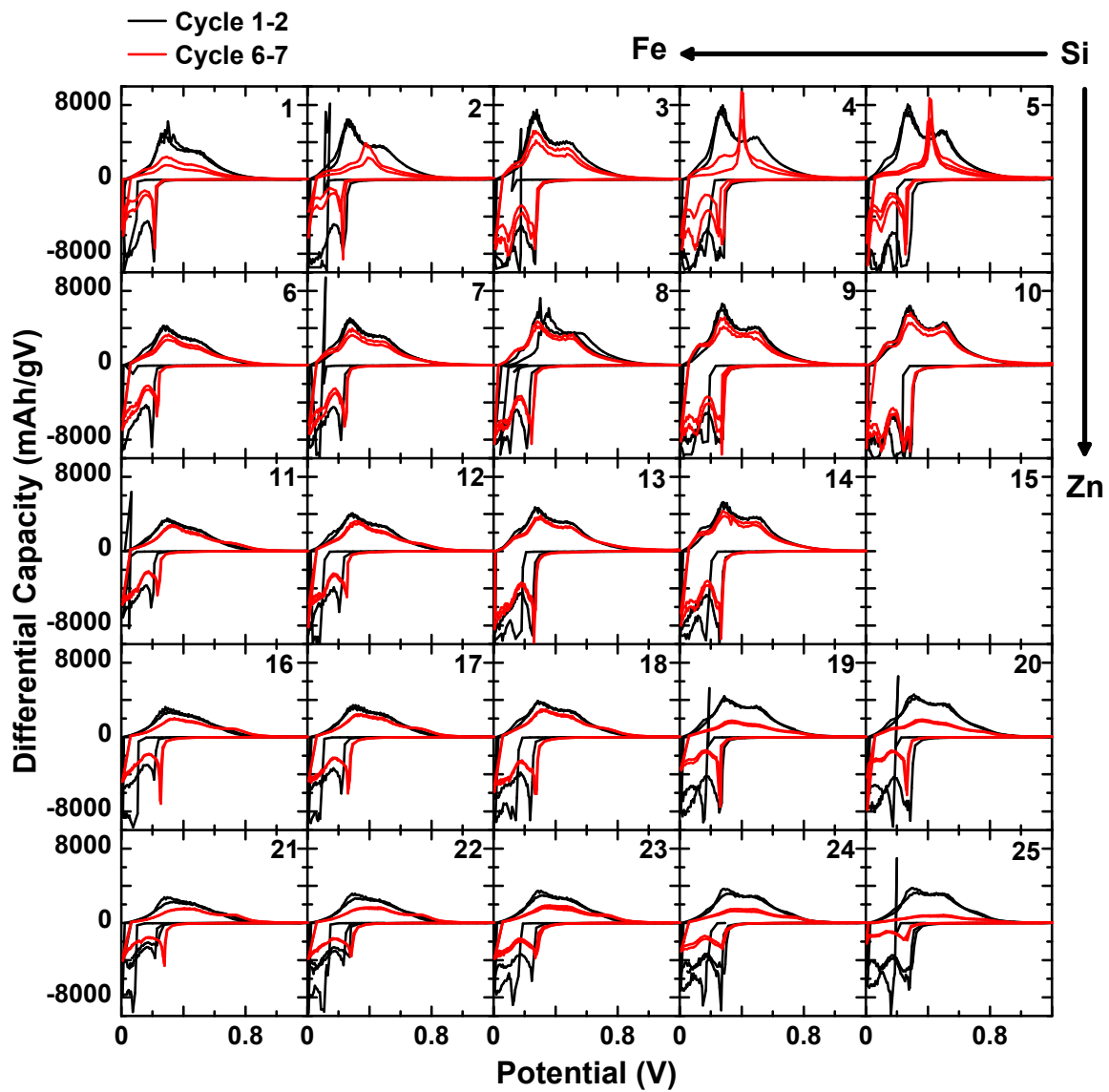
Figure 4.9 Differential capacity curves for cells prepared from library Spt101. The first two cycles are shown in black and the sixth and seventh cycles are shown in red.

Average discharge and charge voltages for all compositions are between 0.11 V - 0.17 V and 0.37 V - 0.42 V, respectively. Average charge and discharge voltages were calculated for the first charge and second discharge, respectively. The average discharge voltage decreases with increasing Fe concentration and the average charge voltage increases with increasing Zn concentration. Thus, hysteresis in the voltage curves increases as Fe and Zn concentrations are increased concurrently in the electrode. This is illustrated in Figure 4.10 which shows an overlay of three normalized voltage curves of the first charge and second discharge for the most Si rich ($Si_{0.86}Zn_{0.08}Fe_{0.06}$), Zn rich ($Si_{0.66}Zn_{0.29}Fe_{0.05}$), and Fe rich ($Si_{0.74}Zn_{0.06}Fe_{0.20}$) compositions in library Spt101.
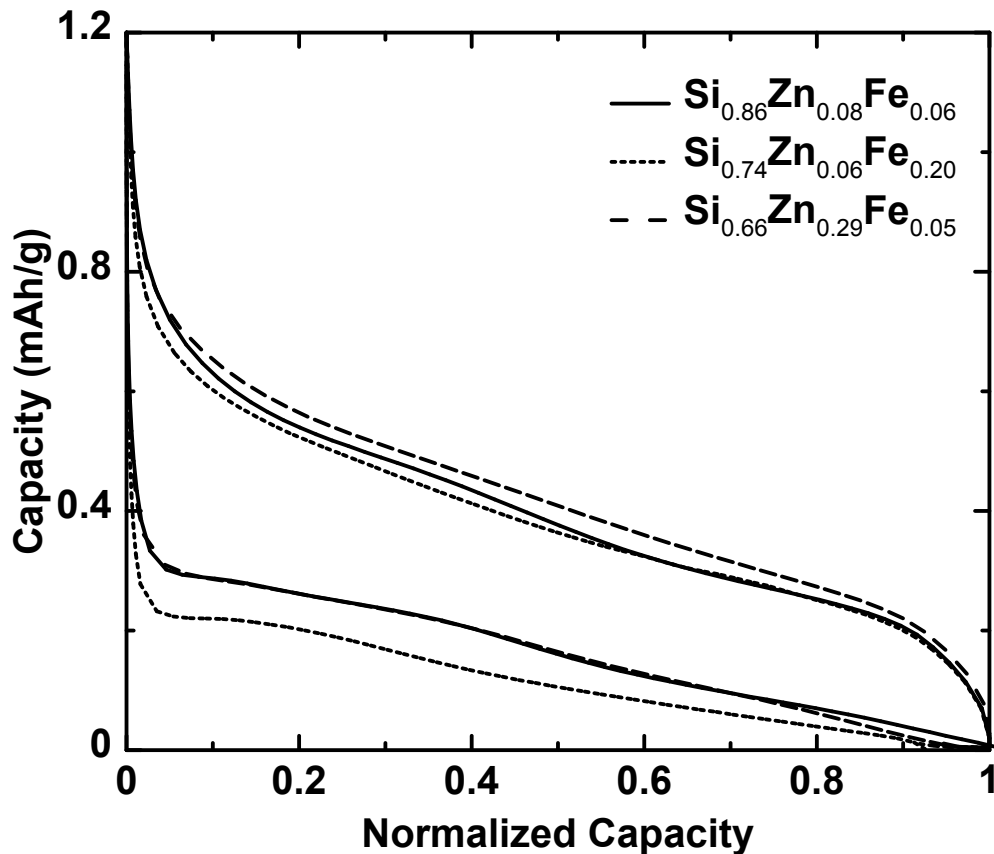
Figure 4.10 Overlay of voltage curves of the first charge and second discharge from panels 1, 5, and 25 in Figure 4.8. The capacity is normalized by first charge capacity.

For the most Fe rich composition the charge portion of the voltage curve is identical to the most Si rich composition, and the discharge portion of the curve is at a lower voltage. Although Fe depresses the voltage of the discharge voltage curve, the features in the discharge voltage curve remain unchanged. For the most Zn rich composition the discharge portion of the voltage curve is identical to that for the most Si rich composition, while the charge portion of the curve is at a higher voltage.

Variations in the average voltage can also be seen in the differential capacity plots shown in Figure 4.9. Fe concentration is increasing from right (panel 5) to left (panel 1) along the top row of Figure 4.9. Positions of the discharge peaks near 0.09 V and 0.26 V shift to lower voltage as Fe concentration is increased, decreasing the average discharge voltage. Zn concentration is increasing from top (panel 5) to bottom (panel 25) in the rightmost column of Figure 4.9. As Zn concentration is increased, a broad peak on charge is introduced at 0.74 V, increasing the average charge voltage. This high voltage peak has been previously observed in Si-Zn thin films.[35] A contour plot of hysteresis versus composition is overlaid on a portion of the Fe-Si-Zn Gibbs' Triangle in Figure 4.11.

The effect of the depression of the discharge voltage curve with increasing Fe content has not been previously reported, although it can be readily seen in the differential capacity plots shown in the study of all of the sputtered Si-M alloy systems (M = Fe, Mn, (Ni + Cr)) by Fleischauer et al.[38] The origin of this discharge voltage depression is not known. Whatever its cause, the depression in the voltage curve is as much as 0.75 V. Since $Li_{15}Si_4$ formation occurs below 50 mV in pure Si,[25] the voltage

depression caused by the addition of transition metals is likely the cause of the suppression of $Li_{15}Si_4$ formation in Si-M alloys.

The initial coulombic efficiency (ICE) of the Fe-Si-Zn alloys varied from 0.80 (cell 10) to 0.94 (cell 24). The ICE showed a linear dependence on Si concentration in the electrode and increased with increasing Si content. Absolute values of irreversible capacity in mAh/g were similar for all cells, but cells with higher Si concentration have higher total capacity which increases the ICE for these cells. ICE versus Si concentration is shown in Figure 4.12 for coin cells
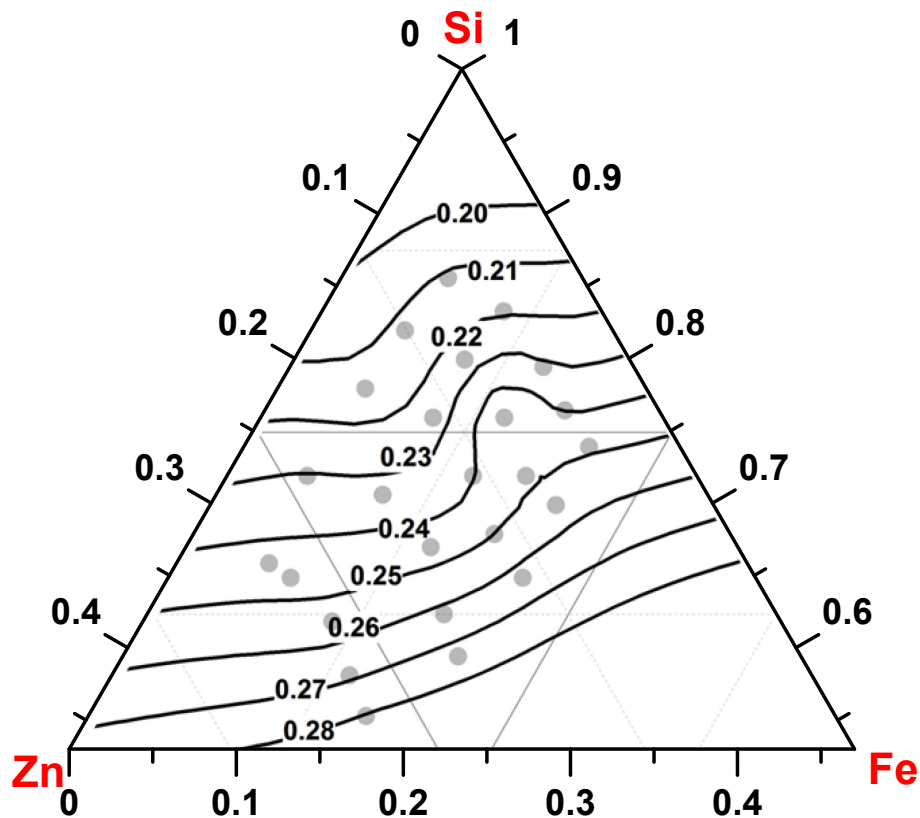
Figure 4.11 Contour plot of hysteresis of second cycle for cells in Figure 4.8. Hysteresis values in volts are indicated on contour lines. Cell compositions are shown in grey.
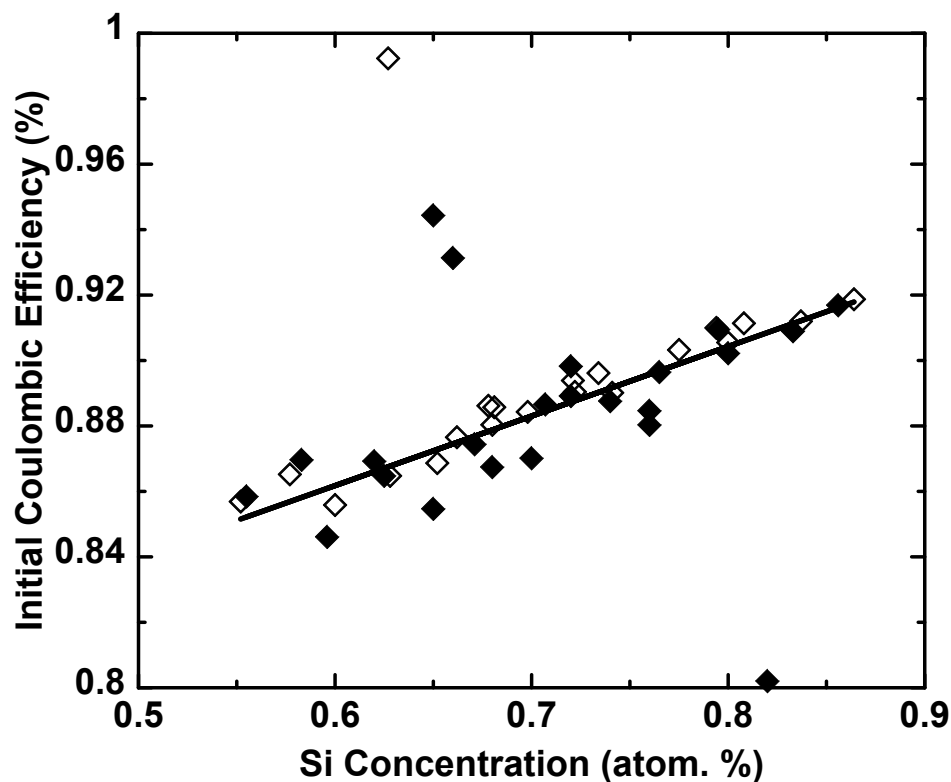
Figure 4.12 Initial coulombic efficiency as a function of Si concentration in the electrode for cells prepared from libraries Spt101 (closed diamonds) and Spt107 (open diamonds). A straight line of best fit by least squares is shown.

prepared from libraries Spt101 and Spt107. A line of best fit determined by least squares is shown. Anomalous points were not included in the fit.

Theoretical and observed capacity versus composition is overlaid on a portion of the Fe-Si-Zn Gibbs' triangle in Figure 4.13. Capacities of cells are predicted assuming all Fe is in an inactive FeSi 1:1 phase, the remaining Si alloys with 3.75 Li per Si, and all Zn present is active and alloys with 1 Li per Zn. Predicted and observed first charge capacities for cells from library Spt101 are shown in Figure 4.14. Predicted capacities agree well with the observed capacities, which is consistent with the proposed model that the film scomprise FeSi, active Si, and active Zn.
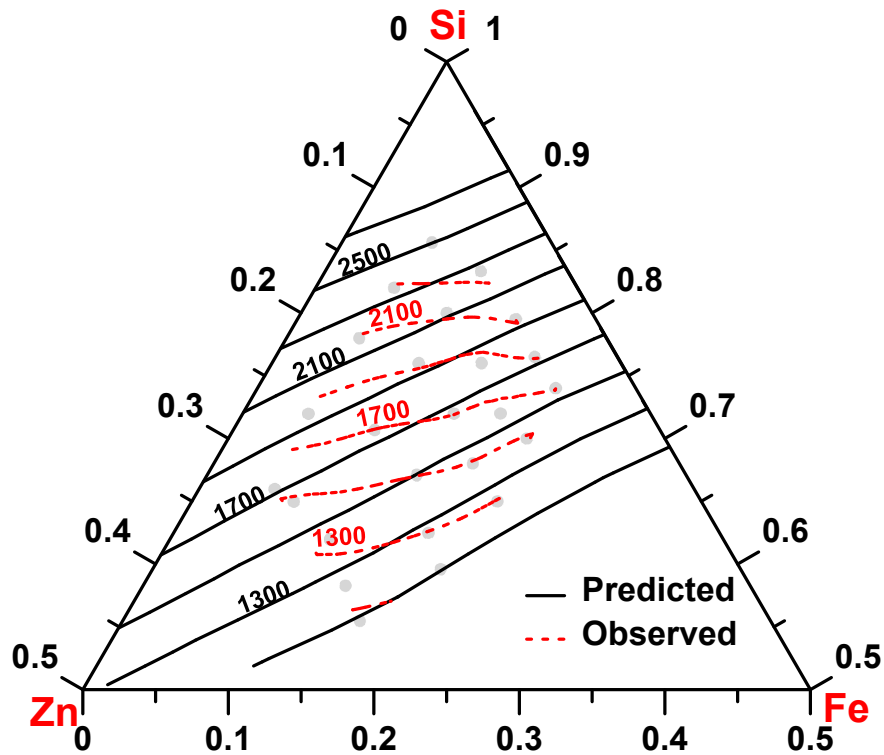
Figure 4.13 Contour plot of predicted (solid line) and observed (dashed line) capacities for Fe-Si-Zn electrodes. Capacities in mAh/g are labeled on the contour lines. Cell compositions for library Spt101 are shown in grey.
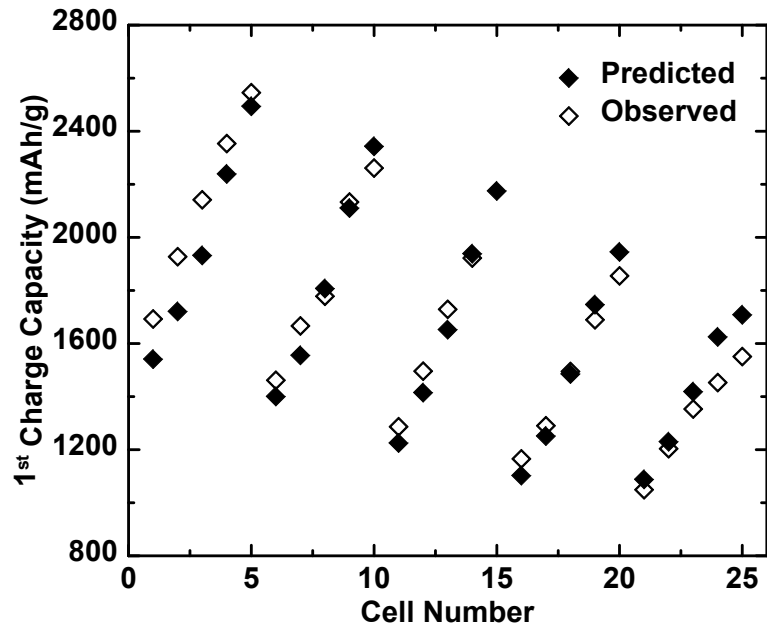
Figure 4.14 Predicted (closed diamonds) and observed (open diamonds) capacity for cells prepared from library Spt101.

4.4 Conclusions for the Fe-Si-Zn Ternary System

Thin film libraries of Fe-Si-Zn were fabricated and characterized using combinatorial high throughput techniques. A large range of Fe-Si-Zn compositions can be sputtered amorphously near the Si-rich corner of the phase diagram. The voltage curves and capacities of the films were strongly dependent on composition.

Initial coulombic efficiencies up to 0.94 were observed. ICE and hysteresis improved with increasing Si concentration in the electrodes. Absolute values of irreversible capacity were similar for all cells. Capacities were predicted assuming that only three phases were present in the electrodes: FeSi, Si, and Zn. Observed capacities agreed well with predicted capacities for all compositions.

The work presented in this chapter shows that increasing the concentration of Fe in the films not only reduces volume expansion by introducing an inactive FeSi phase, but also suppresses of $Li_{15}Si_4$ formation. Here it was found that addition of Fe to Si causes a significant depression in the discharge voltage curve without changing its shape. This depression in the voltage curve likely contributes to the suppression of $Li_{15}Si_4$ formation during cycling in Si-M active/inactive alloys in general. It was also shown that increasing Zn concentration in the films above 15 atom % suppressed the formation of $Li_{15}Si_4$. The mechanism by which Zn suppresses Si formation has been previously studied. Addition of Zn to the alloy also increases the volume fraction of active material in the electrode which may result in better Li diffusion.

This work shows that a wide composition range of amorphous Fe-Si-Zn thin-film materials can be fabricated and compositions with sufficient Fe and Zn content remain amorphous on electrochemical cycling. Theoretical specific and volumetric capacities of

the electrodes range from 1100 - 2500 Ah/kg and 1800 - 2100 Ah/L, respectively. Calculated volume expansions of the electrodes are between 153 % and 240 % if a molar volume of Li in the alloy is assumed to be 9 mL per mole.[6] Introducing Zn into Fe-Si alloys may be useful in improving Li diffusion as it can increase the fraction of active volume in the electrode while maintaining the same volumetric capacity/volume expansion. However, the addition of only Fe to Si electrodes may be sufficient if reduced volume expansion and suppression $Li_{15}Si_4$ formation are the only requirements.

Further work needs to be done to understand the electrochemistry of Fe-Si-Zn materials, such as the effect of discharge voltage depression caused by the addition of Fe. It is especially important to determine the structural and electrochemical properties of bulk Fe-Si-Zn powders made by more conventional means, such as ball milling. Incorporating Fe-Si-Zn alloys in conventional electrode coatings (with binder and conductive additives) is also necessary to obtain reliable cycling performance data. Ongoing and future work involving Fe-Si-Zn alloys will be discussed in Chapter 5.

Chapter 5 Conclusions and Future Work

The objective of this work was to study new Si-based alloys as anode materials for Li-ion batteries. The addition of Fe to Si thin-film electrodes has been previously studied in detail and adding Fe has been shown to improve performance of Si electrodes by introducing an inactive FeSi phase.[38] The addition of Zn to Si thin-film electrodes has also been studied in detail and it has been shown that adding Zn to Si electrodes can supress formation of crystalline $Li_{15}Si_4$ at low voltage.[35] In this work, it was hoped that the addition of both Fe and Zn to Si thin-film electrodes would lead to improvements in performance due to reduced volume expansion and suppression of $Li_{15}Si_4$.

5.1 Conclusions

The Fe-Zn subset of the Fe-Si-Zn ternary alloy system was discussed in detail in Chapter 3. Fe_xZn_{1-x} libraries were prepared by combinatorial sputtering and spanned a composition range of $0 < x < 0.55$. Films were found to be amorphous for x > 0.10. For low Fe concentrations crystalline Zn peaks were observed in the XRD patterns. As Fe content in the films increased, the sharp crystalline Zn peaks were broadened and lost intensity and two new peaks appeared which do not correspond to any known Fe-Zn phases.

Electrochemistry of Fe-Zn electrodes was strongly dependent on composition. It was shown that only films with less than 12 atom % Fe were active toward Li. For active compositions CE increased approximately linearly with Fe concentration to a maximum of 91% and cycling performance improved with increasing Fe concentration. All active compositions had average voltages vs Li/Li^+ that would be suitable for use as anodes. Average discharge voltages for active compositions ranged from 0.10 - 0.17 V and

decreased with increasing Fe concentration. Average charge voltage was 0.37±0.01 V for active compositions and did not show a dependence on Fe concentration. Although cycling performance improved with increasing Fe concentration, the performance of all active compositions was poor and capacity fade during cycling was rapid. Cycling performance of Fe-Zn alloys prepared by conventional methods will probably be different than performance of sputtered films. Further experiments would be necessary to determine performance of Fe-Zn alloys in conventional electrode coatings, although it is unlikely that Fe-Zn alloys will be used in commercial Li-ion cells due to poor Li diffusion in the electrodes.

Electrochemical and XRD measurements suggest that as an amorphous phase is introduced, the Zn atoms are rendered inactive by surrounding Fe atoms. Mössbauer effect measurements suggest that Fe atoms occur in three sites with different local Fe concentrations throughout the films. Ex-situ Mössbauer measurements of cycled electrodes suggested that some Fe-Zn phases in the electrode are inactive towards lithiation at room temperature. Mössbauer measurements also suggest that as the electrode is lithiated, Fe is displaced from the Fe-Zn alloy resulting in the formation of LiZn, inactive δ-phase Fe-Zn and isolated Fe.

Fe-Si-Zn ternary alloys prepared by combinatorial sputtering were discussed in Chapter 4. A large range of Fe-Si-Zn alloys were able to be prepared amorphously near the Si rich corner of the phase diagram. ICE, hysteresis, and capacities of electrodes were dependent on composition. ICE and hysteresis improved with increasing Si concentration in the films. Absolute values of irreversible capacity were similar for all compositions, but cells with higher Si content had higher total capacity which increased

the ICE. Average discharge and charge voltages of all compositions studied ranged from 0.11 V - 0.17 V and 0.37 V - 0.42 V, respectively. Average discharge voltage showed a strong dependence on Fe concentration, decreasing with increasing Fe content in the electrodes. Average charge voltage showed a dependence on Zn concentration, increasing with increasing Zn content in the electrodes. As a result, hysteresis increases with increasing Fe and Zn concentrations. Capacities of electrodes were predicted assuming the films comprised inactive FeSi, active Si, and active Zn. Observed capacities agreed well with the predicted capacities.

It was found that $Li_{15}Si_4$ formation during cycling could be supressed by additions of Fe and Zn. Increasing Zn concentration in the films above 15 atom % supressed the formation of $Li_{15}Si_4$. The mechanism by which Zn suppressed formation of $Li_{15}Si_4$ by has been previously studied.[35] In the work presented in this thesis it was found that increasing Fe content in the electrodes caused a significant depression in the discharge portion of the voltage curves without changing the shape of the curves. Depression in the voltage curves was as much as 0.75 V. Since $Li_{15}Si_4$ formation occurs below 50 mV, the voltage depression likely contributes to the suppression of $Li_{15}Si_4$ in Si-M active/inactive alloys in general. This effect was not noticed previously, despite the many previous studies of Si-M alloys.

Specific and volumetric capacities of Fe-Si-Zn electrodes presented in Chapter 4 ranged from 1100 - 2500 Ah/kg and 1800 - 2100 Ah/L, respectively, and had theoretical volume expansions between 153 % and 240 % upon full lithiation. Incorporating Zn into Fe-Si alloys increases the fraction of active volume in the alloy and may be useful in

79

improving Li diffusion through the electrode. However, the addition of only Fe to Si electrodes both reduces volume expansion, and suppresses formation of $Li_{15}Si_4$.

Fe-Si-Zn alloys are attractive for use in Li-ion cells because Fe, Si, and Zn are inexpensive and abundant.[84] The average voltage and ICE of these alloys are practical for use in current Li-ion battery technology and the high volumetric capacities of these materials is attractive. Volume expansion of the compositions presented in this work may be too large for use in commercial electrodes. The volume expansion of Fe-Si-Zn containing electrodes could easily be optimized by varying Fe and Zn content in the electrode, or by incorporating the alloy into a composite electrode with graphite.

5.2 Ongoing and Future Work

Further work is necessary to understand the electrochemistry of Fe-Si-Zn alloys. The effect of discharge voltage depression caused by the addition of Fe is interesting and should be examined in more detail. This voltage depression likely suppresses $Li_{15}Si_4$ formation in other Si-M active/inactive systems. It may be interesting to examine the effects that metal selection, metal concentration, and rate have on the voltage depression.

Combinatorial sputtering offers the advantage of fabricating and testing a wide range of compositions simultaneously. Analysing a wide range of sputtered compositions using XRD can provide information on which compositions may be amorphous when fabricated using bulk methods. Electrochemical cycling experiments on thin film electrodes can give useful information such as capacity, IRC, and hysteresis. Combinatorial work allows trends in the data to easily be correlated to material composition. Some drawbacks of combinatorial thin film libraries is that they do not provide reliable information on long term cycling performance because there is no binder

or conductive additive in the electrodes. Cycling performance and $Li_{15}Si_4$ formation in sputtered films also varies with film thickness, therefore cycling data is not reliable.[26] Sputtering is also not an economically viable method of producing electrodes for commercial cells.

It is important to determine the structural and electrochemical properties of Fe-Si-Zn alloys prepared by more conventional methods, such as ball milling. Fe-Si-Zn alloys prepared by ball milling can be incorporated into conventional electrode coatings with appropriate binders and conductive additives. The performance of ball milled Fe-Si-Zn alloys may vary from that of sputtered Fe-Si-Zn alloys.

Preparation of select Fe-Si-Zn alloys by low energy ball milling (roller milling) is underway. Roller milling can produce nanostructured and/or metastable amorphous alloys which are desirable for use in Li-ion alloy negative electrodes. Two compositions which have been fabricated by roller milling are indicated on the Fe-Si-Zn ternary phase diagram in Figure 5.1. The shaded region in the figure is the range of compositions that were determined to be amorphous in sputtered thin films. Compositions that fall within the shaded region of the phase diagram have the greatest chance of being prepared amorphously by roller milling. Figure 5.2(a) and (b) show the XRD patterns and for the P092 and P113 roller milled samples shown in Figure 5.1, respectively.

From Figure 5.2 it is clear that the structure of roller milled materials is strongly dependent on composition. It is important to notice that although these compositions fall within the range of Fe-Si-Zn alloys that can be sputtered amorphously, they are not fully amorphous when prepared by roller milling. It is also interesting that there is no strong

evidence of $FeSi_2$ formation in the XRD patterns of the roller milled samples, which is contrary to what is predicted by the phase diagram.
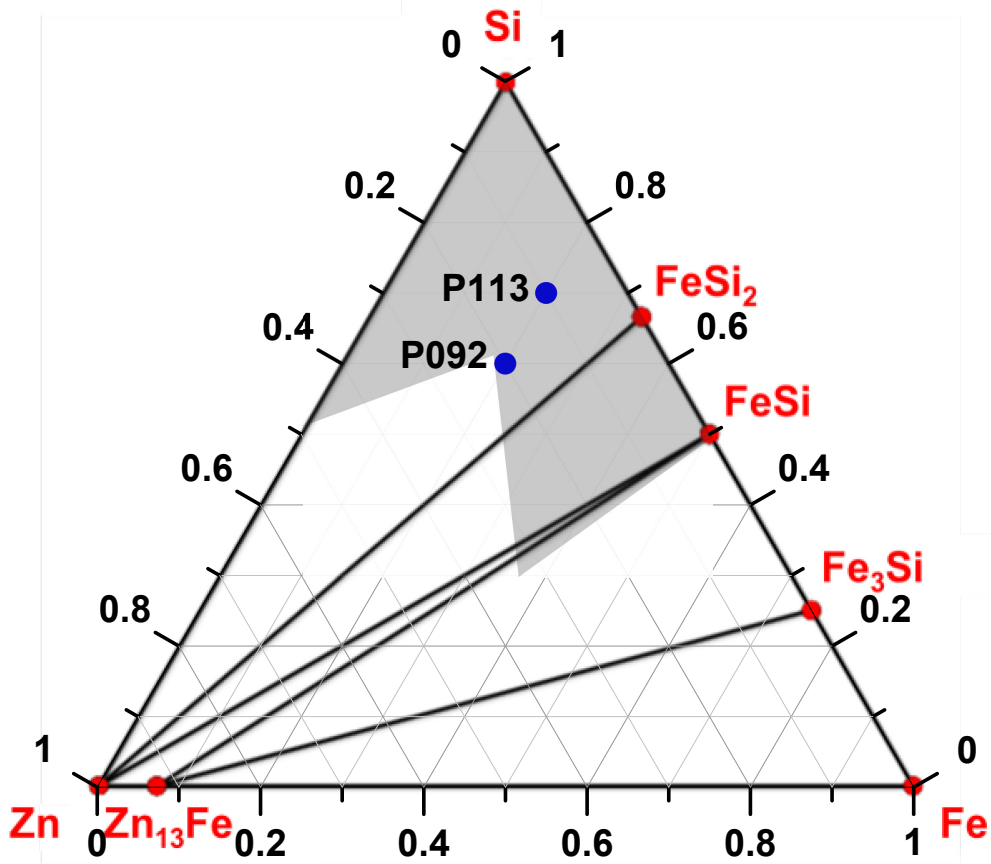
Figure 5.1 P092 and P113 roller mill compositions on the Fe-Si-Zn ternary phase diagram as predicted by the Materials Project at 0 K.[61,62]

A library of Fe-Si-Zn alloys are being prepared by roller milling. The structure of the alloys is being studied using XRD measurements and Mössbauer effect spectroscopy. The milled powders will then be incorporated into conventional electrode coatings and their performance evaluated in electrochemical cells. It will be interesting to compare the structural and electrochemical properties of Fe-Si-Zn alloys prepared by different methods. It would also be interesting to determine if the addition of Zn to Fe-Si alloys makes them easier to process by reducing "caking" during roller milling.
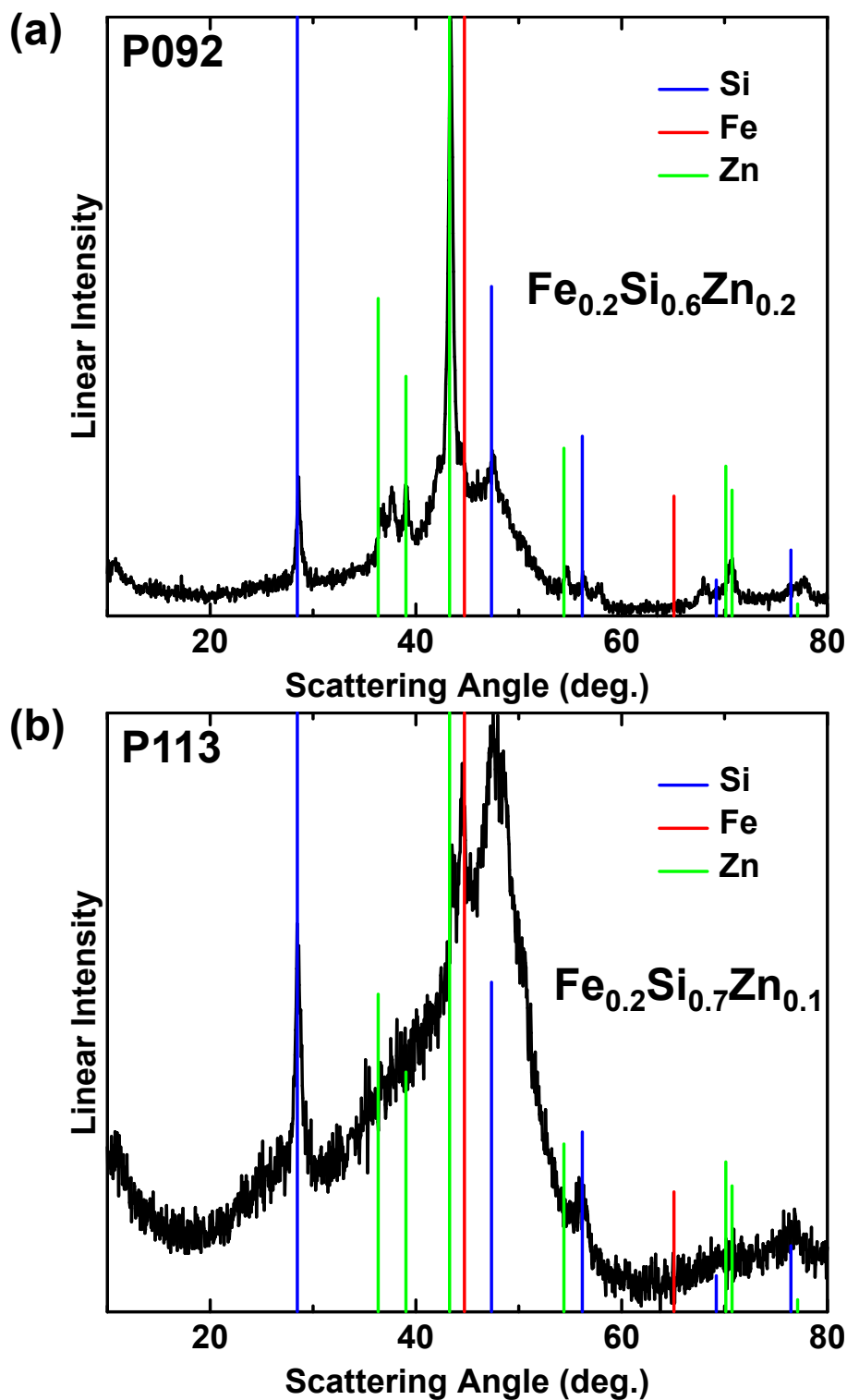
Figure 5.2 XRD patterns of P092 (a) and P113 (b) roller milled samples. Peak positions for Si, Fe, and Zn are indicated in the figure.

The work presented in this thesis suggests that it may be promising to study other alloy systems. Al-M (M = Fe, Mn, Cr, Ni) systems have been studied in detail previously.[12] The work in Chapter 3 of this thesis showed that Fe-Zn and Fe-Al binary systems exhibit similar trends when reacting electrochemically with Li. It could be interesting to study other Zn-M systems to see if they behave in a similar manner to the Fe-Zn or Al-M systems. Ternary Si-Zn-M systems prepared by combinatorial sputtering and roller milling may also be interesting to study. It is possible that performance of Fe-Si-Zn alloys could also be improved by the addition of other elements, such as C, Sn, or Al.

References

1. Y. Qi, S.J. Harris, *Journal of The Electrochemical Society*, **157** (6), A741 (2010).

2. J.R. Dahn, T. Zheng, Y. Liu, J.S. Xue, *Science*, **270**, 590 (1994).

3. J. Jiang, J.R. Dahn, *Electrochimica Acta*, **49** (26), 4599 (2004).

4. N.N. Sinha, J.C. Burns, J.R. Dahn, *Journal of the Electrochemical Society*, **160** (4), A709 (2013).

5. D.Y. Wang, N.N. Sinha, R. Petibon, J.C. Burns, J.R. Dahn, *Journal of Power Sources*, **251**, 311 (2014).

6. M.N. Obrovac, L. Christensen, D.B. Le, J.R. Dahn, *Journal of The Electrochemical Society*, **154** (9), A849 (2007).

7. J.R. Dahn, T. Zheng, Y. Liu, J.S. Xue, *Science*, **270** (5236), 590 (1995).

8. W. Xianming, T. Nishina, I. Uchida, *Journal of Power Sources*, **104** (1), 90 (2002).

9. J. Wang, P. King, R.A. Huggins, *Solid State Ionics*, **20** (3), 185 (1986).

10. C.M. Park, S. Yoon, S.I. Lee, J.H. Kim, J.H. Jung, H.J. Sohn, *Journal of The Electrochemical Society*, **154** (10), A917 (2007).

11. C.M. Park, H. Jung, H.J. Sohn, *Electrochemical and Solid-State Letters*, **12** (9), A171 (2009).

12. M.D. Fleischauer, M.N. Obrovac, J.D. McGraw, R.A. Dunlap, J.M. Topple, J.R. Dahn, *Journal of The Electrochemical Society*, **153** (3), A484 (2006).

13. J. Dahn, I. Courtney, O. Mao, *Solid State Ionics*, **111**, 289 (1998).

14. S. Yoon, C-M. Park, H.J. Sohn, *Electrochemical and Solid-State Letters*, **11** (4), A42 (2008).

15. J. Li, J.R. Dahn, *Journal of The Electrochemical Society*, **154** (3), A156 (2007).

16. W.J. Zhang, *Journal of Power Sources*, **196** (1), 13 (2011).

17. Sony Global- Press Release- Sony's new Nexelion Hybrid Lithium ion Batteries. http://www.sony.net/SonyInfo/News/Press/200502/05-006E/, accessed June 19, 2014.

18.   Amprius Inc. www.amprius.com, accessed June 19, 2014.

19.   Nexeon Limited. http://www.nexeon.co.uk/about/an-introduction-to-nexeon/, accessed June 19, 2014.

20.   M.W.M. Gaultois, T.D.T. Sparks, C.K.H. Borg, R. Seshadri, W.D. Boni, D.R. Clarke, *Chemistry of Materialsof Materials*, **25**, 2911 (2013).

21.   M. Winter, J.O. Besenhard, *Electrochimica Acta*, **45** (1-2), 31 (1999).

22.   U. Kasavajjula, C. Wang, A.J. Appleby, *Journal of Power Sources*, **163** (2), 1003 (2007).

23.   L.Y. Beaulieu, T.D. Hatchard, A. Bonakdarpour, M.D. Fleischauer, J.R. Dahn, *Journal of The Electrochemical Society*, **150** (11), A1457 (2003).

24.   A. Timmons, J.R. Dahn, *Journal of The Electrochemical Society*, **153** (6), A1206 (2006).

25.   M.N. Obrovac, L. Christensen, *Electrochemical and Solid-State Letters*, **7** (5), A93 (2004).

26.   T.D. Hatchard, J.R. Dahn, *Journal of The Electrochemical Society*, **151** (6), A838 (2004).

27.   M.N. Obrovac, L.J. Krause, *Journal of The Electrochemical Society*, **154** (2), A103 (2007).

28.   K.L. Lee, J.Y. Jung, S.W. Lee, H.S. Moon, J.W. Park, *Journal of Power Sources*, **129** (2), 270 (2004).

29.   V.L. Chevrier, J.W. Zwanziger, J.R. Dahn, *Canadian Journal of Physics*, **87** (6), 625 (2009).

30.   V.L. Chevrier, J.R. Dahn, *Journal of The Electrochemical Society*, **156** (6), A454 (2009).

31.   V.L. Chevrier, J.R. Dahn, *Journal of The Electrochemical Society*, **157** (4), A392 (2010).

32.   H. Yang, P. Fu, H. Zhang, Y. Song, Z. Zhou, M. Wu, L. Huang, G. Xu, *Journal of Power Sources*, **174** (2), 533 (2007).

33.   J. Yin, M. Wada, K. Yamamoto, Y. Kitano, S. Tanase, T. Sakai, *Journal of The Electrochemical Society*, **153** (3), A472 (2006).

34. T. Takamura, S. Ohara, M. Uehara, J. Suzuki, K. Sekine, *Journal of Power Sources*, **129** (1), 96 (2004).

35. T.D. Hatchard, M.N. Obrovac, J.R. Dahn, *Journal of The Electrochemical Society*, **152** (12), A2335 (2005).

36. T.D. Hatchard, J.R. Dahn, *Journal of The Electrochemical Society*, **152** (7), A1445 (2005).

37. T.D. Hatchard, J.R. Dahn, *Journal of The Electrochemical Society*, **151** (10), A1628 (2004).

38. M.D. Fleischauer, J.M. Topple, J.R. Dahn, *Electrochemical and Solid-State Letters*, **8** (2), A137 (2005).

39. K. Hanai, Y. Liu, N. Imanishi, A. Hirano, M. Matsumura, T. Ichikawa, Y. Takeda, *Journal of Power Sources*, **146** (1-2), 156 (2005).

40. H. Dong, R.X. Feng, X.P. Ai, Y.L. Cao, H.X. Yang, *Electrochimica Acta*, **49** (28), 5217 (2004).

41. S. Yoon, C.M. Park, H. Kim, H.J. Sohn, *Journal of Power Sources*, **167** (2), 520 (2007).

42. T.D. Hatchard, J.M. Topple, M.D. Fleischauer, J.R. Dahn, *Electrochemical and Solid-State Letters*, **6** (7), A129 (2003).

43. M.D. Fleischauer, J.R. Dahn, *Journal of The Electrochemical Society*, **151** (8), A1216 (2004).

44. M.A. Al-Maghrabi, J.S. Thorne, R.J. Sanderson, J.N. Byers, J.R. Dahn, R.A. Dunlap, *Journal of The Electrochemical Society*, **159** (6), A711 (2012).

45. T.D. Hatchard, M.N. Obrovac, J.R. Dahn, *Journal of The Electrochemical Society*, **153** (2), A282 (2006).

46. P. Villars, A. Prince, H. Okamoto, Handbook of Ternary Alloy Phase Diagrams, ASM International, Materials Park, OH, (1995).

47. J.D. McGraw, M.D. Fleischauer, J.R. Dahn, R.A. Dunlap, *Philosophical Magazine*, **86** (32), 5017 (2006).

48. J.R. Dahn, S. Trussler, T.D. Hatchard, A. Bonakdarpour, J.R. Mueller-Neuhaus, K.C. Hewitt, M. Fleischauer, *Chemistry of Materials*, **14** (8), 3519 (2002).

49. M.D. Fleischauer, T.D. Hatchard, A. Bonakdarpour, J.R. Dahn, *Measurement Science and Technology*, **16** (1), 212 (2005).

50. R. Ingalls, F. Vanderwoude, G.A. Sawatsky, Mössbauer Isomer Shifts, North Holland Publishing Company, (1978).

51. N.N. Greenwood, T.C. Gibb, Mossbauer Spectroscopy, Chapman and Hall Ltd., London, Great Britain, (1971).

52. M.A. Al-Maghrabi, N. van der Bosch, R.J. Sanderson, D.A. Stevens, R.A. Dunlap, J.R. Dahn, *Electrochemical and Solid-State Letters*, **14** (4), A42 (2011).

53. M.N. Obrovac, L. Christensen, D.B. Le, J.R. Dahn, *Journal of The Electrochemical Society*, **154** (9), A849 (2007).

54. T. Fujieda, S. Takahashi, S. Higuchi, *Journal of Power Sources*, **40** (3), 283 (1992).

55. Y. Hwa, J.H. Sung, B. Wang, C.M. Park, H.J. Sohn, *Journal of Materials Chemistry*, **22** (25), 12767 (2012).

56. T. Fujieda, S. Takahashi, S. Higuchi, *Journal of Power Sources*, **40** (3), 283 (1992).

57. M.I. Purcell, T.D. Hatchard, R.J. Sanderson, M.N. Obrovac, *Journal of the Electrochemical Society*, **161** (4), A643 (2014).

58. ASM International's Binary Alloy Phase Phase Diagrams, 2nd Edition, Materials Park, OH 44073-0002, USA, (1990).

59. M.D. Fleischauer, M.N. Obrovac, J.D. McGraw, R. A. Dunlap, J.M. Topple, J.R. Dahn, *Journal of The Electrochemical Society*, **153** (3), A484 (2006).

60. A.D.W. Todd, P.P. Ferguson, M.D. Fleischauer, J.R. Dahn, *International Journal of Energy Research*, **34** (6), 535 (2010).

61. S.P. Ong, W.D. Richards, A. Jain, G. Hautier, M. Kocher, S. Cholia, D. Gunter, V.L. Chevrier, K. A. Persson, G. Ceder, *Computational Materials Science*, **68**, 314 (2013).

62. A. Jain, S.P. Ong, G. Hautier, W. Chen, W.D. Richards, S. Dacek, S. Cholia, D. Gunter, D. Skinner, G. Ceder, K. A. Persson, *APL Materials*, **1** (1), 011002 (2013).

63. J. Hong, S. Oh, S.J. Kwon, *Intermetallics*, **11**, 207 (2003).

64. R. Kainuma, K. Ishida, *Journal of the Iron and Steel Institute of Japan- Tetsu to Hagane*, **91** (3), 349 (2005).

65. N.L. Okamoto, K. Tanaka, A. Yasuhara, H. Inui, *Acta Crystallographica Section B, Structural Science, Crystal Engineering and Materials*, **70** (Pt 2), 275 (2014).

66. M. Hong, H. Saka, *Acta Materialia*, **45** (10) (1997).

67. A. Johansson, H. Ljung, S. Westman, *Acta Chemica Scandinavica*, **22**, 2743 (1968).

68. R. Grant, D. Cook, *Hyperfine Interactions*, **94**, 2309 (1994).

69. J. Brandon, R. Brizard, *Acta Crystallographica*, **B30**, 1412 (1974).

70. P. Liao, B.L. Macdonald, R.A. Dunlap, J.R. Dahn, *Chemistry of Materials*, **20** (2), 454 (2008).

71. R. Belin, M. Tillard, L. Monconduit, *Acta Crystallographica. Section C, Crystal Structure Communications*, **56 (Pt 3)**, 267 (2000).

72. F.R. de Boer, R. Boom, W.C.M. Mattens, A.R. Miedema, A.K. Niessen, Cohesion in Metals Volume 1, North-Holland Physics Publishing, (1989).

73. T. Hatchard, Combinatorial Studies of Silicon-Based Alloy Negatives for Lithium-Ion Batteries, Dalhousie University, Ph.D., 2005.

74. A.J. Smith, J.C. Burns, X. Zhao, D. Xiong, J.R. Dahn, *Journal of The Electrochemical Society*, **158** (5), A447 (2011).

75. A. Hauet, A. Laggoun, J. Teillet, *Materials Science and Engineering: A*, 123 (1991).

76. M. Gu, G.W. Simmons, A.R. Marder, *Metallurgical Transactions A*, **21A** (February), 273 (1990).

77. A.R. Miedema, F. van der Woude, *Physica 100B*, 145 (1980).

78. A.M. van der Kraan, K.H. Buschow, *Physical Review B*, **27** (5), 2693 (1983).

79. W. Hoving, P. Scholte, P. Dorenbos, *Physical Review B*, **32** (12), 8368 (1985).

80. S. Hałas, *Materials Science-Poland*, **24** (4), 20 (2006).

81. R.S. Preston, S. Hanna, J. Heberle, *Physical Review*, **128** (5), 2207 (1962).

82.   T.A. Kovats, J.C. Walker, *Physical Review*, **181** (2), 610 (1969).

83.   O. Mao, R.A. Dunlap, J.R. Dahn, *Journal of The Electrochemical Society*, **146** (2), 405 (1999).

84.   M.W. Gaultois, T.D. Sparks, K.H. Borg, R. Seshadri, W.D. Bonificio, D.R. Clarke, *Chemistry of Materials*, **25**, 2911 (2013).

Appendix A Copyright Permission

COPYRIGHT PERMISSION REQUEST

Please complete all contact information:

Name: Lauren MacEachern   Title:

Company/Organization: Dalhousie University

Address: Dept. of Physics and Atmospheric Science, 6310 Coburg Road

City/State/Zip/Country: Halifax, Nova Scotia, B3H 4R2, Canada

Phone: (902)494-2211   Email: lr884450@dal.ca

I am preparing an article/chapter for publication in the following formats (*check as applicable*):
Print Only ☐   Internet Only ☐   Print and Electronic Media ☑

The information will be used for (*check as applicable*):
Journal article ☐   Conference presentation ☐   Internal company records ☐
Dissertation ☑   Student course material ☐   Commercial publication* ☐

Please complete the following:
The article/chapter title will be: Fe-Zn System
The publication title will be: Combinatorial Studies of Fe Containing Alloy Negative Electrodes for Li-ion Batteries
Publisher: Dalhousie University
Planned date of publication: August 2014

I hereby request permission for non-exclusive world rights for the above publication and all subsequent editions, revisions, and derivative works in English and foreign translations, in the formats indicated above from the following copyrighted content by **ASM International:**

Book ISBN: 0-87170-562-1   Copyright date: 1996
Book/Publication title: Binary Alloy Phase Diagrams Second Edition Plus Updates
Author name(s): ASM International
Article title: Fe-Zn (B.P. Burton and P,Perrot 1993), Li-Zn (A.D. Pelton, 1990)
Text page numbers:
Figure numbers (with page numbers):
Table numbers (with page numbers):

Signature: Lauren MacEachern   Date: 04-08-2014

FOR ASM INTERNATIONAL USE ONLY:
I (we) grant permission requested above. Please ensure that ASM International receives proper credit as publisher by citing the above ASM publication as a reference and including the following: Reprinted with permission of ASM International. All rights reserved. www.asminternational.org

ASM International Representative: Sue Sellers   Date: 8-4-2014

*For Commercial Publications, a copyright permission fee of $50 per figure will be assessed.
Exceptions can be made for reuse of content by its original authors.

ASM International, Permissions, 9639 Kinsman Road, Materials Park, Ohio 44073-0002   **SUBMIT**
permissions@asminternational.org, Phone: 440-338-5151 x5465, Fax: 440-338-8542